

HYDRAULIC FRACTURING AND INDUCED SEISMICITY: A
SEMI-ANALYTICAL APPROACH

by

Mohammad Azad

Submitted in partial fulfillment of the requirements
for the degree of Doctor of Philosophy

at

Dalhousie University

Halifax, Nova Scotia

August 2017

© Copyright by Mohammad Azad, 2017

TABLE OF CONTENTS

LIST OF TABLES	vii
LIST OF FIGURES	viii
ABSTRACT	xiv
LIST OF ABBREVIATIONS AND SYMBOLS USED	xv
ACKNOWLEDGMENTS	xviii
CHAPTER 1: INTRODUCTION	1
1.1 Seismicity due to deep fluids injection	1
1.2 Background and literature review	2
1.2.1 Background	2
1.2.2 Hydraulic fracture modeling	3
1.2.3 Fault slip reactivation due to hydraulic fracturing	8
1.2.4 Induced microseismicity by hydraulic fracturing	10
1.2.5 Poroelastic effect	11
1.2.6 Dilatancy effect	13
1.3 Objectives and organization of the research	14
CHAPTER 2: MATHEMATICAL FORMULATION	16
2.1 Problem settings	16
2.2 Hydraulic fracture	17

2.2.1	Finite (KGD) hydraulic fracture	17
2.2.2	Semi infinite hydraulic fracture with a lag	19
2.3	Shear fracture	21
2.4	Undrained pore pressure field	22
CHAPTER 3: NUCLEATION OF DYNAMIC SLIP ON A HY-		
DRAULICALLY FRACTURED FAULT		24
3.1	Model	24
3.2	Fault Opening Development (Hydraulic Fracture)	28
3.3	Fault Slip Development	31
3.3.1	Governing equations	31
3.3.2	Solution for the fault's slip	32
3.4	Results	32
3.4.1	Slip on a fault with unlimited weakening	34
3.4.2	Condition for nucleation of dynamic slip	36
3.4.3	Effect of residual friction on nucleation	40
3.4.4	Small scale yielding analysis	42
3.5	Field Implications	44
3.5.1	Estimates of slip weakening distance δ_w and nucleation length- scale a_w	44
3.5.2	Estimates of hydraulic fracture loading factor λ	46
3.5.3	Slipping patch, hydraulic fracture, and injected fluid volume at the nucleation	46
3.6	Conclusions	49

CHAPTER 4: NUCLEATION OF SLIP ON A NATURAL FRACTURE DUE TO INTERACTIONS WITH A PROPAGATING HYDRAULIC FRACTURE	51
4.1 Introduction	51
4.2 Model	52
4.3 Propagating semi-infinite hydraulic fracture	53
4.3.1 Viscosity dominated, negligible leak-off hydraulic fracture solution	54
4.3.2 Stress distribution around propagating hydraulic fracture	55
4.4 Slip activation region	56
4.4.1 Transformation of coordinates	57
4.5 Slip along the natural fracture	57
4.5.1 Scaling and numerical approach	57
4.5.2 Some field parameters estimates	58
4.6 Flow in a mechanically closed natural fracture	61
4.6.1 Undrained pore pressure along the natural fracture	63
4.7 Results	66
4.8 Conclusions	72
CHAPTER 5: NUCLEATION OF DYNAMIC SLIP ALONG A NATURAL FRACTURE CROSSED BY A PROPAGATING HYDRAULIC FRACTURE	76
5.1 Introduction	76
5.2 Model	77
5.3 Pore pressure along the edge crack	78
5.4 Slip along the edge crack	78

5.4.1	Scaling and numerical approach	79
5.5	Results	80
5.5.1	The model with unlimited weakening friction	80
5.5.2	Effect of residual friction	81
CHAPTER 6:	DISCUSSION	84
6.1	Relation to existing cases of HF induced seismicity	84
CHAPTER 7:	CONCLUSIONS AND RECOMMENDATIONS	88
7.1	Recommendations for future research	90
BIBLIOGRAPHY		91
APPENDIX A: DERIVATION OF GOVERNING EQUATIONS		102
A.1	Equilibrium equations	102
A.1.1	Stress function formulation	105
A.1.2	Dislocation solution	107
A.1.3	Stress field due to a planar crack	109
A.2	Mass conservation and continuity equation	111
A.3	Navier-Stokes equations of fluid flow	112
A.3.1	Laminar unidirectional flow in a gap space	114
APPENDIX B: SOME DETAILS OF THE ZERO-TOUGHNESS		
HYDRAULIC FRACTURE SOLUTION		116
APPENDIX C: NORMALIZED FORM OF SLIP FORMULATION		
ALONG THE HYDRAULICALLY FRACTURED FAULT		119
APPENDIX D: STRESS FIELD AROUND PROPAGATING HY-		
DRAULIC FRACTURE		120
C.1	Traction along the edge crack with an arbitrary orientation	120

**APPENDIX E: NORMALIZED FORM OF SLIP FORMULATION
FOR THE NATURAL FRACTURE BEFORE CROSSING 123**

**APPENDIX F: NORMALIZED FORM OF SLIP FORMULATION
FOR THE EDGE CRACK 126**

LIST OF TABLES

Table 4.1	Stress measurements for the strike slip state tectonic regimes at a lithostatic depth of 3 km.	59
Table 4.2	The assumed parameter values for the numerical analyses. The values represent as an examples of stress and pore pressure measurements at 3 km lithostatic depth. Conventional and slick water hydraulic fracturing are distinguished with the viscosity dominated length scale $L_{\mu}^{(Gel)}$ and $L_{\mu}^{(Slick\ water)}$, respectively.	61

LIST OF FIGURES

Figure 1.1	Simple fracture geometry models	4
Figure 2.1	Finite plane strain hydraulic fracture with length 2ℓ	17
Figure 2.2	Semi-infinite plain strain hydraulic fracture with lag of length λ	20
Figure 2.3	Pre-existing plain strain shear fracture with length $2a$	21
Figure 2.4	Slip weakening friction.	23
Figure 3.1	Hydraulic fracture (HF) with an open half-length $\ell(t)$ is driven along a fault by a constant rate of fluid injection Q_0 at the inlet. The fault slipping patch is characterized by the half-length $a(t)$, and the “frictionless” half-length $b(t)$ ($a > b > \ell$). The latter encompasses the open crack with half-length ℓ and the small regions of extent $b - \ell$ just outside of the HF tips where the effective normal stress is tensile as the result of the singular stress perturbation induced by the open crack. The fault lies parallel to the x axis and is oblique to the far-field principal stresses, which result in background values of the normal, σ_0 , and shear, τ_0 , stresses resolved on the fault plane.	25
Figure 3.2	Self-similar solution for the hydraulic fracture normalized opening $\bar{\Omega} = w/\varepsilon\ell$ and stress change $\Pi = (\sigma - \sigma_0)/\varepsilon E'^{-1}$ as a function of normalized distance x/ℓ (Carbonell et al., [42]; Adachi and Detournay [43]). Time dependent length L ($\ell \simeq 0.615L$) and stress $\varepsilon E'^{-1}$ scales are defined in (3.7). The dashed lines show the HF tip asymptotics (3.8).	30

Figure 3.3 (a) Example of the effective normal stress distribution for two values of the HF loading factor $\lambda = 0, 0.2$ and the HF half-length $\ell = 0.1a_w$. (b) Development of the tensile effective stress region ahead of the hydraulic fracture tip, $b - \ell$, with the growth of the hydraulic fracture length ℓ for the case with $\lambda = 0.2$. The asymptotic form of tensile effective stress region extension is shown by dashed line (3.13). The frictionless tips, $|x| = b(t)$, indicated by stars in (a), are nearly coincident with the hydraulic fracture tips $|x| = \ell(t)$, i.e. $b/\ell \simeq 1$ 34

Figure 3.4 Development of (a) the slipping patch ahead of the hydraulic fracture tip, $(a - \ell)/a_w$, and (b) peak slip in the frictional patch $\delta_{x=b}$ with the growth of the hydraulic fracture half-length ℓ for the hydraulic fracture loading factor $\lambda = 0.2$ and different values of the background shear stress, as indicated for each curve. Termination points of the curves correspond to the vertical slope and signify the instability of the quasi-static crack growth. 35

Figure 3.5 Development of the normalized slip distribution, (a), the normalized shear stress distribution, (b), the normalized hydraulic fracture opening distribution, (c), and the normalized effective normal stress distribution, (d), along the fault during the hydraulic fracture propagation for loading factor value $\lambda = 0.2$ and background shear stress $\tau_0/\tau_p = 0.7$. Blue arrows and stars correspond to the nearly coincident hydraulic fracture, $|x| = \ell(t)$, and the frictionless, $|x| = b(t)$, tips, respectively. It can be seen that the extent of the segments where the effective normal stress is tensile, $b - \ell$, is practically negligible. The instability of the quasi-static crack growth is highlighted by heavier lines. 37

Figure 3.6 Shear fracture half-length vs. hydraulically open fracture half-length at the instability for various values of the loading factor $\lambda = 0, 0.2$ and 1, as determined from Eigenvalue analysis. Eigenvalue analysis allows to establish relationship between nucleation crack size a_c and its open part ℓ_c , but not their relation to the background stress τ_0 38

Figure 3.7 (a) Normalized shear crack half-length a_c/a_w and (b) the normalized slip at the frictionless tips $(\delta_{x=b})_c/\delta_w$ at the instability as functions of the fault understress $(\tau_p - \tau_0)/\tau_p$ for three values of the dimensionless loading factor $\lambda = 0$, $\lambda = 0.2$ and $\lambda = 1$. Normalized critical hydraulic fracture half-length at the instability ℓ_c/a_w is shown by dotted lines in (a). The reference solution for the instability under the incipient hydraulic fracture condition (i.e., injection fluid pressure is just below the normal stress) of Garagash and Germanovich [64] is shown by dashed line. 40

Figure 3.8 Growth of (a) the slipping segments ahead of the hydraulic fracture tips and (b) the normalized slip at the frictionless tips with the the hydraulic fracture advance in the model with residual friction $f_r/f_p = 0.6$, loading factor $\lambda = 0.2$ and for different values of background shear stress. The results are compared to the small scale yielding (s.s.y.) approximation (dotted lines) in (a). No dynamic instability is observed for values of the background stress below the ambient value of residual strength, $\tau_0/\tau_r < f_r/f_p = 0.6$ 41

Figure 3.9 The normalized shear crack half-length a_c/a_w , (a), and the normalized slip at the frictionless tips $(\delta_{x=b})_c/\delta_w$, (b), at the instability as functions of the fault understress $(\tau_p - \tau_0)/\tau_p$ in the model with the residual friction $f_r/f_p = 0.6$ for two values of the loading factor $\lambda = 0, 0.2$. Corresponding half-length of the hydraulic fracture at instability ℓ_c/a_w is shown by dashed line in (a). (The dotted line shows the reference solution for the model with unlimited weakening ($f_r = 0$) for $\lambda = 0$). The solution is only weakly dependent on the loading factor . The hydraulic fracture induced slip on faults with $\tau_0 \leq \tau_r$ is unconditionally stable. The heavy dashed line shows the reference solution for the instability under the incipient hydraulic fracture condition of Garagash and Germanovich [64]. 42

Figure 4.1 A semi-infinite hydraulic fracture approaches a pre-existing shear fracture. Stress perturbation ahead of the hydraulic fracture activates slip along the shear fracture. 53

Figure 4.2	The limiting failure values of the effective principal stress ratio for the planes that are oriented at an angle θ to the direction of maximum horizontal stress assuming a typical peak friction coefficient $f_p = 0.8$. The blue dashed lines correspond to the assumed effective principal stress ratios in the numerical analyses.	61
Figure 4.3	The problem set up to approximate pore pressure along the natural fracture	63
Figure 4.4	Medium pore fluid diffusion into the fracture at the arbitrary location chosen by the normalized distance $L_{max}/L_\mu = 10$. Pore fluid flows to equilibrate the pressure difference between the normalized medium pressure $(p_0 + \Delta p_{und})/(\sigma_{min} - p_t) = 0.98$ and the inside fracture pressure $(p_0 + \Delta \sigma_n)/(\sigma_{min} - p_t) = 0.82$ for conventional hydraulic fracturing scenario.	65
Figure 4.5	Stress perturbations (positive in compression) (a) $\Delta\sigma_{YY}$, (b) $\Delta\sigma_{XX}$, (c) $\Delta\sigma_{XY}$ and (d) pressure perturbation Δp_{und} around propagating hydraulic fracture. Note that the negative X values along the moving coordinates (X, Y) shows the area ahead of the hydraulic fracture.	68
Figure 4.6	Degree of stress rotation by the hydraulic fracture stress perturbation	68
Figure 4.7	A, A' : Slip activation on conjugate pair of favorably oriented natural fractures during conventional hydraulic fracturing, case study I.	69
Figure 4.8	(a) Normalized peak background shear strength $f_p(\sigma_n - (p_0 + \Delta p_{und}))/(\sigma_{min} - p_{tip})$ and background shear stress distribution $\tau^b/(\sigma_{min} - p_{tip})$ along fracture oriented at $\beta = 20^\circ$, at two values of normalized time $Vt/L_\mu = 15.8$ and $Vt/L_\mu = 19.8$. (b) Shear stress distribution along the crack at normalized time $Vt/L_\mu = 19.8$ when nucleation of dynamic slip takes place.	70

Figure 4.9	Growth of crack half length a/a_w (a) and normalized slip at the center of slipping patch δ_b/δ_w (b) vs. time Vt/L_μ for the fracture with different orientations during conventional HF (case study I). Slip either turns into dynamic rupture (indicated by vertical slops) or the slipping patch expansion stops (shown by blue circles).	71
Figure 4.10	(a) Normalized slip δ/δ_w and (b) stress distribution $\tau/(\sigma_{min} - p_{tip})$ along the fracture oriented at $\beta = 20^\circ$ for different values of time Vt/L_μ (first numerical analysis). The heavy line corresponds to the instability. Center of slipped portion of the crack is shown by star in (a).	71
Figure 4.11	(a) Crack expansion stops along the fracture oriented at $\beta = 14^\circ$ where examples of normalized slip δ/δ_w and (b) stress distribution $\tau/(\sigma_{min} - p_{tip})$ are plotted for different values of time Vt/L_μ (Case study I).	72
Figure 4.12	Critical crack half-length a_c/a_w (a, d), critical (or a ceased expansion) time Vt_c/L_μ (b, e) and (c, f) slip at the center of slipping patch at instability $(\delta_b/\delta_w)_c$ as a function of fracture orientation for conventional (gel) compared to slick water hydraulic fracturing (case study I). The values of maximum crack expansion (i.e., no instability) in the slick water stimulation are presented by dashed line for the comparison.	73
Figure 4.13	Comparison of the two performed numerical analyses on instability of slip along the natural fracture (under different in-situ stress conditions) for conventional HF. Slip grows stably along the fracture which is subjected to the less critical effective principal stress ratio (case study 2 shown by red dashed line).	74
Figure 5.1	The semi-infinite hydraulic fracture crosses the pre-existing shear fracture. Pore pressure diffusion into the edge cracks activates slip along them.	77
Figure 5.2	Normalized pore pressure evolution with time inside the edge crack inclined at $\beta = 10^\circ$ during conventional HF, case study I.	79

Figure 5.3	Growth of edge crack length a/a_w (a) and normalized slip at the crack mouth δ_{max}/δ_w (b) vs. time Vt/L_μ for the crack with different orientations during conventional HF.	80
Figure 5.4	(a) Normalized slip δ/δ_w and (b) stress distribution $\tau/(\sigma_{min} - p_{tip})$ along the edge crack oriented at $\beta = 40^\circ$ at different values of normalized time Vt/L_μ . The heavy line corresponds to the instability.	81
Figure 5.5	Normalized critical edge crack length a_c/a_w (a), critical time Vt_c/L_μ (b) and (c) critical slip at the crack mouth $(\delta_{max})_c/\delta_w$ for the fracture with different orientations. The results are compared to the slick water HF (shown by gray line) and to the case study 2 with lower effective principal stress ratio (shown by dashed line).	82
Figure 5.6	Growth of the edge crack length a/a_w (a) and (b) slip at the crack mouth δ_{max}/δ_w with time for the fracture with different orientation in the model with residual friction $f_r/f_p = 0.6$ during slick water HF (case study I). The results are compared to the model with no residual friction (shown by dotted line).	83
Figure A.1	An infinitely small differential element in equilibrium	102
Figure A.2	Unidirectional flow between parallel plates	114

ABSTRACT

The injection of fluids into the ground is undertaken in a number of engineering practices including hydraulic fracturing, liquid waste disposal, CO₂ sequestration and extraction of geothermal heat (EGS). Study of mechanisms for slip on faults/natural fractures due to hydraulic fracturing is of great interest for the energy resource industry in view of efficiency of hydraulic fracturing, seismic monitoring and seismicity related safety hazards. In this thesis, semi-analytical approaches are applied to investigate physical processes associated with hydraulic fracturing induced seismicity and to develop a deeper understanding of the problem. The primary focus is on the modeling of initiation and growth of slip on a pre-existing fault/fracture due to interaction with a single propagating hydraulic (tensile mode) fracture.

The first part of the thesis is concerned with the relationship between hydraulic fracturing injection into a fault and the possibility of a seismic slip. The results show that the nucleation of dynamic slip on a fault with slip-weakening friction is only weakly dependent on the magnitude of the stress perturbation ahead of the propagating hydraulic fracture (HF), or the HF propagation regime, and is mainly controlled by the hydraulic fracture length (i.e., the size of the fully unloaded fault segment at a given time). The growth of the fault slipping patch remains stable when the background shear stress τ_0 is smaller than the residual fault strength τ_r under ambient conditions. Otherwise ($\tau_0 > \tau_r$), nucleation of dynamic slip takes place when the hydraulic fracture grows to the critical size ℓ_c , which is vanishingly small $\propto \tau_p - \tau_0$ for critically-stressed faults (i.e., when the background stress approaches the fault peak strength, $\tau_0 \rightarrow \tau_p$) and is diverging as $\propto 1/(\tau_0 - \tau_r)$ when the stability boundary is approached ($\tau_0 \rightarrow \tau_r$). In addition, no dynamic slip transients are predicted when background shear stress is less than the residual fault strength.

In the second part of the thesis we examine the possibility of a microseismic slip on a natural fracture as a result of poromechanical interactions with an advancing hydraulic fracture. Nucleation of slip on the frictional fracture approached by the hydraulic fracture depends on the state of in-situ stresses, hydraulic fracture pressure, angle of approach and friction of the fracture. Slip instability, consistent with field observations, occurs on the critically stressed and favorably oriented strike-slip fracture. Nucleation takes place as the slipping patch reaches the critical length $\sim E/(\sigma_{min} - p_{tip}) \times \delta_w$, where E' is the elastic modulus of the rock, σ_{min} the minimum in-situ principal stress, p_{tip} tip pressure (proportional to ambient pore pressure p_0), and δ_w is the characteristic slip weakening distance. Finally, we have studied nucleation of slip on a natural fracture crossed by a propagating hydraulic fracture. Slip initiates along the edge crack as the frictional strength drops due to increase in pore pressure by diffusion of fluid from the hydraulic fracture.

LIST OF ABBREVIATIONS AND SYMBOLS USED

a	shear crack half-length
a_w	characteristic slipping patch length
a_c	critical crack half-length
B	Skempton's coefficient
B'	plane-strain Skempton's coefficient
b	frictionless tip
E	Young's modulus
E'	plane-strain modulus of elasticity
f	friction coefficient
f_r	residual friction
G	energy release rate
G^*	fracture energy
$G_{i,j,k}$	influence functions
h	fracture height
k	formation permeability
k_{ni}	initial normal stiffness
K_{Ic}	rock toughness
KGD	Khristianovic and Geertsma and de Klerk
ℓ	hydraulic fracture half-length
ℓ_c	critical hydraulic fracture half-length
ℓ_{tip}	lag's length
$\dot{\ell}$	hydraulic fracture front velocity
L	crack length scale
L_μ	viscosity dominated length scale

p	internal fluid pressure
PKN	Perkins and Kern and Nordgren
p_{tip}	tip pressure
p_0	ambient pore pressure
p_*	characteristic pressure
Q_0	total volumetric flow rate
S	storage coefficient
t	time
V	hydraulic fracture propagation velocity
V_{inj}	injected volume
$V_{inj,c}$	critical injected volume
w	crack opening
w_0	neutral hydraulic opening
W	slip weakening slope
x	spatial coordinate in 2D
y	spatial coordinate in 2D
α	diffusivity coefficient
β	fracture orientation
γ	dimensionless hydraulic fracture half-length
δ	crack slip
δ_w	slip weakening distance
ε	small non-dimensional parameter
λ	loading factor
μ	injected fluid viscosity
μ_f	formation fluid viscosity
ν	Poisson's ratio
ν_u	undrained Poisson's ratio

σ_{min}	minimum principal stress
σ_{max}	maximum principal stress
σ_0, σ^b	background normal stress
$\bar{\sigma}_0$	effective normal stress
τ	shear stress
τ_0, τ^b	background shear stress
τ_r	residual shear strength
ϕ	porosity
Λ	dimensionless lag
Γ	stiffness ratio
Π	non-dimensional pressure
Ω	non-dimensional opening

ACKNOWLEDGMENTS

First and foremost I would like to express my sincere gratitude to my advisor Dr. Dmitry Garagash for his guidance, patience and support during my PhD studies at Dalhousie University. I am thankful of his valuable guidelines that inspired me to broaden my knowledge on the research topic. I also would like to express my deepest gratitude to my Co-Supervisor Dr. Mysore Satish for his supervision and constant support.

It is my pleasure to thank my PhD advisory committee, Dr. Farid Taheri and Dr. Gordon Fenton for their time and support.

I also wish to express my gratitude to my friend and colleague Dr. Erfan Sarvaramini for his help during these years. My sincere thanks to Dr. Robert Viesca for our scientific discussions.

Last but not least I am very grateful to my family and friends for their love, inspiration and encouragement over the years. It would not have been possible for me to overcome these challenging years without their support.

CHAPTER 1: INTRODUCTION

1.1 Seismicity due to deep fluids injection

The injection of fluids into the ground is undertaken in a number of engineering practices including hydraulic fracturing [1, 2], CO₂ sequestration [3, 4] and extraction of geothermal heat [5, 6, 7]. Injection induced or triggered earthquakes have been cited in relation to liquid waste disposal [8, 9, 10, 11]; geothermal operations [12], and hydraulic fracturing stimulation of hydrocarbon reservoirs [13, 14]. Although hydraulic fracturing operation has less perturbing characteristics compared to other anthropogenic triggers (probably due to lower volumes of fluid and shorter pumping time), there are several documented cases of felt earthquakes associated with hydraulic fracturing [13, 15]. While microseismicity induced by hydraulic fracturing is ubiquitous in brittle, naturally fractured formations [16, 17].

Seismic events occur as a result of the stress changes and pore pressure perturbation created by the injection. Slip initiates owing to increase of shear stress and/or reduction of effective normal stress acting across preexisting fracture/fault surfaces. Poroelastic changes of the shear stress may also lead to slip activation provided that the injection source is located away from the fault plane [18, 19]. As the public's concern about the increase of induced seismic activity has grown, more studies are investigating the different physical processes occurring during an injection. The goal of these studies is to make extraction of hydrocarbons through hydraulic fracturing more efficient and, at the same time, to lower the environmental impacts.

1.2 Background and literature review

1.2.1 Background

The industrial process of hydraulic fracturing (HF) is utilized widely in the exploitation of hydrocarbon resources. In the classical sense, a hydraulic fracture is a wing-shaped tensile fracture propagating away from the wellbore. Rock is fractured by high-pressure hydraulic fracturing fluid (gel or slick water) as the pressure exceeds the sum of the minimum principal stress σ_{min} , and the tensile strength of the rock, creating an opening-mode fracture that propagates in the plane normal to σ_{min} . The fracture continues to grow as long as the pumping rate is higher than the rate of fluid leaking off into the formation. Once the pumps are shut down, closure of the fracture may significantly lower its conductivity. In order to keep the fracture open, a propping agent like sand grains or ceramic is usually added to the hydraulic fracturing fluid [20].

The hydraulic fracture stimulation technique has been used for more than half a century to enhance production from hydrocarbon reservoirs. The recent advances in the hydraulic fracture technique in conjunction with horizontal drilling technology have enabled economical production of very low permeability shale formations. Horizontal drilling allows connectivity of more distant volumes of rock by creating or stimulating fractures that act as conduits to flow where the well may extend laterally to several kilometers within the shale formation [11, 14].

Numerous studies have shown occurrence of seismicity as a result of hydraulic fracture stimulation in oil and gas settings [21, 15]. Significant seismic slip (earthquake) occurs as the state of stress and/or fluid pore pressure are perturbed along a fault. Even with many fewer induced seismic hazards compared to longterm wastewater injection operations [22], the U.S., U.K., and Canada each have well documented earthquakes directly linked to HF operations of low-permeability shale formations, such as in

Blackpool, United Kingdom [23]; the Eola field, Oklahoma [24]; the Horn River and Montney basins, British Columbia [25, 26]; Harrison County, Ohio [27]; Poland township, Ohio [28]; and Crooked Lake, Alberta [29, 30] with reported moment magnitudes (M_W) ranging from 2.0 to 4.6.

During hydraulic fracture stimulation, small magnitude induced microseismicity $-3 < M_W < 2$ routinely occur as a result of creation of new fractures and interaction with pre-existing fractures. These microseismic events often have small magnitudes to be felt or even recorded unless sensitive downhole recorders at close proximity are used [31]. However, the events' magnitudes can increase in some naturally fractured reservoirs particularly those at a high stress level. Microseismic monitoring may be performed to map gross structure and fluid-flow paths stimulated by the hydraulic fracturing operation.

1.2.2 Hydraulic fracture modeling

The study of mechanics of hydraulic fracturing have attracted numerous contributions over the past few decades. The mathematical modeling of physical interaction between fluid and rock during hydraulic fracture propagation can be very challenging. The analytical and numerical analysis of the hydraulic fracture process have attracted numerous contributions [32]. Due to complexity of the problem and challenging computational effort, the models are often simplified to idealized fracture geometries. However, these more simple idealized models can be very useful study tools for analyzing various problem parameters as well as identifying different propagation regimes.

The most widely used fracture geometry models are (Figure 1.1):

- The plain strain or KGD (after Khristianovic Geertsma and de Klerk) model: assumes a crack with infinite height where every horizontal cross section has the state of plane strain deformation.

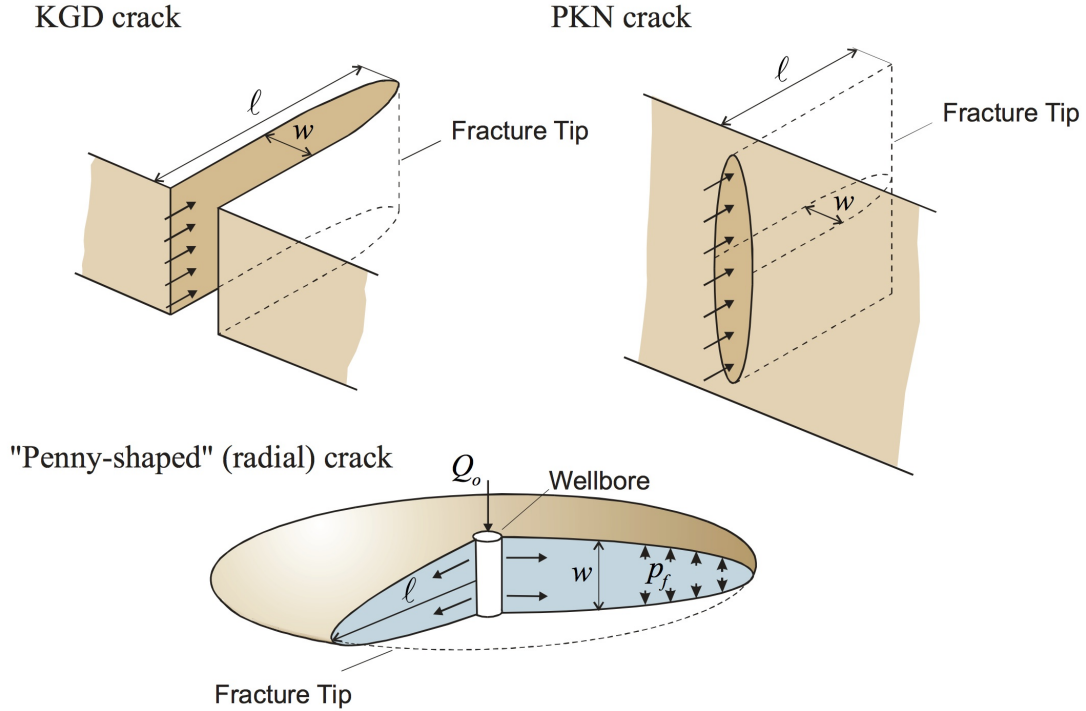


Figure 1.1: Simple fracture geometry models [33].

- The PKN (Perkin and Kern and Nordgren) model: assumes that the crack length is much larger than its height (confined between two impermeable rock layers). Plane strain is considered in the vertical elliptical shape cross sections perpendicular to the direction of fracture propagation.
- The Penny-shaped or radial crack model: assumes an axisymmetric crack propagation with respect to the wellbore.

In these models, the rock is assumed to be a continuous, homogeneous, isotropic linear elastic solid. The fracture propagates as the injection continues and the fracturing fluid flows along the length of the fracture. The exchange of fluid between the fracture and the rock may also play an important role in the HF propagation.

Since the early contribution of Khristianovic and Zeltov [34], Perkin and Kern [35], Geertsma and de Klerk [36] and Nordgren [37], many studies investigated analytical and numerical solutions of these fracture models. The main objective is to evaluate

the fracture growth rate, the fluid pressure and the fracture opening for various propagation regimes. In the viscosity-dominated propagation regime, the energy dissipation needed to break the rock is negligible compared to the energy losses in the flow of viscous fluid, while in the toughness-dominated regime, viscous losses are negligible compared to the energy required to break the rock. In addition to these dissipation processes, lagging of the fluid's front behind the fracture front and fluid leak-off (into the permeable solid) are the other important physical process governing propagation of the hydraulic fracture [38]. The corresponding models simultaneously consider

- 1) The lubrication equation, which describes the flow of fluid in the fracture. In the case of a permeable rock, the exchange of fluid with surrounding rock is governed by the fluid leak-off equation.
- 2) The elasticity equation that relates the deformation of the fracture to the net pressure.
- 3) The fracture propagation criterion.

Analytical solution of these models are mathematically challenging due to (i) the non-linear coupling of the lubrication equation and elasticity equation and (ii) the non-local mechanical response of the fracture governed by the elasticity equation (i.e., the crack opening at a position along the fracture is subject to the fluid pressure at another position). Below, we mention some of the most relevant studies carried out on the plane strain crack model (either finite KGD fracture, or steadily moving semi-infinite fracture). Although the main focus of this study is on the hydraulic fracturing injection, the similar model and arguments hold for analogous buoyancy-driven magmatic intrusions.

Spence and Sharp [39] presented a self-similar solution for a KGD crack where the non-dimensional form of the solution depends on the normalized stress intensity factor at the tip. They assumed the square root tip asymptote of the Linear Elastic Fracture

Mechanics (LEFM) for the crack tip opening: $w \sim X^{1/2}$, where X is the distance from the tip. Lister [40] considered the problem of a steady propagating, buoyancy-driven hydraulic fracture for relatively small fracture toughness and presence of a fluid lag zone.

For the case of zero toughness and under the assumption that the fluid flows up to the tip of the fracture, the fluid-solid coupling in the near tip region has an exact matching singularity between the lubrication and elasticity equations [40, 41]. Desroches et al. [41] established the exact zero-toughness solution for a semi-infinite fluid-driven fracture propagating steadily in an impermeable rock. The solution is characterized by the matching singularity of the crack opening w varying as $X^{2/3}$ (compared to the $X^{3/2}$ of linear elastic fracture mechanics) and fluid pressure p as $-X^{-1/3}$. The corresponding weak singularity of the pressure is associated with a negative infinite fluid pressure at the tip of the fracture.

Carbonell et al. [42], using the exact tip singularity, constructed the self similar solution for a finite KGD crack propagating in an impermeable, zero toughness elastic solid due to a constant rate of injection. Adachi and Detournay [43] generalized this solution to the case of power law fracturing fluid rheology.

Negative infinite fluid pressure at the tip of plane strain crack propagating in zero toughness solid suggests the existence of a lag between the fluid front and the tip of the moving fracture (since the fluid cannot sustain an infinite suction or negative pressure) [44]. The latter has a similar role as the process or plastic zone to ensure finiteness of stresses at the fracture tip. Furthermore, the presence of a lag is necessary for a hydraulic fracture propagating in a solid with finite toughness ($K_{Ic} > 0$ where K_{Ic} is the critical rock toughness). Under assumption of no lag, solving the lubrication equation combined with the opening asymptote of linear elastic fracture mechanic $w \sim X^{1/2}$ imposes a logarithmic singularity for the pressure $p \sim \ln X$ [45]. Studies show that the lag is several orders of magnitude smaller than a characteristic

length of the fracture and hence can be often neglected, but not always (see Garagash and Detournay [46] and Garagash [44] for the conditions when the lag can be neglected). The lag plays a significant role in the near tip processes, like interaction with faults/ fractures in the hydraulic fracture tip vicinity, where the lag and associated stress perturbation may be important vs. the larger scale (of the hydraulic fracture), where it may not be important (i.e., in determining the propagation of the hydraulic fracture itself).

The tip cavity is assumed to be filled by the vapors of the fracturing fluid for the case of the fracture propagating in an impermeable medium or by pore-fluid infiltrating from the permeable host solid [47, 48]. Garagash and Detournay [46] constructed a solution for a semi-infinite plane strain crack with a priori unknown length fluid lag propagating in an impermeable rock with an arbitrary toughness. The solution is consistent with the square root singularity of the linear elastic fracture mechanics in the tip region and asymptotically approaches the zero toughness solution [41] away from the fracture tip. The asymptotic form of the solution away from the tip which is characterized by large fluid pressure gradient and viscous energy dissipation corresponds to the part of the solution insensitive to the tip region behavior.

Garagash [44] studied the propagation of a finite plane strain hydraulic fracture with a fluid lag in an impermeable elastic solid with various toughness in the early stage of the propagation. The solution evolves between the two limiting cases corresponding to the zero under-pressure¹ (or maximum value of the lag as a fraction of fracture length) and infinite value of the tip under-pressure (or zero value of the lag of Spence and Sharp [49]).

For more contributions to the modeling of the other hydraulic fracture geometries refer to recent review paper on the subject [50].

¹under-pressure corresponds to the difference between the tip pressure and the far field confining stress

1.2.3 Fault slip reactivation due to hydraulic fracturing

A hydraulic fracture in general should propagate perpendicular to the minimum principal stress or in the direction of the maximum principal stress. If a hydraulic fracture encounters a preexisting fault that is oblique to the principal directions, it could propagate inclined to the direction of the least compressive stress as a consequence of the fault mechanical weakness. Several authors have described frozen dikes occupying faults or other preexisting fractures [51].

Healy et al. [8] pioneered considerations of the seismic slip of a fault due to elevated pore pressure caused by the deep waste fluid injection into the crust. Their work was followed by field experiments in earthquake control [52]. Theoretical [6, 53, 54] and numerical [55, 56, 57, 58] studies have explored the injection-induced activity associated with injection into faults. Hayashi and Abe [6] concluded that the hydraulic fracture propagates stably along the fault of variable in-situ normal stress and constant friction coefficient. Ziv and Rubinfeld [53] investigated the possibility of instability of dike intrusion along the fault due to the initiation of a tensile crack at the dike tips. Zhang et al. [54] considered a fluid injection and the associated slip development on a slip-weakening natural fault/fracture, where the injected fluid was assumed to be accommodated entirely by the inelastic dilation driven by the slip (i.e. intrinsic fault storage was neglected). Garagash et al. [59] and Germanovich et al. [60, 61] have considered the possibility of fluid injection into a fault in conjunction with the use of thermal techniques to locally modify the in situ stress and fault strength such as to trigger an earthquake in more controllable conditions than would happen otherwise. Viesca and Rice [62] studied the effects of pore pressure perturbations on the nucleation of dynamic slip in the context of submarine and subareal landslides. In a recent field study, Guglielmi et al. [63] studied aseismic slip on a fault directly stimulated by water injection.

Garagash and Germanovich [64] theoretically studied the nucleation of dynamic rup-

ture resulting from a pore pressure perturbation Δp due to injection into a fault. The fault remains closed during the injection as long as the fluid pressure is less than the in-situ normal stress, i.e., the normalized fluid overpressure $\Delta p/\bar{\sigma}_0 < 1$, where $\bar{\sigma}_0 = \sigma_0 - p_0$ is ambient effective normal stress. They showed that seismic slip occurs when the background stress τ_0 is larger than the residual strength τ_r along the fault, irrespective of fluid overpressure (as long as sufficient to activate slip). They also showed that unstable slip can be nucleated for $\tau_0 < \tau_r$ at low enough overpressure, however slip remains stable for all values of background stress $\tau_0 < \tau_r$ when near the incipient hydraulic fracture condition, i.e. $\Delta p/\bar{\sigma}_0 \rightarrow 1$. Injection into a fault with fluid pressure higher than the normal stress initiates a hydraulic fracture that propagates along the fault.

In this study, it has been considered that the friction along the fault/fracture has a slip-weakening character [65, 66, 67]. Contrary to a simple constant friction law, a slip-dependent friction model is comparable with a more complicated, laboratory derived, rate-and state-dependent friction model [68, 69, 70]. The latter considers that friction depends on slip velocity and state variables where the entire friction evolution has a more complex time dependency. Rubín and Ampuero [71] and Ampuero and Rubín [70] identified two end-member length scales for the nucleation patch in the context of rate-and state-dependent friction law. The minimum nucleation patch length scale is identical to that attained by [72, 73] for the linear slip-weakening friction law. Further, Garagash and Germanovich [64] linked the second end-member to the maximum extent of a slip weakening crack obtained by Andrews [74].

Nucleation of dynamic slip along a fracture with a slip-weakening friction has been studied before [73, 55]. Slip accumulates quasi-statically along the fracture when shear stress grows locally larger than the shear strength. With the weakening nature of slip, this quasi-static growth may transition to dynamic slip (micro-seismicity or earthquake).

1.2.4 Induced microseismicity by hydraulic fracturing

Pre-existing fracture networks often provide pathways for the flow of fluid through unconventional reservoir rocks where the matrix permeability is several order of magnitude smaller than that of the conventional reservoir rocks. The hydraulic fracturing operation can effectively increase the reservoir productivity by connecting the networks of the fractures to the well-bore. During the hydraulic fracture process, microseismic events occur due to slippage on pre-existing fractures in response to changes of the in-situ stresses.

While micro seismic monitoring provides valuable information on how a hydraulic fracture interacts with natural shear fractures, a complete understanding of the physics of the problem can be the key for maximizing efficiency of the hydraulic fracturing and also lowering associated seismic hazards. The propagating hydraulic fracture induces shear failure along the surrounding preexisting fracture(s) by altering the ambient stress/ pore pressure state. The slipped patch along a favorably oriented natural fracture grows quasi-statically (aseismically) until it ruptures seismically. The less favorably oriented fractures can still accumulate significant aseismic slip, and thus contribute to the reservoir permeability enhancement. The shear dilation (or normal deformation) occurs as a result of uplift in sliding over asperities of two rough fracture surfaces, which results in a permanent increase in the fracture permeability.

Hydraulic fracture propagation in a naturally fractured formation has been subject of various theoretical [75, 76, 77], experimental [78, 79] and numerical [80, 81] studies. The interaction of a hydraulic fracture with a natural fracture depends on various parameters including the in-situ stresses [79], friction and permeability along the shear fracture [82, 83]. The numerical models investigate various settings of multiple fracture propagation, slippage along one or a few preexisting fractures, or induced slip along a network of preexisting fractures. Interaction between each hydraulic frac-

ture and natural fracture determine ultimate geometry for the networks of stimulated fractures. There are three interaction types: (i) the hydraulic fracture crosses the natural fracture without changing direction; (ii) the hydraulic fracture crosses the natural fracture with an offset, where it deflects into the natural fracture, and then kinks out at some weak point along the natural fracture; (iii) the hydraulic fracture will be arrested at the intersecting point, diverted into the natural fracture, and then initiates a new fracture path at the tip of the natural fracture. The more realistic, three dimensional modeling of fractures interaction could be challenging to handle due to the spatial and temporal complexity of fracture propagation. An example of possible interaction scenarios in three dimensions could be that of hydraulic fracture splitting, with part of it along the intersection line crossing and another part diverting, essentially breaking the geometrical (initially planar) form of the fracture. Several analytical criterions have been proposed in the past to predict outcome of the interaction when a hydraulic fracture intersects a pre-existing natural fracture. The theoretical solution proposed by Blanton [75] and Warpinski and Teufel [76] are based on the differential stress and angle of intersection. Renshaw and Pollard's [77] criterion considers an orthogonal crossing interaction which was later modified by Gu and Weng [84] to be applicable for non-orthogonal intersections.

1.2.5 Poroelastic effect

The mechanical response of a fluid infiltrated porous rock can be altered by the presence of pore fluid and its mobility [85]. The time dependent, poro-mechanical interaction between fluid diffusion and deformation is composed of (i) changes in pore pressure due to changes in mean normal stress and (ii) changes in stresses due to pore pressure changes [86, 87]. In the quasi-static theory of poroelasticity, the inertia terms (i.e., mass times acceleration terms) are neglected, such that for the static or slow moving processes the inertia terms are much smaller than other terms in the

balance equation for linear and angular momentum. Occurrence of seismic events have been previously attributed to the delayed coupled poro-mechanical diffusion response whereby pore pressure changes have altered conditions on the fault [88]. Furthermore, Segall and Lu [18] and Deng et al. [19] among other numerical works, correlated the induced earthquakes to the poroelastic stress perturbations of the solid matrix rather than the fluid diffusion as the dominant factor.

The poroelastic solutions in the limiting cases of undrained and drained response correspond to an elastic solution but with different set of effective elastic moduli (undrained and slightly smaller drained modulus, respectively). In an undrained condition of rock-fluid interaction, the mass of the fluid inside the rock stays the same, which is attained when deformations occur rapidly relative to the time scale of fluid mass diffusion (i.e., no fluid flow). While an drained response denotes conditions when the pore fluid is allowed to leave or enter the rock, which is attained when deformations take place slowly compared to the time scale of fluid mass diffusion (i.e., no alteration in pore fluid pressure).

For a propagating hydraulic fracture front, deformation occurs so rapidly that there is no time for pore fluid to flow and hence the response is undrained around the hydraulic fracture tip. This condition particularly holds if the preexisting fractures are partially mineralized (so that their hydraulic conductivity prior to the slip is negligible). In practice, the response can be considered as undrained for very impermeable rocks where the pores are very small so that the pore fluid cannot flow through, or for the high rates of hydraulic fracture propagation. One way to quantify this is by comparing the timescale for pore pressure diffusion over a relevant problem length-scale to the timescale of hydraulic fracture propagation over the same distance. In Chapter 4, we calculate the timescale pertaining to diffusion in the rock mass over the characteristic size of the tip region where the stress is perturbed (i.e., L_{max}). This timescale is large compared to the hydraulic fracture propagation time over the

same distance, thus, assumed undrained response of the bulk rock. The undrained response eventually gives way to partially-drained response as the pressure diffuses into the rock.

1.2.6 Dilatancy effect

Shear dilatancy is associated with inelastic volume deformation of a fault/ natural fracture as a result of slip. The shear induced dilation causes pore pressure to drop and hence could restrengthen the fault by increasing the effective normal stress [89]. Many investigators have studied the effect of dilatancy altering the evolution of slip on faults [90, 91]. The shear dilation as a result of slippage along the fracture rough surfaces can also be a significant source of the fracture permeability change [92]. Zhang et al. [54] presented the model of a toughness dominated KGD crack propagating under a slip-weakening friction law. They assumed that the dilatation from slippage is related to the slip by a linear relationship proposed by Barton et al. [93]. In chapter 4, we show that the fluid pressure changes in a natural fracture can be approximated by that in the surrounding matrix. The analysis can be used to quantify whether dilatancy driven fluid pressure changes in the natural fracture persist on the timescale of the slip development or effectively obliterated by fluid exchange with the matrix. We show that the timescale relating to the diffusion about the natural fracture in order to accommodate the perturbation to the pore pressure due to dilation of the natural fracture (as a result of slip) is short compared to the propagation timescale, thus the perturbation to the pore pressure along the natural fractures caused by their dilation is effectively dissipated and pore pressure is given by the bulk undrained value.

1.3 Objectives and organization of the research

The goal of this research is to perform rigorous semi-analytical studies on physical interaction between hydraulic fracture injection and induced slip on faults/ natural fractures. We mainly focus on the modeling of quasi-static slip growth and induced seismicity on a pre-existing fault/fracture due to interaction with a single propagating hydraulic (tensile mode) fracture. The two dimensional KGD crack model which assumes a plane strain deformation, was used to define the crack geometry. Although in the physical world cracks are three dimensional, the two dimensional idealizations provide the basic solution of the crack tip fields and may serve as a reasonable approximation in applicable cases.

The thesis is organized as follows:

In Chapter 2, the mathematical formulation of the KGD crack driven by hydraulic fracture injection is presented. With the two dimensional idealization, stress field around the crack can be broken down into its components of pure tension and shear modes. Different model settings and assumptions are discussed.

In Chapter 3, we consider a hydraulic fracturing injection into a fault. Such a scenario is likely rarely realized, but serves as a simplified view of a more realistic case where a hydraulic fracture has been initiated some distance away and propagated to a fault, and then diverted into (propagate along) the fault zone due to its mechanical weakness. This is a viable mechanism for more significant seismic events (earthquakes) because of a larger surface area available for rupture along an extensive fault compared to less extensive natural fractures supporting microseismicity. The criterion for ultimate stability of the fault is established.

In Chapter 4, we consider seismicity along a pre-existing natural (shear) fracture which is approached by a hydraulic fracture. We made the assumption that interaction between fractures are one-way coupled. It is assumed that the stress pertur-

bation due to slip along the natural fracture does not affect the hydraulic fracture propagation regime. Our goal is to study microseismicity along natural fractures due to hydraulic fracturing using semi-analytical techniques. The results show the slip development on the natural fracture is controlled by the various problem parameters such as the hydraulic fracture pressure, the fractures orientation and in-situ stresses. In Chapter 5, we extend the model presented in the previous chapter to investigate nucleation of dynamic slip along a pre-existing fracture crossed by a propagating hydraulic fracture. The assumptions underlying the model are discussed. We review different mechanisms contributing to the slip growth on the natural fracture. This thesis contributes to the general understanding of the induced seismicity along faults/natural fractures due to the hydraulic fracture injection.

CHAPTER 2: MATHEMATICAL FORMULATION

2.1 Problem settings

In this chapter, the mathematical formulation for a two dimensional plane strain fracture is presented. We formulate the relationship between stress and displacement considering the stress field is broken up into its component of Mode I and Mode II. Mode I causes the crack to open and results in changes of normal stress along the fracture plane. Whereas Mode II causes the crack surfaces to slip relative to each other and results in shear stress redistribution along the fracture plane. Throughout this study, we adopt the sign convention that compressive stresses and right-lateral shear stresses are positive.

In this thesis we consider a one-way interaction of a hydraulic fracture and a shear fracture. Stress/ pore pressure perturbation by the hydraulic fracture is considered as an agent of slip on the shear fracture. But the stress perturbation induced by slip on the shear fracture is assumed to be inconsequential for the hydraulic fracture propagation. Specifically, this approach is expected to be approximately applicable when the length of the hydraulic fracture is much larger than the slipping patch or if the hydraulic and shear fracture are on the same plane (e.g., hydraulic fracturing along the fault plane).

We first define the model of a KGD crack without a lag followed by the model of a semi-infinite HF with the lag where the latter is looked at as a “refinement” of the former near the tip. Indeed, the latter provides the details of how the tip behavior evolves to the "no-lag" behavior (i.e., $w \sim X^{2/3}$) with increasing distance from the tip. The lag is likely to play a small role in both models (see Chapter 3 and Chapters 4-5). We have chosen to account for it in the latter and not in the former, but essentially did not have to. (A practical reason to have a more accurate, i.e. non-

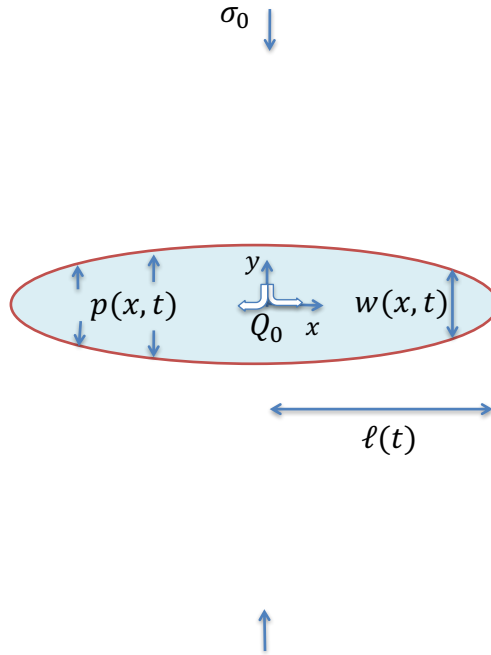


Figure 2.1: Finite plane strain hydraulic fracture with length 2ℓ

zero lag, solution in the case of Chapter 4-5 is to avoid dealing with stress singularities at the hydraulic fracture tip when it intersects the natural fracture).

2.2 Hydraulic fracture

2.2.1 Finite (KGD) hydraulic fracture

Consider a hydraulic fracture of length 2ℓ propagating in a linearly elastic, homogeneous impermeable rock. The hydraulic fracture loaded with the fluid pressure p is driven by fluid injection with the constant flow rate Q_0 at the crack center and is aligned with the x axis taken perpendicular to the minimum in-situ stress σ_0 (Figure 2.1). The governing equations describing propagation of the fracture are summarized below¹.

¹The detailed derivation can be found in Appendix A.

Fracture opening

The elasticity equation relates the crack opening w to the net fluid pressure $p - \sigma_0$ along the fracture plane [94]:

$$p(x, t) - \sigma_0 = -\frac{E'}{4\pi} \int_{-\ell}^{\ell} \frac{\partial w}{\partial s} \frac{ds}{x - s}, \quad (2.1)$$

where the plane strain modulus $E' = E/(1 - \nu^2)$ relates to the Young's modulus E and the Poisson's ratio ν .

Fluid continuity

The governing equations for the flow of a Newtonian fluid within the fracture are given by the Poiseuille's law for the fluid flow velocity averaged across the gap

$$v = -\frac{w^2}{12\mu} \frac{\partial p}{\partial x}, \quad (2.2)$$

where μ is the dynamic viscosity of the fluid, and the fluid continuity equation in the absence of leak-off

$$\frac{\partial w}{\partial t} + \frac{\partial vw}{\partial x} = 0. \quad (2.3)$$

The assumption of negligible lag between the fluid front and the hydraulic fracture tip implies that there are no boundary conditions on the fluid pressure there. This is known to lead to an infinite suction ($p \rightarrow -\infty$) at very small distances from the tip [40, 41], which are assumed inconsequential for slip development on a larger spatial scale. (see references: Garagash [44] for lag estimate, and Uenishi and Rice [73], Garagash and Germanovich [64] for slip patch scaling)

Fracture propagation

Note that this thesis will be dealing with the opening mode HF under assumption of negligible toughness, which will be further justified in Chapters 3, 4.

Based on linear elastic fracture mechanics, the tip asymptote for the fracture opening is given by [95]:

$$w/(\ell - |x|)^{1/2} \rightarrow 0, \quad |x| \rightarrow \ell^- \quad (2.4)$$

The boundary condition are given by

$$wv = \pm \frac{Q_0}{2}, \quad \text{at } x = 0^\pm \quad (2.5)$$

at the fluid inlet, and

$$w = 0, \quad v = \pm \dot{\ell}, \quad \text{at } x = \pm \ell \quad (2.6)$$

at the fracture front, where $\dot{\ell} = d\ell/dt$ is the fracture front velocity. The initial conditions are given by:

$$\ell = 0, \quad w = 0, \quad \text{at } t = 0. \quad (2.7)$$

2.2.2 Semi infinite hydraulic fracture with a lag

The governing equations for a semi-infinite hydraulic fracture with a lag of constant length ℓ_{tip} and propagating at constant velocity V are summarized below (Figure 2.2).

The elasticity equation (2.1) along the plane of fracture takes the form of

$$p(x, t) - \sigma_0 = \frac{E'}{4\pi} \int_{-\infty}^{x_{tip}} \frac{\partial w}{\partial s} \frac{ds}{x - s} \quad (2.8)$$

where x_{tip} is the tip position. With transforming of the fixed coordinate system (x, y)

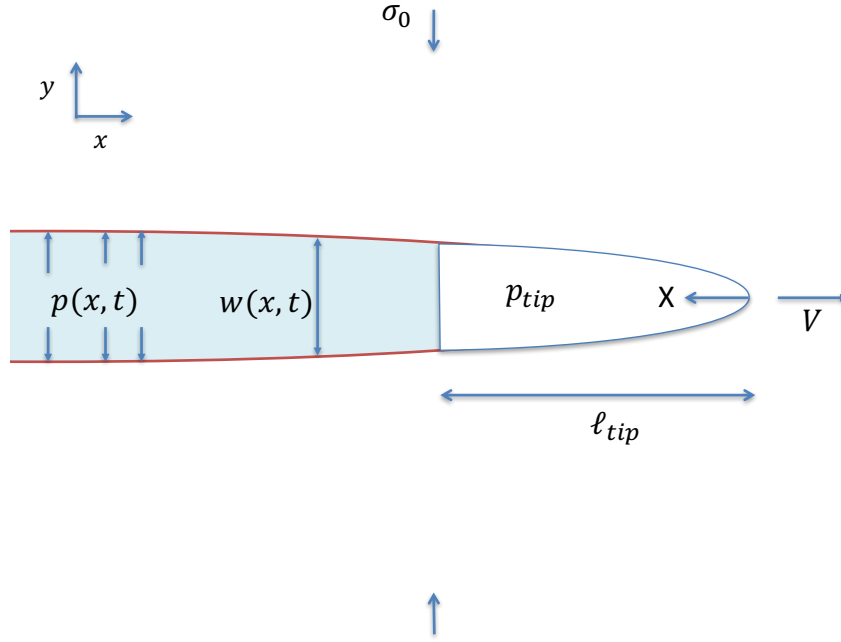


Figure 2.2: Semi-infinite plain strain hydraulic fracture with lag of length λ

to “moving with crack tip” coordinate system (X, Y) by $X = x_{tip} - x = Vt - x$, the above equation becomes

$$p(X) - \sigma_0 = \frac{E'}{4\pi} \int_0^\infty \frac{\partial w}{\partial s} \frac{ds}{X - s}. \quad (2.9)$$

Upon integrating the continuity equation (2.3) and for the case of steady propagation, the lubrication equations transforms to

$$w^2 \frac{dp}{dX} = 12\mu V \quad \ell_{tip} < X < \infty \quad (2.10)$$

In the lag region, pressure is constant:

$$p = p_{tip} \quad 0 \leq X \leq \ell_{tip} \quad (2.11)$$

The fracture opening close to the tip is given by the classical elastic square root

asymptote

$$w/X^{1/2} \rightarrow 0, \quad X \rightarrow 0 \quad (2.12)$$

2.3 Shear fracture

Consider a preexisting shear fracture of length $2a$ in a linearly elastic, homogenous rock under spatially non-uniform, HF-perturbed, background normal $\sigma_b(x, y)$ and shear stress $\tau_b(x, y)$ (Figure 2.3).

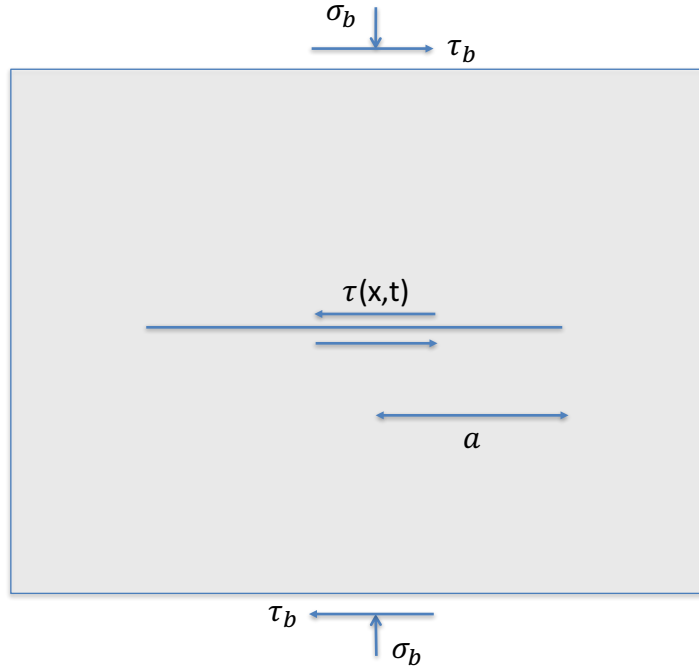


Figure 2.3: Pre-existing plain strain shear fracture with length $2a$

The equation of quasi-static elastic equilibrium relates the change of the shear stress on the crack plane to the slip δ by:

$$\tau(x, t) - \tau_b(x, t) = -\frac{E'}{4\pi} \int_{-a(t)}^{+a(t)} \frac{\partial \delta(s, t)}{\partial s} \frac{ds}{x-s}. \quad (2.13)$$

The finite stress (i.e., vanishing stress intensity factors), or a vanishing slip gradient at the tips of a crack requires [95]:

$$\int_{-a(t)}^{+a(t)} \frac{\tau(x, t) - \tau_b(x, t)}{\sqrt{a(t)^2 - x^2}} dx = 0, \quad \int_{-a(t)}^{+a(t)} \frac{\tau(x, t) - \tau_b(x, t)}{\sqrt{a(t)^2 - x^2}} x dx = 0 \quad (2.14)$$

Note that for a symmetric crack the second equation is automatically satisfied.

The shear stress is equal to the shear strength along the crack

$$\tau = f(\delta)(\sigma_b - p) \quad (2.15)$$

where $(\sigma_b - p)$ is the effective stress.

Friction f is assumed to weaken with slip δ . Specifically, we make use of a linear slip-weakening model in which f decreases linearly with slip from its peak f_p to the residual f_r value attained at $\delta_r = (f_p - f_r)/W$ [66]:

$$f(\delta) = \begin{cases} f_p - W\delta, & \delta \leq \delta_r \\ f_r, & \delta > \delta_r, \end{cases} \quad (2.16)$$

where W [$1/L$] is the slip-weakening slope (Figure 2.4). A slip-weakening distance, which is independent of the particular residual level of friction, can be defined as the value of slip

$$\delta_w = f_p/W \quad (2.17)$$

at which the friction would vanish if allowed an unlimited weakening (Figure 2.4).

2.4 Undrained pore pressure field

Undrained pore pressure regime or response denotes the condition where the time scale characteristic of the loading is too short for the diffusivity process and for fluid movement to occur within the rock matrix. This is in contrast with the drained pore

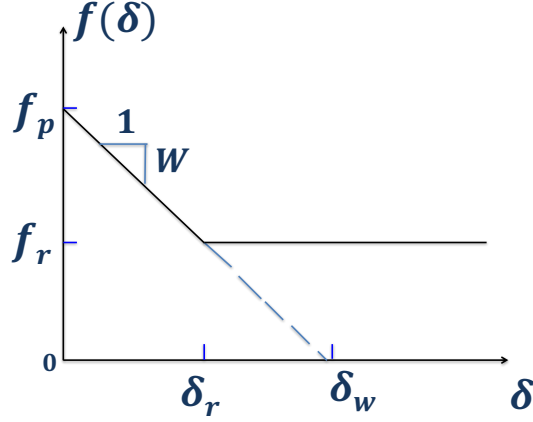


Figure 2.4: Slip weakening friction.

pressure response which characterizes the conditions when the excess pore pressure has time to dissipate and the pore pressure has returned to its ambient value.

The ratio of the induced pore fluid pressure, Δp , to the change in the applied stress (i.e., confined pressure), $(\Delta\sigma_{xx} + \Delta\sigma_{yy} + \Delta\sigma_{zz})/3$, under undrained condition (or in impermeable rock) is denoted by the Skempton's coefficient B , $\Delta p = B(\Delta\sigma_{xx} + \Delta\sigma_{yy} + \Delta\sigma_{zz})/3$. The Skempton's coefficient B ranges between 0.4 and 1 for water-saturated rocks [87]. For the case of plane strain with $\Delta\sigma_{zz} = \nu_u(\Delta\sigma_{xx} + \Delta\sigma_{yy})$, the relation takes the form of:

$$\Delta p_{und} = B(1 + \nu_u)(\Delta\sigma_{xx} + \Delta\sigma_{yy})/3. \quad (2.18)$$

where ν_u is the undrained Poisson's ratio.

CHAPTER 3: NUCLEATION OF DYNAMIC SLIP ON A HYDRAULICALLY FRACTURED FAULT

In this chapter, we investigate slip development and potential instability along a hydraulically fractured fault. The physical model for a HF propagating along a fault is presented in Section 3.1, followed by the mathematical treatments of the hydraulic fracture and related elastic stress perturbation along the fault (Section 3.2), and of the fault slip induced by the HF (Section 3.3), respectively. Section 3.4 presents the main results for the nucleation of the dynamic slip, followed by the discussion in Section 3.5 of the physical scales of the HF-induced slip instability on natural faults¹.

3.1 Model

We consider a hydraulic fracturing injection at a constant volumetric rate Q_0 [L^2/T] into a two dimensional fault in an unbounded homogenous elastic medium with ambient pore pressure of p_0 and the remote normal σ_0 and shear τ_0 stresses resolved on the fault plane (Figure 3.1).

The hydraulic fracture propagates due to the injection of the pressurized fluid into the fault, which in return activates the shear mode (slip) propagation. As the fluid is injected, slip (relative shear displacement) will take place along the fracture plane due to zero frictional strength in the open portion of the crack, and fault strength ahead of the hydraulic fracture tips will be diminished due to the compressive normal stress reduction there. We neglect the fluid leak-off from the hydraulic fracture into surrounding rock, and similarly neglect the pore pressure diffusion and pore

¹The model and the results in this chapter have been published by AGU. Copyright (2017) American Geophysical Union.

"Azad, M., D. I. Garagash, and M. Satish (2017), Nucleation of dynamic slip on a hydraulically fractured fault, J. Geophys. Res. Solid Earth, 122, doi:10.1002/2016JB013835"

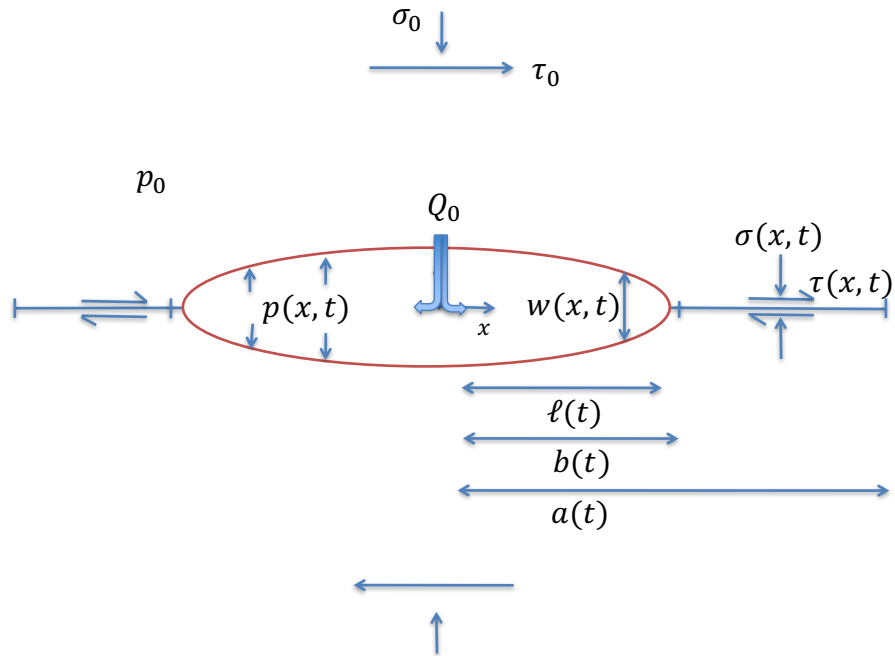


Figure 3.1: Hydraulic fracture (HF) with an open half-length $\ell(t)$ is driven along a fault by a constant rate of fluid injection Q_0 at the inlet. The fault slipping patch is characterized by the half-length $a(t)$, and the “frictionless” half-length $b(t)$ ($a > b > \ell$). The latter encompasses the open crack with half-length ℓ and the small regions of extent $b - \ell$ just outside of the HF tips where the effective normal stress is tensile as the result of the singular stress perturbation induced by the open crack. The fault lies parallel to the x axis and is oblique to the far-field principal stresses, which result in background values of the normal, σ_0 , and shear, τ_0 , stresses resolved on the fault plane.

fluid flow in the rock. Consequently, the pore pressure perturbation ahead of the hydraulic fracture tips is undrained. This assumption approximately holds if the rate of hydraulic fracture propagation is higher than the rate of pore pressure diffusion in the rock ahead of the hydraulic fracture front.

As the result of fluid injection, the fault undergoes opening $w(x, t)$ and slip $\delta(x, t)$. The open part (hydraulic fracture), characterized by half-length $\ell(t)$, is embedded into the slipping part (shear fracture) with half-length $a(t)$, ($a > \ell$).

Denote the normal and shear stresses as $\sigma = \sigma_{yy}$, $\tau = \sigma_{xy}$. Along the open-part of the fault (hydraulic fracture), the normal stress is given by the fluid pressure p ,

$$|x| < \ell(t) : \quad w(x, t) > 0, \quad \sigma(x, t) = p(x, t). \quad (3.1)$$

Along the slipping part of the fault, the shear stress is given by the fault frictional strength

$$|x| < a(t) : \quad \tau = \tau_{fault} = f(\delta)[\sigma - p] \quad (3.2)$$

where $[\sigma - p] = \sigma - p$ when $\sigma - p > 0$ (compressive) and $[\sigma - p] = 0$ otherwise. Shear stress borne in the viscous fluid occupying the open part of the slipping fault (HF) is normally very small compared to the frictional strength of the closed part of the slipping patch, and is, therefore, neglected in (3.2). In other words, the hydraulically fractured part of the fault offers no resistance to slip in our model. We also recognize existence of a tensile region $(\sigma - p) \leq 0$ immediately ahead of the hydraulic fracture front $\ell < |x| < b$, which extends the frictionless region beyond the HF tips. As we will show further, the extent $b - \ell$ of this segment of the frictionless region is however very small compared to the fracture dimensions.

The pore pressure p ahead of the hydraulic fracture is reduced from its ambient level p_0 due to poroelastic rock/fault gouge dilation. The undrained (instantaneous) value of the pore pressure perturbation is linked to the mean stress change, and can be

expressed along the fault plane outside of the plane strain hydraulic fracture as

$$(p - p_0)_{\text{und}} = B'(\sigma - \sigma_0), \quad |x| > \ell \quad (3.3)$$

The plane strain Skempton's coefficient $B' = \frac{2}{3}B(1 + \nu_u)$ relates to the Skempton's coefficient B , ranging between 0.4 and 1 for water-saturated rocks [87], and to the undrained Poisson's ratio $\nu_u \sim 0.3$. Fault slip will also generally lead to a change of the pore pressure about the fault plane, but this change is perfectly antisymmetric (identical magnitudes of the increase/decrease of the pore pressure on the compressional/extensional sides of the fault) if the mechanical and hydraulic properties of the host rock and gouge are either homogeneous or more generally symmetrically-distributed across the fault [96]. Given the asymmetry of the pore pressure change due to slip under stated conditions, it remains exactly zero at the slip surface (or at the center of a finite sheared gouge zone accommodating slip) and does not appear in (3.3).

When the rock properties are the same on both sides of the fault, the opening and shear fracture modes are only one-way coupled. Slip does not affect the normal stress distribution along the fracture plane and hence does not affect the hydraulic fracture (opening mode) propagation. However, the opening mode affects the slip on a frictional fault by altering the normal stress, leading to (i) zero frictional strength along the open part of the rupture; and (ii) reduced frictional strength ahead of the open crack tips. As a result, the hydraulic fracture problem can be addressed independently of the fault slip problem.

In the following, the mathematical formulation of both modes of fault displacement, as well as the dimensionless forms of their corresponding equations, will be introduced. It will then be discussed how the solution of the hydraulic fracture problem may be used to solve the fault slip problem.

3.2 Fault Opening Development (Hydraulic Fracture)

The governing equations for a propagating plane strain hydraulic fracture were summarized in section (2.2.1).

Elasticity equation relates the crack opening w to the normal stress change $\sigma - \sigma_0$ along the fracture plane (equation 2.1). Along the hydraulic fracture $|x| \leq \ell$, $\sigma = p$, and the above equation yields the net fluid pressure distribution $p - \sigma_0$.

The slip ahead of the hydraulic fracture front is assumed to break the rock resistance and nullify the opening-mode fracture toughness, $K_{Ic} = 0$.

This fully defines the zero-toughness solution for the hydraulic fracture half-length $\ell(t)$, opening $w(x, t)$ and the net fluid pressure $p(x, t) - \sigma_0$ along the fracture, $|x| \leq \ell$, and normal stress change $\sigma(x, t) - \sigma_0$ outside of it, $|x| > \ell$, as functions of injection rate Q_0 , fluid viscosity parameter μ' ($= 12\mu$) and the elastic modulus E' [49, 42, 43]. Assuming the zero-toughness condition, the tip asymptote of the solution assumes the form distinct from the classical fracture mechanics $w \sim X^{1/2}$ [41] characterized by crack tip opening

$$w = 2^{1/3} 3^{5/6} (\mu' \dot{\ell} / E')^{1/3} (\ell - |x|)^{2/3}, \quad |x| \rightarrow \ell^- \quad (3.4)$$

and weak tensile fluid pressure/stress singularities

$$\sigma - \sigma_0 = -6^{-2/3} (\mu' \dot{\ell} E'^2)^{1/3} \begin{cases} (\ell - |x|)^{-1/3}, & |x| \rightarrow \ell^- \\ 2 \times (|x| - \ell)^{-1/3}, & |x| \rightarrow \ell^+ \end{cases} \quad (3.5)$$

as the crack tip is approached from the inside/outside. We note that the change of the value of the stress singularity prefactor in (3.5) when the HF tip is approached from the inside/outside have not been exposed previously. Yet it does follow directly from the stress representation in terms of the monomial form of the complex-valued

elastic potential function of Desroches et al. [41].

Zero-toughness, zero leak-off hydraulic fracture solution

Scaling considerations for the case of negligible toughness and fluid leak-off show that the solution is self-similar [97]:

$$\ell(t) = L(t)\gamma, \quad w(x, t) = \varepsilon(t)\ell(t)\bar{\Omega}(\xi), \quad \sigma(x, t) - \sigma_0 = \varepsilon(t)E'\Pi(\xi) \quad (3.6)$$

where $\xi = x/\ell(t)$ is the similarity variable and

$$L(t) = \frac{E'^{1/6}Q_0^{1/2}t^{2/3}}{\mu'^{1/6}}, \quad \varepsilon(t) = \left(\frac{\mu'}{E't}\right)^{1/3} \quad (3.7)$$

are the crack length scale and small non-dimensional parameter, respectively.

The solution for dimensionless hydraulic fracture half-length $\gamma \simeq 0.615$, crack opening $\bar{\Omega}(\xi)$, and stress change $\Pi(\xi)$ along the fracture, $|\xi| < 1$, in scaling (3.6) were obtained by Adachi and Detournay [43], with some of the relevant solution details recounted in Appendix B. The Appendix also extends their stress change solution to the entire fault plane. Figure 3.2 illustrates the normalized self-similar opening and stress change profiles contrasted near the tip to their asymptotic forms, as follows from (3.4) and enriched form of (3.5):

$$\Omega = 2^{2/3}3^{1/2}(1-|\xi|)^{2/3}, \quad |\xi| \rightarrow 1^-, \quad \Pi = \begin{cases} -2^{-1/3}3^{-1}(1-|\xi|)^{-1/3} + \Pi_{\text{const}}, & |\xi| \rightarrow 1^- \\ -2 \times 2^{-1/3}3^{-1}(|\xi| - 1)^{-1/3} + \Pi_{\text{const}}, & |\xi| \rightarrow 1^+ \end{cases} \quad (3.8)$$

Here $\Pi_{\text{const}} \approx 0.7508$ is the next order (constant) term in the near tip stress expansion of the Adachi and Detournay's solution (Appendix B).

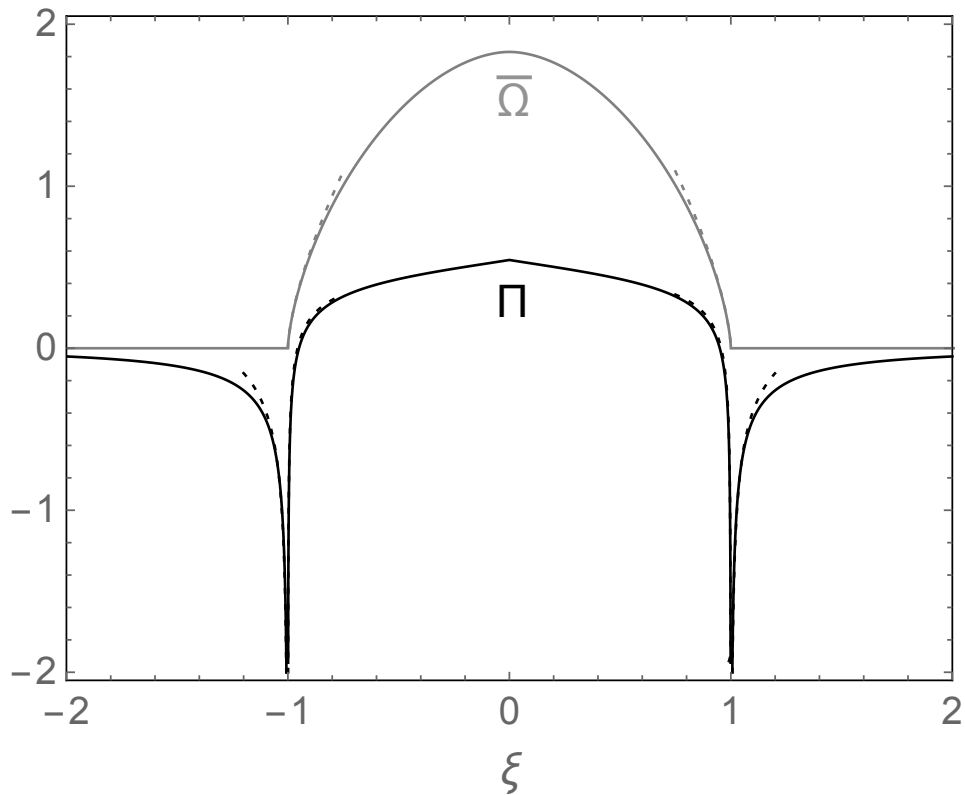


Figure 3.2: Self-similar solution for the hydraulic fracture normalized opening $\bar{\Omega} = w/\varepsilon\ell$ and stress change $\Pi = (\sigma - \sigma_0)/\varepsilon E'^{-1}$ as a function of normalized distance x/ℓ (Carbonell et al., [42]; Adachi and Detournay [43]). Time dependent length L ($\ell \simeq 0.615L$) and stress $\varepsilon E'^{-1}$ scales are defined in (3.7). The dashed lines show the HF tip asymptotics (3.8).

3.3 Fault Slip Development

3.3.1 Governing equations

The equations governing slip on the fault plane are summarized in section (2.3).

The shear stress along the crack, $|x| < a$, is given by the fault frictional strength (3.2), $\tau = f(\delta)[\sigma - p]$. Thus, the coupling of the slip to the opening-mode fracture (hydraulic fracture) is through the effective stress $\sigma - p$, which can be expressed in view of equation (3.6) for total stress change $\sigma - \sigma_0$ and equation (3.3) for the undrained pore pressure change ahead of the hydraulic fracture tip $p - p_0$, as:

$$\sigma - p = \sigma_0 - p_0 + (1 - B')\varepsilon(t)E'\Pi\left(\frac{x}{\ell(t)}\right), \quad |x| > \ell(t) \quad (3.9)$$

A characteristic slipping patch length can be defined in relation to the characteristic slip value $\delta_w = f_p/W$, (2.17), as

$$a_w = \frac{E'}{2\tau_p}\delta_w \quad (3.10)$$

where $\tau_p = f_p(\sigma_0 - p_0)$ is the peak ambient value of the shear strength.

In the following, it will prove convenient to use a normalized form of the effective stress perturbation introduced by the hydraulic fracture, (3.9), cognizant of the lengthscale of interest a_w :

$$\frac{\sigma - p}{\sigma_0 - p_0} - 1 = \lambda \left(\frac{\ell(t)}{a_w}\right)^{-1/2} \Pi\left(\frac{x}{\ell(t)}\right), \quad |x| > \ell(t) \quad (3.11)$$

Here λ is a dimensionless hydraulic fracture loading factor

$$\lambda = \frac{(1 - B')\varepsilon(t_w)E'}{\sigma_0 - p_0} = (2\gamma)^{1/2} (1 - B') \frac{E'^{1/4} \mu'^{1/4} Q_0^{1/4} f_p^{1/2}}{(\sigma_0 - p_0)^{1/2} \delta_w^{1/2}}, \quad (2\gamma)^{1/2} \approx 1.109 \quad (3.12)$$

which characterizes the magnitude of the effective stress perturbation ahead of the HF tip relative to the ambient effective stress value at the time t_w when the HF has grown to the characteristic size a_w , i.e., $\ell(t_w) = a_w$.

3.3.2 Solution for the fault's slip

To facilitate the numerical solution for the slip, we make use of characteristic crack length a_w , (3.10), and slip weakening distance δ_w , (2.17), to nondimensionalize the shear crack length a and slip δ , respectively. Normalized solution for δ/δ_w and a/a_w as a function of normalized position along the crack $X = x/a$ (slip only) and the normalized HF length $\ell(t)/a_w$, which embodies the problem dependence on the injection time, is governed by the normalized form of the governing equation (2.13)-(3.9) given in Appendix C. The normalized solution depends on the following three parameters: the normalized background shear stress τ_0/τ_p , residual to peak friction ratio f_r/f_p and the hydraulic fracture loading factor λ , (3.12).

The numerical solution is computed using a piecewise constant slip distribution method. Selected results are further validated by an alternative solution method corresponding to an expansion of the slip distribution into a series of Chebyshev's polynomials. Details of numerical implementations can be found in Appendix A of *Garagash and Germanovich* [64]. The numerical calculations explore the full range of the background shear stress, $0 < \tau_0/\tau_p < 1$, for two choices of the residual friction values, namely, $f_r/f_p = 0$ (unlimited weakening) and $f_r/f_p = 0.6$, and the various values of the HF loading factor $\lambda \leq 1$. Values of physical parameters pertaining to the field are discussed in Section 3.5.

3.4 Results

At the start of the injection, $t = 0$, the extent of the open portion (hydraulic fracture) is zero and the entire fault is at its ambient peak strength τ_p , $\tau_p > \tau_0$, which indicates

a non-slip condition. The injection opens the fault over length $2\ell(t)$ at $t > 0$ which causes reduction of the fault strength to zero along the hydraulic fracture and to a diminished value ahead of the hydraulic fracture tips. This activates the slip on the fault and causes the slipping patch $2a(t)$ extension with the continuing injection. Note that the time dependence of the solution follows directly from that of the hydraulic fracture half-length $\ell(t)$, (3.6)-(3.7).

The effective normal stress distribution $\sigma - p$ is given by the hydraulic fracture solution, (3.9). Figure 3.3a shows an example of the normalized effective normal stress for a particular value of the hydraulic fracture loading parameter, $\lambda = 0.2$, and normalized hydraulic fracture length $\ell/a_w = 0.1$. The effective stress is null along the hydraulic fracture, $|x| < \ell(t)$, and singular just outside of the hydraulic fracture tips, (3.5), resulting in a tensile region ahead of the hydraulic fracture tips $\ell(t) < |x| < b(t)$. The effective normal stress ahead of the hydraulic fracture increases from a negative (tensile) singularity towards the ambient (compressive) value $\sigma_0 - p_0$, as the distance from the tip increases.

The extent of the region with tensile effective stress ahead of the hydraulic fracture tip, $b - \ell$, is obtained from (3.11) by setting $\sigma - p = 0$ at $x = b$, in the implicit form $\Pi(b/\ell) = -(1/\lambda)(\ell/a_w)^{1/2}$. The evolution of tensile region length $b - \ell$ with hydraulic fracture advance is exemplified on Figure 3.3b for the case with $\lambda = 0.2$. It is apparent that the tensile region is typically very small compared to the hydraulic fracture half-length, $b - \ell \ll \ell$. The first order estimate of b can, therefore, be obtained from the near tip stress asymptote (by requiring $\sigma - p = 0$ at $x = b$), dimensionless form of which is given in (3.5), as

$$\frac{b}{\ell} = 1 + \frac{4}{27} \left(\Pi_{\text{const}} + \frac{1}{\lambda} \sqrt{\frac{\ell}{a_w}} \right)^{-3} \quad (3.13)$$

The latter approximation is shown on Figure 3.3b by the dashed line.

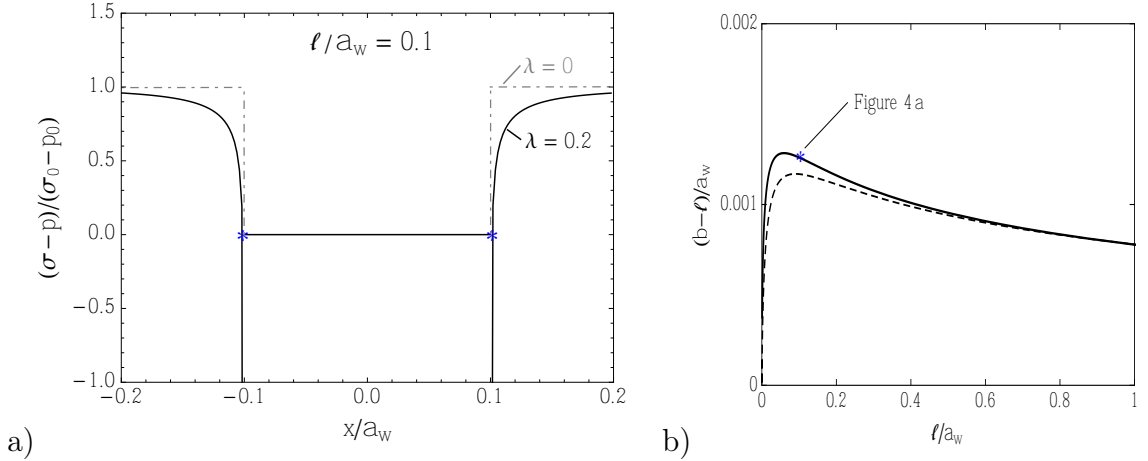


Figure 3.3: (a) Example of the effective normal stress distribution for two values of the HF loading factor $\lambda = 0, 0.2$ and the HF half-length $\ell = 0.1a_w$. (b) Development of the tensile effective stress region ahead of the hydraulic fracture tip, $b - \ell$, with the growth of the hydraulic fracture length ℓ for the case with $\lambda = 0.2$. The asymptotic form of tensile effective stress region extension is shown by dashed line (3.13). The frictionless tips, $|x| = b(t)$, indicated by stars in (a), are nearly coincident with the hydraulic fracture tips $|x| = \ell(t)$, i.e. $b/\ell \simeq 1$.

The fault frictional strength, (3.2), is zero along the hydraulic fracture and the tensile region ahead of the hydraulic fracture tip $|x| \leq b(t)$; and it increases from zero at $|x| = b(t)$ to the peak value $\tau_p = f_p(\sigma - p)$ at the shear crack tips, $|x| \rightarrow a(t)$.

In the following, the numerical solution of the proposed problem will be discussed. First, the results of a model in which friction is allowed to decrease unlimitedly with slip (i.e., $f \rightarrow 0$ as $\delta \rightarrow \delta_w$) will be presented, and then, the results of a more realistic model in which the friction saturates at a non-zero residual value f_r at large enough slip will be shown.

3.4.1 Slip on a fault with unlimited weakening

Extent $a - \ell$ of the slipping patch ahead of the hydraulic fracture tip is shown on Figure 3.4a as a function of the hydraulic fracture half-length ℓ for the loading factor $\lambda = 0.2$ and different values of the background shear stress. Nucleation of dynamic slip on the fault occurs when a small increase in the hydraulic fracture length results

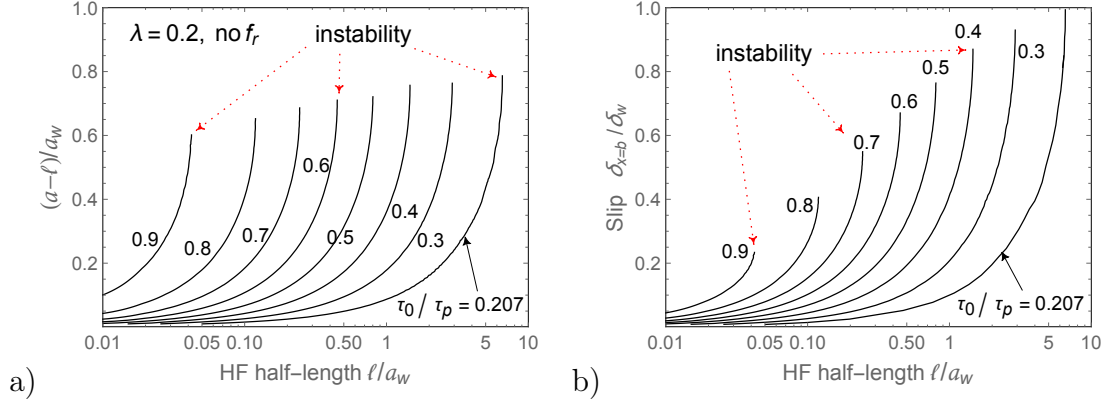


Figure 3.4: Development of (a) the slipping patch ahead of the hydraulic fracture tip, $(a - \ell)/a_w$, and (b) peak slip in the frictional patch $\delta_{x=b}$ with the growth of the hydraulic fracture half-length ℓ for the hydraulic fracture loading factor $\lambda = 0.2$ and different values of the background shear stress, as indicated for each curve. Termination points of the curves correspond to the vertical slope and signify the instability of the quasi-static crack growth.

in a large increase of the shear crack length (i.e., $da/d\ell \rightarrow \infty$ in the quasi static model) and corresponds to the points with the vertical slope on Figure 3.4a. Once the nucleation takes place, the quasi-static solution is not valid and the dynamic slip formulation should be implemented to model dynamic rupture. The extent of the closed part of the crack at the instability $a_c - \ell_c$, scales with a_w while length of the hydraulic fracture at the slip instability, ℓ_c , increases with decreasing background stress.

Figure 3.4b shows the development of slip at the frictionless tips $\delta_{x=b(t)}/\delta_w$ with the hydraulic fracture growths. Critical slip $(\delta_{x=b})_c/\delta_w$ increases with reduction of the background stress. Unlimited weakening model fails before nucleation when $\delta > \delta_w$ (or $f < 0$), which takes place for small values of the shear loading ($\tau_0/\tau_p < 0.207$, Figure 3.4b).

Figure 3.5 shows the development of the slip and the shear stress along the fault at different stages of the hydraulic fracture growth for the background stress $\tau_0/\tau_p = 0.7$. The shear stress drops from its peak at the shear crack tips towards the center of the crack and becomes zero for the hydraulically fractured part of the fault. Outside of

the slipped portion of the fault, the shear stress diminishes with distance from the tips and approaches the background shear stress at infinity. Profiles of the normalized normal stress and opening distributions for the same stages of the hydraulic fracture propagation are shown in Figure 3.5c and 3.5d.

3.4.2 Condition for nucleation of dynamic slip

Some of the fault characteristics at the instability can be obtained from the eigenvalue analysis [98, 73, 64], which allows to forgo the full fault slip solution. Differentiation of equation (2.13) with time and taking the nucleation limit, $t \rightarrow t_c$, results in:

$$\frac{a_c}{a_w} v(X) \frac{[\sigma - p](a_c X, t_c)}{\sigma_0 - p_0} = \frac{1}{2\pi} \int_{-1}^1 \frac{\partial v(s)}{\partial s} \frac{ds}{X - s} \quad (3.14)$$

where $X = x/a$ is the normalized coordinate along the slipping patch and the diverging slip rate $\dot{\delta} = \partial\delta/\partial t$ has been normalized using its root mean square:

$$v(X) = \lim_{t \rightarrow t_c} \frac{\dot{\delta}(aX, t)}{\sqrt{\frac{1}{2} \int_{-1}^1 \dot{\delta}^2(aX, t) dX}}. \quad (3.15)$$

Equation (3.14) is a linear homogenous equation for the normalized slip velocity distribution $v(X)$ when the effective normal stress $\sigma - p$ is known along the crack. The critical normalized half-length a_c/a_w , which corresponds to the smallest eigenvalue solution of equation (3.14), depends on the two parameters which describe the normalized effective normal stress field (3.11) in equation (3.14): the normalized critical hydraulic fracture half-length ℓ_c/a_w and the loading factor λ . In the limit of the uniform distribution of effective normal stress along the crack $\sigma_0 - p_0$ (negligible hydraulic fracture extent), the problem reduces to the eigenvalue problem solved by Uenishi and Rice [73] where the critical crack length approaches $a_c/a_w \simeq 0.579$. Figure 3.6 shows the crack half-length versus the hydraulic fracture half-length at

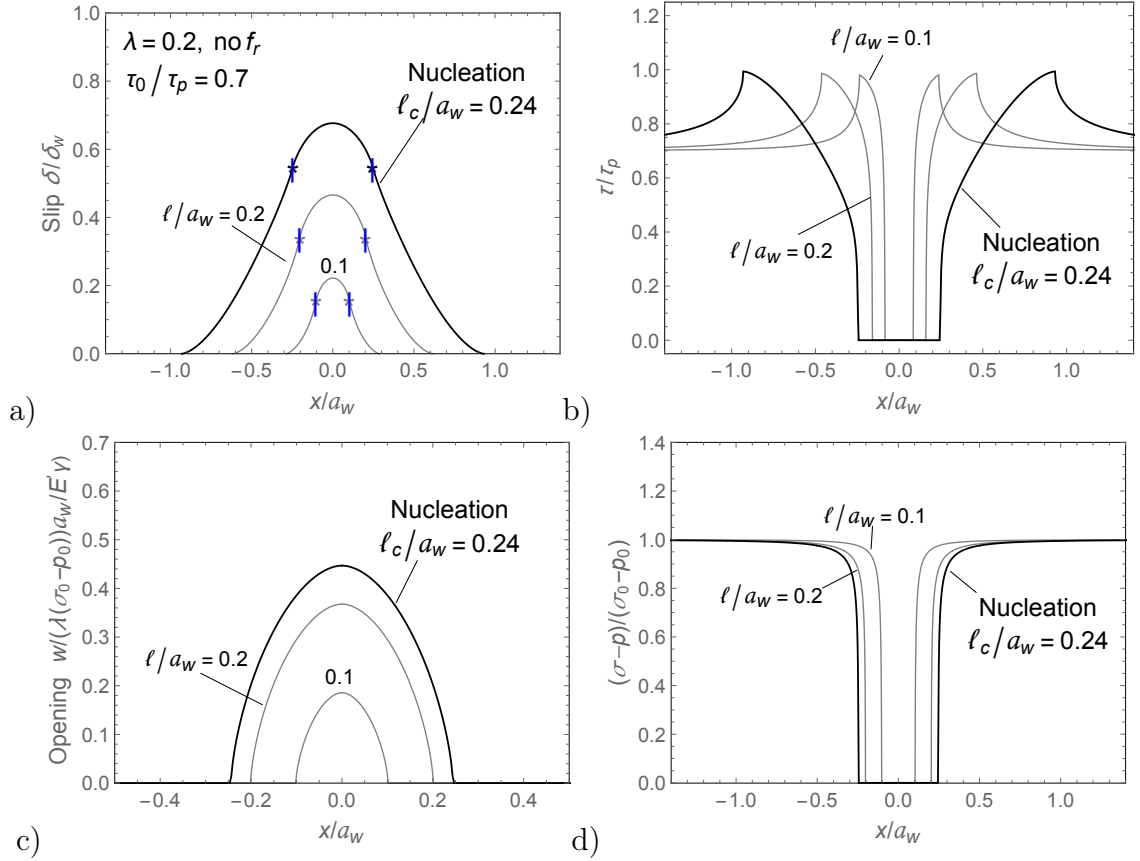


Figure 3.5: Development of the normalized slip distribution, (a), the normalized shear stress distribution, (b), the normalized hydraulic fracture opening distribution, (c), and the normalized effective normal stress distribution, (d), along the fault during the hydraulic fracture propagation for loading factor value $\lambda = 0.2$ and background shear stress $\tau_0/\tau_p = 0.7$. Blue arrows and stars correspond to the nearly coincident hydraulic fracture, $|x| = \ell(t)$, and the frictionless, $|x| = b(t)$, tips, respectively. It can be seen that the extent of the segments where the effective normal stress is tensile, $b - \ell$, is practically negligible. The instability of the quasi-static crack growth is highlighted by heavier lines.

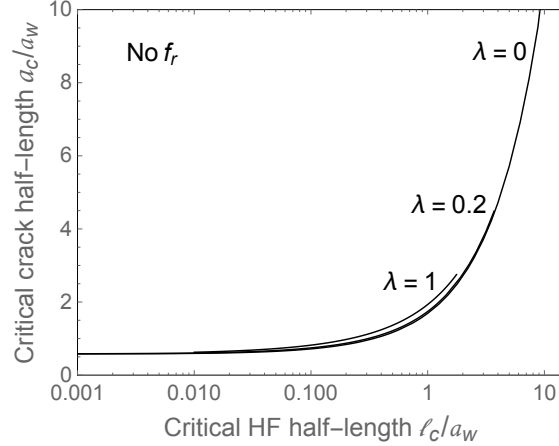


Figure 3.6: Shear fracture half-length vs. hydraulically open fracture half-length at the instability for various values of the loading factor $\lambda = 0, 0.2$ and 1 , as determined from Eigenvalue analysis. Eigenvalue analysis allows to establish relationship between nucleation crack size a_c and its open part ℓ_c , but not their relation to the background stress τ_0 .

the instability for various values of the loading factor $\lambda = 0, 0.2$ and 1 . As is the case of the full solution for the fault slip development (e.g., Fig 3.7), the eigenvalue solution for the critical crack half-length is weakly dependent on the loading factor λ . It should be noted that the magnitude of the corresponding background shear stress at nucleation can not be obtained from the eigenvalue analysis alone and requires the full solution of equations (2.13)-(3.9) for the time development of fault slip, as discussed next.

In order to investigate the effect of the loading parameter λ and the background stress τ_0 on the fault instability, the normalized critical crack half-length a_c/a_w and critical slip at the frictionless tips $(\delta_{x=b})_c/\delta_w$ have been plotted versus the fault understress $(\tau_p - \tau_0)/\tau_p$ for different values of the loading parameter in Figure 3.7. The case with $\lambda = 0$ corresponds to an idealization where hydraulic fracturing related stress-perturbation is confined to the open part of the crack, and is negligible outside of it. As shown, the critical crack half-length a_c/a_w and the critical hydraulic fracture half-length ℓ_c/a_w increase with the fault understress (or, conversely, decrease with the background shear stress) and only weakly dependent on λ . Smaller values of

the loading factor λ correspond to slightly larger a_c and ℓ_c . This means that when the perturbation of the normal stress ahead of the hydraulic fracture is smaller, the nucleation length is marginally larger. Similarly, the critical slip at the frictionless tips $(\delta_{x=b})_c/\delta_w$ is mostly controlled by the value of the background shear stress, and only weakly dependent on λ .

Nucleation in the limit of a critically-stressed fault ($\tau_0 \rightarrow \tau_p$), when only a small perturbation is required to activate fault slip and bring it to the instability, can be treated analytically following the approach of Garagash and Germanovich [64]. Specifically, in this limit the spatial extent of the perturbation (HF length ℓ) is vanishingly small compared to the slipping patch size a , and the effect of the former on fault slip can be modeled by an equivalent point force ΔP . The latter corresponds to the net (integrated along the fault) perturbation of the effective normal stress $\Delta(\sigma - p)$, which is equal to $-(\sigma_0 - p_0)$ for $|x| < \ell$ (consistent with the complete unloading of the fault along the HF length) and is approximated as zero elsewhere,

$$\Delta P(\ell) = - \int_{-\infty}^{\infty} \Delta(\sigma - p) dx \approx 2(\sigma_0 - p_0)\ell \quad (3.16)$$

Using the value of the point force at the instability, $\Delta P_c \approx 0.837(\tau_p - \tau_0)a_w/f_p$ [64], in expression (3.16) allows to evaluate the corresponding critical HF length ℓ_c , reported below together with the corresponding nucleation patch size a_c ,

$$\frac{\ell_c}{a_w} \approx 0.418 \frac{\tau_p - \tau_0}{\tau_p}, \quad \frac{a_c}{a_w} \approx 0.579 \quad (\tau_0 \rightarrow \tau_p) \quad (3.17)$$

This critically-stressed fault nucleation asymptote is consistent with the numerical solution on Fig. 3.7b in the corresponding range of small understress.

The model with unlimited weakening may be used to predict the nucleation of instability over a range of loading conditions when $(\delta_{x=b})_c \leq \delta_w$. The corresponding range of background stress where the model with unlimited friction weakening is adequate

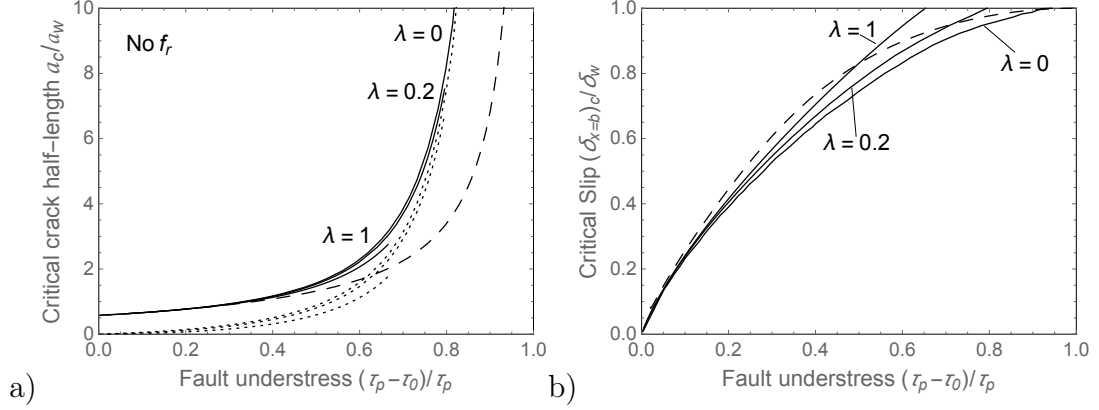


Figure 3.7: (a) Normalized shear crack half-length a_c/a_w and (b) the normalized slip at the frictionless tips $(\delta_{x=b})_c/\delta_w$ at the instability as functions of the fault understress $(\tau_p - \tau_0)/\tau_p$ for three values of the dimensionless loading factor $\lambda = 0$, $\lambda = 0.2$ and $\lambda = 1$. Normalized critical hydraulic fracture half-length at the instability ℓ_c/a_w is shown by dotted lines in (a). The reference solution for the instability under the incipient hydraulic fracture condition (i.e., injection fluid pressure is just below the normal stress) of Garagash and Germanovich [64] is shown by dashed line.

(i.e., results in $f \geq 0$) is wider for smaller values of the loading factor. For example, for loading factors $\lambda = 1$, this model leads to $(\delta_{x=b})_c > \delta_w$ and $f < 0$ and, thus, physically meaningful for the background stress $\tau_0/\tau_p \geq 0.35$, or, conversely, for the understress $1 - \tau_0/\tau_p \leq 0.65$ (Figure 3.7b).

3.4.3 Effect of residual friction on nucleation

Previous section has discussed the slip instability in the framework of the fault friction characterized by unlimited weakening. The latter model ceases to be an adequate description of fault strength for slips in excess of δ_w , when the model predicts negative friction. In a more realistic model, friction saturates at some non-zero residual value f_r for slips in excess of $\delta_r = (1 - f_r/f_p)\delta_w$ (Fig. 2.4). Thus, the fault responses with slips in excess of this threshold prompt reexamination. Taking, for example, $f_r/f_p = 0.6$, we can forecast based on Fig. 3.7b that the nucleation of dynamic slip will be affected by the residual fault strength for the understress values $1 - \tau_0/\tau_p \gtrsim 0.2$ (corresponding to $(\delta_{x=b})_c/\delta_w \geq 1 - f_r/f_p$). As shown by Garagash and Germanovich

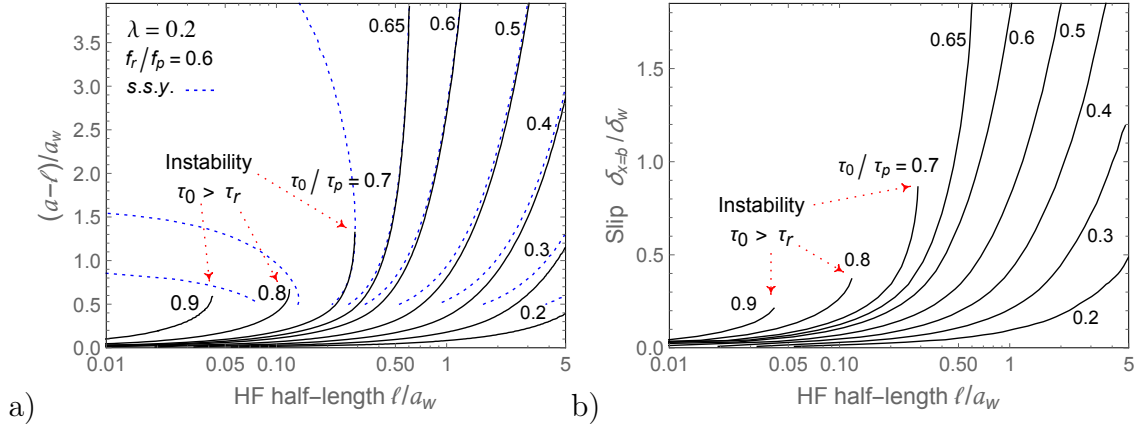


Figure 3.8: Growth of (a) the slipping segments ahead of the hydraulic fracture tips and (b) the normalized slip at the frictionless tips with the the hydraulic fracture advance in the model with residual friction $f_r/f_p = 0.6$, loading factor $\lambda = 0.2$ and for different values of background shear stress. The results are compared to the small scale yielding (s.s.y.) approximation (dotted lines) in (a). No dynamic instability is observed for values of the background stress below the ambient value of residual strength, $\tau_0/\tau_r < f_r/f_p = 0.6$.

[64] in the case of non-hydrofracture injection at a constant fluid overpressure, the existence of residual friction may lead to the stabilization of slip for large enough fault understress by either suppression of the instability or arrest of the nucleated dynamic slip.

Figure 3.8 illustrates the development of the slipping segments ahead of the hydraulic fracture tips $a - \ell$, (a), and of the normalized slip at the frictionless tips $\delta_{x=b}/\delta_w$, (b), as the hydraulic fracture propagates along a fault with residual friction $f_r/f_p = 0.6$, hydraulic fracture loading factor $\lambda = 0.2$, and different values of the background stress.

Figure 3.9 shows crack half-length a_c/a_w (a) and the slip at the frictionless tips $(\delta_{x=b})_c/\delta_w$ (b) at the instability as a functions of the fault understress $(\tau_p - \tau_0)/\tau_p$ in the model with the residual friction $f_r/f_p = 0.6$ and various values of the hydraulic fracture loading factor λ . The critical crack length and slip increase with diminishing τ_0 , and become unbounded when stress stability boundary ($\tau_0 = \tau_r$) is approached. The fault slip development remains stable when $\tau_0 < \tau_r$. Remarkably, the instability

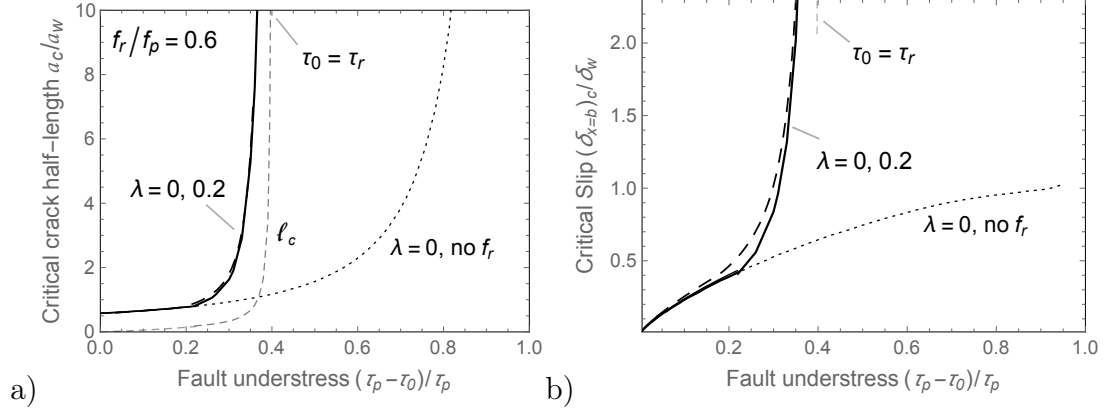


Figure 3.9: The normalized shear crack half-length a_c/a_w , (a), and the normalized slip at the frictionless tips $(\delta_{x=b})_c/\delta_w$, (b), at the instability as functions of the fault understress $(\tau_p - \tau_0)/\tau_p$ in the model with the residual friction $f_r/f_p = 0.6$ for two values of the loading factor $\lambda = 0, 0.2$. Corresponding half-length of the hydraulic fracture at instability ℓ_c/a_w is shown by dashed line in (a). (The dotted line shows the reference solution for the model with unlimited weakening ($f_r = 0$) for $\lambda = 0$). The solution is only weakly dependent on the loading factor. The hydraulic fracture induced slip on faults with $\tau_0 \leq \tau_r$ is unconditionally stable. The heavy dashed line shows the reference solution for the instability under the incipient hydraulic fracture condition of Garagash and Germanovich [64].

is very weakly dependent on the details of the fault loading by hydraulic fracturing or propagation regime thereof, as exemplified by the similarity of the solutions for various values of the HF loading factor λ to the solution in the incipient hydraulic fracture case (the injection pressure equal to the value of the normal stress resolved on the fault), studied previously by Garagash and Germanovich [64] and shown in Fig. 3.9 by the dashed line.

3.4.4 Small scale yielding analysis

When the crack length is large compared to the characteristic crack length a_w , the weakening of the shear strength with slip is localized to a small zone close to the crack tips and the small scale yielding condition (s.s.y.) [95] applies. Some useful examples of the s.s.y. analysis of geological shear fractures include Palmer and Rice

[67], Ampuero and Ben-Zion [99], Garagash and Germanovich [64], Viesca and Rice [62]. The simplified solution for the slip in our problem can be developed following Garagash and Germanovich [64, section 5.2]. Numerical solutions are compared to the s.s.y. approximation in Figure 3.8a. At high values of the background shear stress, the nucleation patch size $\sim a_w$ and the s.s.y. approximation is not applicable (i.e., the entire slipping patch is still undergoing weakening as the instability takes place). At moderate to low values of the background shear stress exceeding τ_r , the nucleation patch exceeds a_w and the s.s.y. solution provides an adequate approximation to the full solution.

Heeding the numerical observation that the fault slip is weakly influenced by the HF loading factor λ , we further simplify s.s.y. analysis by taking $\lambda = 0$, which then allows for an analytical expression for the energy release rate to propagate the shear crack

$$G = \frac{K^2}{E'}, \quad K = (\tau_0 - \tau_r)\sqrt{\pi a} + \frac{2}{\pi}\tau_r\sqrt{\pi a} \arcsin \frac{\ell}{a} \quad (3.18)$$

where K is the stress intensity factor (SIF), which general expression is given by Eq. (28) of Garagash and Germanovich [64]. The two terms in (3.18)_b correspond to the SIF value at the ambient fault conditions ($\sigma - p = \sigma_0 - p_0$ everywhere along the fault) and the correction along the HF ($\Delta(\sigma - p) = -(\sigma_0 - p_0)$ when $|x| < \ell$), respectively. Applying the shear crack propagation criteria, which specifies that the energy release rate G at the crack tip is to match the fracture energy $G^* = (\tau_p - \tau_r)\delta_r/2$, yields the simplified s.s.y. solution for the shear crack length a as a function of the HF length ℓ . The corresponding critical lengths at the nucleation (a_c and ℓ_c) are then obtained by requiring $da/d\ell \rightarrow \infty$.

The s.s.y. approximation is particularly useful in addressing the fault slip behavior when the stress stability boundary ($\tau_0 = \tau_r$) is approached and where the critical shear crack length has been shown numerically to diverge. In this case $a \gg \ell$ and

$\arcsin(\ell/a) \approx \ell/a$ in (3.18), which allows to evaluate at nucleation

$$\frac{\ell_c}{a_w} \approx \frac{1}{8} \frac{(\tau_p - \tau_r)^2}{\tau_r(\tau_0 - \tau_r)}, \quad \frac{a_c}{a_w} \approx \frac{1}{4\pi} \frac{(\tau_p - \tau_r)^2}{(\tau_0 - \tau_r)^2} \quad (\tau_0 \rightarrow \tau_r) \quad (3.19)$$

The critical shear crack (slipping patch) length a_c asymptote is identical to the expression reported previously [64, 62] and is also relatable to the Andrews' [74] critical crack length for a slip weakening fault under uniform loading. Both the shear and the open (HF) crack lengths diverge as $\tau_0 \rightarrow \tau_r$, (3.19), but the HF length does so slower, as also evidenced in Fig. 3.9a.

3.5 Field Implications

3.5.1 Estimates of slip weakening distance δ_w and nucleation lengthscale

a_w

Using the interpretation of the laboratory rate and state friction law, Uenishi and Rice [73] estimate the slip-weakening rate W to range from 0.15 to 3 (1/mm). They also show that this range is consistent with the interpretation of Rice [100] of the post-failure stage of triaxial experiments on intact granite specimens of Rummel et al. [101]. Considering a typical value of the peak friction coefficient of a sedimentary rock $f_p = 0.6$, the characteristic slip weakening distance $\delta_w = f_p/W \sim 1$ mm (taking average value 0.6/mm of the above W range). Similar values of the slip weakening distance are inferred by Brantut and Viesca [102] for initially healed/cemented fault gouge friction experiments of Karner et al. [103].

The above estimates stem from laboratory scale observations of either (i) sliding between rock blocks separated by very thin (millimeter or less) fault gouge, or (ii) fresh fracture of initially intact rock. In either case, δ_w scale may be relatable to the sliding surfaces' roughness, and is denoted here as a “*thin fault scaling*”.

On the other hand, the observations made on more mature faults in nature suggest

that the slip can be accommodated in a finite fault core (principal slip zone), which is cms to dms in thickness and is comprised of a (weak) ultracataclastic gouge [104]. Direct observations on an apparently stable section of the San Andreas Fault at Parkfield, CA at ~ 3 km depth show pervasive slip within a \sim meter thick ultracataclastic gouge layer at a slow (tectonic) rate [105]. Observations from drilling into fault zones that recently hosted large earthquakes show a \sim cm thick bands within a wider ultracataclastic gouge layer which have been inferred to have accommodated large earthquake slip [106]. In contrast, observations of an exhumed section of a major ancient fault (Punchbowl fault, CA) have been used to infer \sim sub mm thick relict principal slip zones [107].

Since a severe localization is predicted to take place in the course of seismic slip [108], these different field observations of the principal slip zone thickness may be reconciled to correspond to various degrees of slip localization during different slip events. If so, it is plausible to assume that the slip is initially pervasive, i.e. is accommodated over the entire (or significant fraction of) thickness of the ultracataclastic gouge layer, and is then progressively localized with the accumulated slip/strain. Marone and Kilgore [109] have concluded based on laboratory gouge friction experiments, that the corresponding *quasi-static* slip weakening distance δ_w of the nucleation process is proportional to the evolving thickness h of the slipping zone. (Note that a similar conclusion, $\delta_w \propto h_0$, has been drawn theoretically for the *dynamic* fault weakening with slip due to the frictional heating [108], where h_0 is the initial thickness of the slipping gouge).

Based on the above reasoning, and assuming anthropogenic slip nucleation on an ancient (inactive), healed mature fault, we consider a possibility that the slip weakening distance can scale with the thickness of the ultracataclastic gouge layer, i.e. $\delta_w \sim h_0 \sim$ cms to dms. This estimate, further denoted as a “*thick fault scaling*”, may therefore exceed the “*thin fault scaling*” of δ_w by two orders of magnitude.

Taking the plane-strain modulus $E' = 50$ GPa and the ambient effective stress $\sigma_0 - p_0 = 50$ MPa for a typical depth range from 2 to 4 km of hydraulic fracturing industrial applications, the characteristic slipping patch lengthscale (3.10) is $a_w \sim 10^3 \times \delta_w$. This translates to $a_w \sim 1$ m in the “thin fault” and $a_w \sim 10$ to 100 m in the “thick fault” scalings, respectively.

3.5.2 Estimates of hydraulic fracture loading factor λ

The hydraulic fracture dimensionless loading factor λ , (3.12), which quantifies the HF-induced perturbation of the fault effective stress when the HF has grown to the size $\sim a_w$, is estimated below for two representative HF scenarios. Namely, the hydraulic fracturing injection of a slick water with viscosity of $\mu = 5$ cp at the rate $Q = 0.01$ m²/s, and injection of a gelled fluid with viscosity $\mu = 100$ cp at the rate $Q = 0.001$ m²/s, respectively. (The assumed flow rate values represent typical field volumetric injection rates into a fracture with the out-of-the-plane extent, e.g., the height of a laterally propagating HF, of 10 m). For both injection scenarios, the loading factor evaluates to about $\lambda \sim 0.1$ in the “thin fault” scaling ($\delta_w \sim 1$ mm) and to the tenth of that, i.e., $\lambda \sim 0.01$, for the “thick fault” scaling ($\delta_w \sim 1$ cm). As the numerical solutions attest, these values of λ have a little influence over the slip nucleation (see, for example, Figure 3.9 for the nucleation patch size dependence on λ and on the fault understress).

3.5.3 Slipping patch, hydraulic fracture, and injected fluid volume at the nucleation

Our study has established the solution for the slipping patch size a_c at the nucleation of dynamic slip and the corresponding critical hydraulic fracture size ℓ_c as a function of the background shear loading on the fault. These two critical lengths are bounded from below by the critically-stressed fault scaling (3.17) when $\tau_0 \rightarrow \tau_p$ and from

above by the metastable-fault scaling (3.19) when $\tau_0 \rightarrow \tau_r$.

The nucleation slipping patch size a_c serves as a proxy for the minimum extent of a fault capable of hosting seismic slip. For faults more favorably oriented with respect to the background stress, i.e. τ_0 sufficiently exceeds τ_r , a_c scales with the characteristic lengthscale a_w , which is estimated to vary between ~ 1 to ~ 100 meters depending on the fault maturity (“thin” vs. “thick” faults). It is of note, that for less favorably-oriented, metastable faults, $\tau_0 \rightarrow \tau_r$, the minimum fault extent to support seismic slip “blows up” as $1/(\tau_0 - \tau_r)^2$.

Assuming an extensive enough fault capable of hosting seismic slip, $\tau_0 > \tau_r$, the nucleation would then be solely determined by the size of the stimulated hydraulic fracture in comparison to the critical size ℓ_c . The latter scales with the characteristic lengthscale a_w for the background stress values intermediate to the peak and residual strength, however, it is seen to vanish as $(\tau_p - \tau_0)$ for the critically-stressed faults ($\tau_0 \rightarrow \tau_p$) and “blow-up” as $1/(\tau_0 - \tau_r)$ for the metastable faults ($\tau_0 \rightarrow \tau_r$). Given that a typical HF length ℓ in oil/gas reservoir stimulation ranges from 10s to 100s meters, the dynamic slip will most likely be always nucleated by hydraulic fracturing on favorably-oriented (critically-stressed) faults, while the fault maturity (the length-scale a_w) is expected to play a deciding role for nucleation on less favorably-oriented and metastable faults. For example, considering a metastable fault with $\tau_0 = 1.05 \tau_r$ and $\tau_r/\tau_p = 0.6$, we estimate from (3.19) $\ell_c \approx 1.1 a_w$, which would then suggest dynamic slip nucleation by a typical HF treatment on a “thin” fault with $a_w \sim 1$ m, but not necessarily on a “thick” fault with $a_w \sim 10$ to 100 meters.

The above discussion of the seismic slip nucleation by a HF of a given length $\ell(t)$ can be rephrased in terms of the injected fluid volume (per unit fracture height) $V_{inj} = Q_0 t$, by means of relating the two via (3.6-3.7) as follows

$$V_{inj} = \gamma^{-3/2} \left(\frac{\mu' Q_0}{E'} \right)^{1/4} \ell^{3/2}, \quad \gamma^{-3/2} \approx 2.073 \quad (3.20)$$

For the two HF treatments’ scenarios considered in Section 6.2, we can estimate $V_{inj} \sim (10^{-3} \text{ m}^{1/2}) \times \ell^{3/2}$. Then for a metastable fault with $\ell_c \approx 1.1 a_w$, the critical injected fluid volume required to nucleate seismic slip is $V_{inj,c} \sim 10^{-3} \text{ m}^3/\text{m}$ (i.e., per meter of the HF height) on a “thin” fault and $V_{inj,c} \sim 1 \text{ m}^3/\text{m}$ on a “thick” fault.

When applying these results to natural faults, one has to reconcile the model’s assumption of a homogeneous stress and strength on a planar fault with generally heterogeneous fields inferred from inversions of seismological data, which show spatio-temporal complexity of slip in large earthquakes [110, 111], and from wellbore logging of the orientation of breakouts and drilling-induced fractures [112, 113]. We can draw some inferences as to how the results of a homogeneous stress/strength model may translate to the heterogeneous fault conditions from existing numerical studies of dynamic rupture and seismicity on faults with fractal stress [114, 115, 58]. Specifically, Ripperger et al. [115] rupture solutions show that the heterogeneous fault stress tends to broaden the rupture nucleation patch size a_c compared to that in the baseline case, $a_c^{(uni)} \approx 0.579 a_w$, corresponding to the uniform fault stress. This patch broadening, however, still retains a relation to the uniform stress scaling, as an equivalent radius a_c of the irregular-shaped (2D) nucleation patch (taken here as geometric mean of the inscribed and circumscribed circles’ radii reported by Ripperger et al. [115] in their Figure 5) is roughly between $1.5 a_c^{(uni)}$ to $2 a_c^{(uni)}$ depending on the value of the Hurst exponent of the stress distribution. Consistent with the baseline, uniform stress case, the dynamic rupture nucleation in their study requires the ultimately unstable fault conditions, $\tau_0 > \tau_r$, with τ_0 now bearing the meaning of the mean background stress, while the post-nucleation rupture fate (the run-away, fault-spanning rupture mode vs. the arrested rupture) is less trivial and depends on the degree of the stochastic fault stress variability.

3.6 Conclusions

The goal of this chapter was to study initiation of a dynamic rupture on a fault due to a hydraulic fracturing injection into it. This can also serve as a simplified model for a case where the hydraulic fracture has intersected a fault and diverted into it. The slip patch grows as a result of the reduction of the fault strength to zero along the hydraulic fracture, the open part of the fault, as well as the decrease of the fault frictional strength due to the normal stress perturbation ahead of the hydraulic fracture tip. Slip-weakening nature of the fault friction may cause the slipping patch to propagate dynamically leading to seismic slip.

Ultimate stability of the fault depends on its background shear loading τ_0 and its ambient residual strength τ_r . Injection into a fault with $\tau_0 > \tau_r$ will result in a dynamic shear rupture (earthquake). Nucleation takes place when the extent of the slipping patch reaches the critical length $\sim a_w$. This scaling changes when τ_0 approaches τ_r (a metastable fault), in which case both critical hydraulic fracture and slipping patch lengths increase strongly with diminishing τ_0 as foreshadowed in the earlier study of non-hydrofracture fluid injection into a fault [64]. Nucleation of dynamic slip is only weakly dependent on the magnitude of the normal stress perturbation ahead of the propagating hydraulic fracture (quantified by the loading factor λ , Eq. (3.12)), and is mainly controlled by the hydraulic fracture length (i.e., the size of the fully unloaded fault segment at a given time). The developed solution for the critical HF length at the nucleation, allows to relate the parameters of industrial hydraulic fracture treatments (e.g., fluid injection volumes) and fault properties (e.g., the slip weakening distance) to the likelihood of induced seismic slip. For the faults which are stressed below their ambient value of the residual strength, i.e. $\tau_0 \leq \tau_r$, the hydrofracture induced slip develops aseismically. This is in contrast to a non-hydrofracture injection, where, under the same background stress loading

conditions ($\tau_0 \leq \tau_r$), the fault slip can undergo a seismic transient.

CHAPTER 4: NUCLEATION OF SLIP ON A NATURAL FRACTURE DUE TO INTERACTIONS WITH A PROPAGATING HYDRAULIC FRACTURE

4.1 Introduction

In this chapter, we investigate possibility of a microseismic slip on a natural fracture as a result of poromechanical interactions with an advancing hydraulic fracture. As the hydraulic fracture approaches slip initiates along the favorably oriented natural fracture.

Presence of natural fractures is the key to enhance conductivity of unconventional reservoirs by the process of hydraulic fracturing. These pre-existing fractures often provide pathways for the flow of fluids in the low permeability reservoirs. Microseismic events caused by shear failure occur along these planes of weakness in the rock surrounding the main hydraulic fracture. The fractures vary in length (on a scale of $\sim 1 - 10$ meters) and are often confined in the targeted reservoir layers (between impermeable layers of rock) in which the hydraulic fracture treatment is being conducted.

Stress perturbations in the vicinity of a propagating hydraulic fracture activate slip events along the critical fractures. The stress fields in the surrounding rock is dominated by the related large pressure gradient at the tip of hydraulic fracture where the effects of rock toughness, fracturing fluid's viscosity and etc. are localized. Rubin [47] considered the stress perturbations around the tip of a propagating dike to be of the order of the suction in the (several meter) dike's tip cavity. In this chapter we formulate the propagating hydraulic fracture with a near tip solution that also accounts for the presence of a lag between the fracturing fluid's front and the hydraulic fracture's tip.

One of simplifying assumption of this work is one-way interaction between the hydraulic fracture and the shear fracture. In other words, we have assumed that the stress perturbation due to slip on the natural fracture has no effect on the hydraulic fracture propagation. This assumption is particularly applicable when the length of the hydraulic fracture (~ 100 meters) is much larger than the slipped patch.

Nucleation of slip on a frictional fracture approached by a hydraulic fracture depends on the state of in-situ stresses, the hydraulic fracture pressure, angle of approach and friction of the fracture among others. The dynamic propagation of a favorably oriented fracture will arrest at the end points of the fracture and the induced “microseismic” event corresponds to the limited-area of the fracture surface.

4.2 Model

Consider a two dimensional shear fracture inclined at an angle β to the hydraulic fracture plane. The semi-infinite hydraulic fracture, loaded internally by fluid pressure p , is propagating at a constant velocity V in an impermeable linear elastic medium characterized by plane-strain modulus E' . The hydraulic fracture has a lag of constant length ℓ_{tip} , tip pressure p_{tip} and is propagating in the plane aligned with far-field maximum stress σ_{max} (x axis) and perpendicular to the minimum stress σ_{min} . We define L_{max} as the distance from the intersection point between the planes of the natural and hydraulic fractures, respectively, to the hydraulic fracture tip at the moment when the natural fracture slips for the first time. The pre-existing shear fracture has a limited extent (i.e., $\pm\hat{C}$), an initially zero shear displacement and it coincides with the transformed coordinate system $(\hat{x}, 0)$ (Figure 4.1).

Slip initiates along the favorably oriented shear fracture when the peak shear strength $\tau_p = f_p(\sigma_n - p)$ declines below the shear stress τ . The slip patch of length $2a = a_+ - a_-$ grows quasi-statically with the hydraulic fracture approaching closer to the shear fracture. Slip either turns into the dynamic slip due to the slip weakening nature of

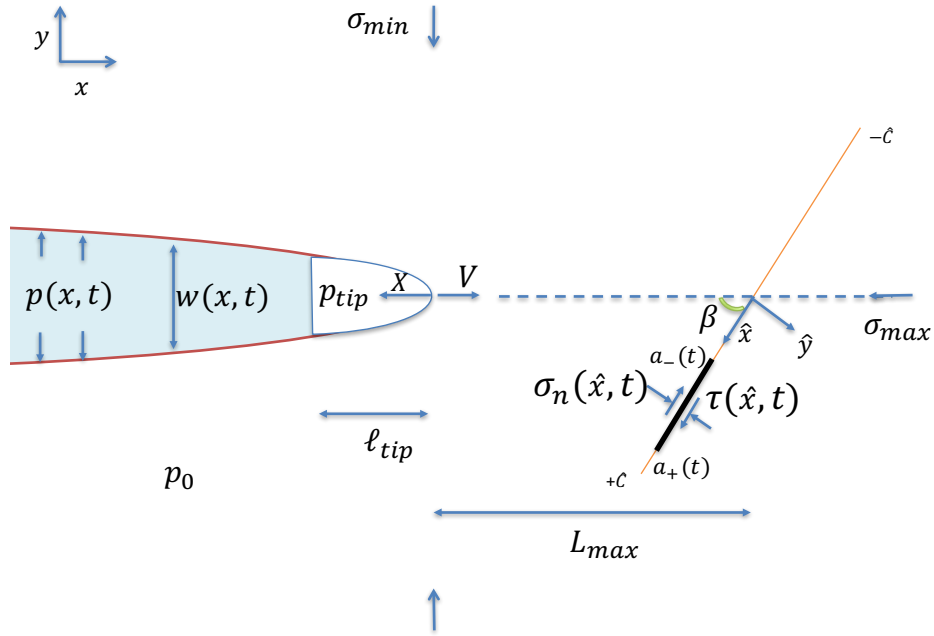


Figure 4.1: A semi-infinite hydraulic fracture approaches a pre-existing shear fracture. Stress perturbation ahead of the hydraulic fracture activates slip along the shear fracture.

friction, or expansion of the slipping patch stops before the intersection. The dynamic rupture will arrest at the end points of the fracture where the induced microseismicity relates to the finite length of the natural fracture.

4.3 Propagating semi-infinite hydraulic fracture

When the fracturing fluid flows to the hydraulic fracture tip, the non linear hydromechanical coupling between fluid and solid in the vicinity of the advancing fracture tip results in a negative singular fluid pressure there: $p_f \sim \ln X$ in the finite fracture toughness case and $p_f \sim -X^{-1/3}$ in the zero toughness case [41, 40]. Since the fracturing fluid could not sustain negative infinite pressure (suction), presence of a lag is necessary to remove this singularity. The lag can have a similar role to the “process zone” in the classical fracture mechanics and allows for the finiteness of the fluid pressure behind the fracture tip and stresses ahead of it.

As the fluid flow is lagging behind the advancing fracture tip, the tip cavity is assumed to be filled with vapors of the fracturing fluid for a nearly impermeable host solid in an undrained propagation (or a fast growing hydraulic fracture). In the general cases of a permeable host rock and/or a drain propagation (slow propagation), the lag can be filled with infiltrating pore fluids from the host rock [47, 48].

Continuity of undrained pore pressure profile requires the pore pressure along the cavity wall to be equal to the pressure within the tip cavity [47]. Along the hydraulic fracture plane $\Delta\sigma_{xx} = \Delta\sigma_{yy}$ (i.e., note the equation (A.32) on $y = 0$) and (2.18) can be rewritten as $\Delta P_{\text{und}} = B(1 + \nu_u)(2\Delta\sigma_{yy})/3$. On the other hand, the uniform pore pressure along the cavity wall $p_0 + \Delta p_{\text{und}}$ must to be equal to cavity pressure p_{tip} . Along the cavity $\Delta\sigma_{yy} = p_{\text{tip}} - \sigma_{\text{min}}$ and the continuity between the cavity pressure and the adjacent pore pressure results in:

$$\frac{p_{\text{tip}}}{\sigma_{\text{min}}} = \frac{(p_0/\sigma_{\text{min}}) - B'}{1 - B'} \quad (4.1)$$

where $B' = \frac{2}{3}B(1 + \nu_u)$. At given ambient pore pressure p_0 , and the known Skemp-ton's and undrained Poisson's ratios, the above equation gives the tip cavity pressure p_{tip} . Note that this equation yields negative cavity pressure $p_{\text{tip}} < 0$ for low enough ambient pore pressure. In this case fluid cavitation is expected in the tip cavity, rendering $p_{\text{tip}} \simeq 0$.

4.3.1 Viscosity dominated, negligible leak-off hydraulic fracture solution

The set of governing equations (2.9-2.12) defines the solution for the opening $w(x, t)$, net fluid pressure $p - \sigma_{\text{min}}$ and constant length of the lag ℓ_{tip} as functions of the tip velocity V , the fluid viscosity μ , the plane strain modulus E' , the minimum in situ stress σ_{min} and the tip pressure p_{tip} .

The self-similar solution of viscosity dominated regime (i.e., negligible toughness) along the normalized moving coordinate $\xi = X/L_\mu$ is obtained by Garagash and

Detournay [46] using following scaling:

$$\ell_{tip} = L_\mu \Lambda, \quad w(X) = \varepsilon L_\mu \Omega(\xi), \quad p(X) - \sigma_{min} = (\sigma_{min} - p_{tip}) \Pi(\xi) \quad (4.2)$$

where Λ denotes the dimensionless fluid lag and

$$L_\mu = \frac{12\mu V E'^2}{(\sigma_{min} - p_{tip})^3}, \quad \varepsilon = \frac{\sigma_{min} - p_{tip}}{E'}. \quad (4.3)$$

are the viscosity dominated length scale and small non-dimensional parameter, respectively.

The solution asymptotically approaches the zero toughness singular solution of the semi-infinite hydraulic fracture at infinity [41]. At the near tip region, the solution is consistent with the linear elastic fracture mechanics solution (2.12). However, the linear elastic fracture mechanics region lies entirely in the lag (with the scaled length $\Lambda = 0.357$) for the negligible rock toughness, $K_{Ic} = 0$. The hydraulic fracture growth in real field operations is expected to obey the viscosity-dominated regime, but at the early stages of propagation in which the fracture extension is toughness dominated [116].

4.3.2 Stress distribution around propagating hydraulic fracture

Having determined the normalized opening Ω as a function of the moving coordinate ξ , the stress distribution around the propagating hydraulic fracture can be expressed by (2.9):

$$\sigma_{XX}(\xi, \eta) = \sigma_{max} + \Delta\sigma_{XX}(\xi, \eta) = \sigma_{max} + \frac{\sigma_{min} - p_{tip}}{4\pi} \int_0^\infty \frac{d\Omega}{ds} G_{\eta\xi\xi}(\xi, \eta, s) ds$$

$$\sigma_{YY}(\xi, \eta) = \sigma_{min} + \Delta\sigma_{YY}(\xi, \eta) = \sigma_{min} + \frac{\sigma_{min} - p_{tip}}{4\pi} \int_0^\infty \frac{d\Omega}{ds} G_{\eta\eta\eta}(\xi, \eta, s) ds \quad (4.4)$$

$$\sigma_{XY}(\xi, \eta) = \frac{\sigma_{min} - p_{tip}}{4\pi} \int_0^\infty \frac{d\Omega}{ds} G_{\eta\xi\eta}(\xi, \eta, s) ds$$

where the influence functions G_{ijk} are provided in Appendix D for dimensionless coordinates $\xi = X/L_\mu, \eta = Y/L_\mu$. Note that stress fields are determined by superposition of background stresses (i.e., $\sigma_{min}, \sigma_{max}$) and the induced stresses due to opening.

4.4 Slip activation region

Slip (or failure) along the pre-existing natural fracture (with no cohesive strength) is governed by the Coulomb failure criterion: $\tau = \tan[\phi_p](\sigma_n - p)$, where τ is the shear stress, σ_n is the normal stress and ϕ_p is the peak friction angle. Background normal $\sigma_n^b(\hat{x}, t)$ and shear $\tau^b(\hat{x}, t)$ stresses along the shear fracture (i.e., predetermined plane, which may or may not be most-favorably oriented) inclined at an angle β from the X direction can be expressed using Mohr transformation:

$$\begin{aligned} \sigma_n^b &= \sigma_{XX} \sin^2 \beta + \sigma_{YY} \cos^2 \beta - \sigma_{XY} \sin 2\beta \\ \tau^b &= (\sigma_{YY} - \sigma_{XX}) \sin \beta \cos \beta + \sigma_{XY} \cos 2\beta \end{aligned} \quad (4.5)$$

The necessary condition for the slip within the perturbed volume of rock is that for slip on the most favorably oriented fracture(s) oriented at $45 + \phi_p/2$ and $45 - \phi_p/2$ from the maximum principal stress direction. This condition is referred to as the Mohr-Coloumb failure criterion, and can be formulated as:

$$\sqrt{(\sigma_{XX} - \sigma_{YY})^2 / 4 + \sigma_{XY}^2} > ((\sigma_{XX} - p) + (\sigma_{YY} - p)) \sin[\phi_p] / 2 \quad (4.6)$$

The latter condition is helpful in evaluating the region adjacent to the hydraulic

fracture tip where slip may be activated [117].

4.4.1 Transformation of coordinates

Introducing the change of variables ($X = \hat{x} \cos \beta - L_{max} + Vt$, $Y = \hat{x} \sin \beta$) transforms the moving coordinate system (X, Y) into the fixed coordinate system $(\hat{x}, 0)$ which coincides with the pre-existing natural fracture located at the distance L_{max} ahead of the hydraulic fracture tip.

4.5 Slip along the natural fracture

Shear stress along the natural fracture is given by the elasticity equation (2.13)

$$\tau(\hat{x}, t) = \tau^b(\hat{x}, t) - \frac{E'}{4\pi} \int_{a_-}^{a_+} \frac{d\delta(s, t)}{ds} \frac{ds}{\hat{x} - s} \quad (4.7)$$

where τ^b is the stress induced in the material by the hydraulic fracture in absence of the shear crack and the second term is the stress change due to slip. Shear strength along the slipped portion of the fracture is given by $\tau = f(\sigma_n - p)$. The local normal stress is equal to background normal stress $\sigma_n = \sigma_n^b$ (as slip does not change the local normal stress along the natural fracture in an infinite medium).

4.5.1 Scaling and numerical approach

To simplify the numerical solution, the system of equations (4.5-4.7) are expressed in terms of the normalized coordinate $\hat{\xi} = (\hat{x} - b)/a$, where $a(t) = (a_+ - a_-)/2$ is the crack half-length and $b(t) = (a_+ + a_-)/2$ is the midpoint of the slipping patch. After doing so, the normalized shear crack half-length a/a_w , normalized slipping patch midpoint b/a_w and normalized slip δ/δ_w (i.e., the problem unknowns) can be expressed as functions of normalized time Vt/L_μ , normalized residual friction f_r/f_p , non-dimensional peak friction f_p and the length parameter $\varsigma = L_\mu/a_w$ (i.e., the

problem knowns) for an inclination β , normalized pore pressure p_0/σ_{min} and in-situ stress ratio of $\sigma_{max}/\sigma_{min}$. The characteristic (shear) crack length is given by:

$$a_w = \frac{E'}{\sigma_{min} - p_{tip}} \delta_w \quad (4.8)$$

where the characteristic slip weakening distance has been defined in (2.17). The normalized slip formulation and the method of solution are provided in Appendix E.

4.5.2 Some field parameters estimates

Consider the following example of plausible values (ranges) for rock and fracturing fluid material used in the fracturing application. Assume the treatment is performed in an elastic rock medium with the elastic modulus $E = 30$ GPa, Skempton coefficient $B = 0.5$ [85] and Poisson ratios $\nu = 0.25$, $\nu_u = 0.3$ [85, 118].

Range of stress magnitudes for a strike slip vertical fracture $\sigma_{min} < \sigma_v < \sigma_{max}$ vary in different tectonic environments.

Table 4.1 summarizes some examples of in-situ principal stress measurements at a lithostatic depth of 3 km for the strike slip state tectonic regime. The lithostatic stress refers to the weight of the rock above a specified depth (while the confining stress is combination of the lithostatic stress and the hydrostatic stress, i.e. total weight of the rock and the water). In the off-shore reservoir examples, the stress measurements are provided at the depth of 3 km of the rock below the sea floor. The water depth (above the sea floor) for the off-shore reservoirs of Timor Sea (1) and Timor sea (2) are ~ 600 m and ~ 400 m, and ~ 500 m for the Visund field, respectively.

Table 4.1: Stress measurements for the strike slip state tectonic regimes at a lithostatic depth of 3 km.

Well Location	σ_{min} (MPa)	σ_{max} (MPa)	p_0 (MPa)	σ_v (MPa)	$\frac{(\sigma_{max}-p_0)}{(\sigma_{min}-p_0)}$	$\frac{p_0}{\sigma_{min}}$	Ref.
KTB pilot borehole	49	96	30	87	3.47	0.61	[119]
Timor Sea (1)	52	84	36	77	3	0.69	[120]
Timor Sea (2)	52	81	34	72	2.61	0.65	[120]
A field in South East Asia	43	68	30	68	2.92	0.7	[121]
Visund field in North Sea	65	89	50	72	2.6	0.77	[122]
Central Australia	69	156	30	69	3.23	0.43	[123]

Stress measurements in the KTB pilot borehole and also in some portions of the Timor Sea (both examples) indicate strike slip fracture/faulting stress state (in which the vertical stress is the intermediate stress). In the example of the southeast Asia field, σ_{min} is less than the vertical stress but $\sigma_{max} \approx \sigma_v$ which characterizes a normal/strike slip stress state. In the Visund field in the northern North Sea (and the example of the well in central Australia) represent(s) a more compressional strike slip stress state where the magnitude of minimum horizontal stress σ_{min} is slightly below (or equal to) the magnitude of σ_v which is almost a strike-slip/reverse stress state [123]. The pressure profile for all the examples in Table 4.1 are hydrostatic except the Visund field in which overpressure (i.e., abnormally high pressure) has been developed.

Considering a typical peak friction coefficient $f_p = \tan[\phi_p] = 0.8$ [124] sets an upper bound on the effective principal stress ratio $(\sigma_{max} - p_0)/(\sigma_{min} - p_0) = 4.33$ for the stable rock under principal in-situ stresses (when the hydraulic fracture is not present). The directions of critical potential failure planes are at the angles $\pm(45 - \phi_p/2) = \pm 24^\circ$ to the maximum compressive principal stress. The magnitude of the effective principle stress ratio cannot be larger than this value because a well oriented fracture would slip. The lower bound value of the effective maximum horizontal

stress is the effective vertical stress. Figure 4.2 illustrates the limiting failure values for the effective horizontal stress ratio $(\sigma_{max} - p_0)/(\sigma_{min} - p_0)$ as the Coulomb failure criterion is expressed on the planes that are oriented at an angle β to the direction of maximum horizontal stress: $f_p ((\sigma_{max} - p_0) \sin^2[\beta] + (\sigma_{min} - p_0) \cos^2[\beta]) < (\sigma_{max} - \sigma_{min}) \sin[\beta] \cos[\beta]$.

For similar applications at lithostatic depth of 3 km, we perform the first numerical analysis assuming the minimum horizontal stress $\sigma_{min} = 45$ MPa and the maximum horizontal stress $\sigma_{max} = 81$ MPa when the pore pressure is hydrostatic $p_0 = 30$ MPa. The lithostatic overburden stress for the rock with average density $\rho = 2600$ m³/kg is $\sigma_v = \rho gh = 78$ MPa. This corresponds to the effective horizontal stress ratio $(\sigma_{max} - p_0)/(\sigma_{min} - p_0) = 3.4$ in Figure 4.2, which in terms of numerical parameters expresses the absolute stress ratio $\sigma_{max}/\sigma_{min} = 1.8$ and normalized pore pressure $p_0/\sigma_{min} = 0.66$. The second analysis is performed for the in-situ stress measurements in the Visund field example which corresponds to the effective horizontal stress ratio $(\sigma_{max} - p_0)/(\sigma_{min} - p_0) = 2.6$, $\sigma_{max}/\sigma_{min} = 1.37$ and $p_0/\sigma_{min} = 0.77$ (Table 4.1).

The hydraulic fracture is assumed to propagate with average velocity $V = 1$ m/s during the two assumed scenarios of conventional hydraulic fracturing with the gelled fluid viscosity $\mu = 0.1$ Pa.s and slick water fracturing with $\mu = 0.005$ Pa.s, respectively.

A typical value of slip-weakening slope $W = 0.8/\text{mm}$ yields the slip-weakening displacement $\delta_w = 1$ mm (3.10).

Taking into account all the assumptions, Table 4.2 summarizes the values of the assumed parameters for the numerical analyses.

Given the minimum horizontal stress and pore pressure, equation (4.1) is used to calculate the lag pressure p_{tip} . The non dimensional length parameter ς and $\varsigma_{s.w.}$ represent the conventional and slick water operations, respectively. The result are presented for the conventional hydraulic fracturing, unless stated otherwise.

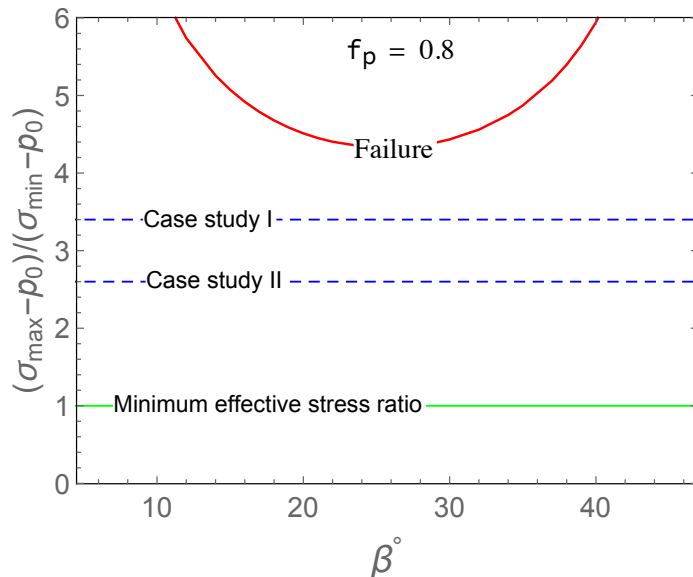


Figure 4.2: The limiting failure values of the effective principal stress ratio for the planes that are oriented at an angle θ to the direction of maximum horizontal stress assuming a typical peak friction coefficient $f_p = 0.8$. The blue dashed lines correspond to the assumed effective principal stress ratios in the numerical analyses.

Table 4.2: The assumed parameter values for the numerical analyses. The values represent as an examples of stress and pore pressure measurements at 3 km lithostatic depth. Conventional and slick water hydraulic fracturing are distinguished with the viscosity dominated length scale $L_\mu^{(Gel)}$ and $L_\mu^{(Slick\ water)}$, respectively.

	σ_{min} (MPa)	σ_{max} (MPa)	p_0 (MPa)	$\sigma_{max}/\sigma_{min}$	p_0/σ_{min}	p_t/σ_{min}	$L_\mu^{(Gel)}$ m	$L_\mu^{(Slick\ water)}$ m	a_w m
Case I	45	81	30	1.8	0.66	0.41	0.066	0.003	0.96
Case II	65	89	50	1.37	0.77	0.59	0.068	0.003	0.96

4.6 Flow in a mechanically closed natural fracture

Rough surfaces of a mechanically closed natural fracture (subjected to a negative net effective stress) prevent complete closure of the fracture and create hydraulic conductivity in excess of that of the rock matrix. The hydraulic conductivity (before any slip) is often negligible for natural fractures that are partially mineralized.

The flow of fluid inside a mechanically closed natural fracture can be described by

the lubrication equation via substituting the flow equation (2.2) into the continuity equation (2.3):

$$\frac{\partial \bar{w}}{\partial t} = \frac{\partial}{\partial \hat{x}} \left(\frac{\bar{w}^3}{12\mu_f} \frac{\partial p}{\partial \hat{x}} \right). \quad (4.9)$$

where \bar{w} is the hydraulic opening and μ_f is the formation fluid viscosity.

Several authors have investigated the relation between the deformation of mechanically closed fracture with the change in the fracture net loading [125, 126, 127]. In this study, we have adapted a relation by Bandis et al. [127] in which the change of the hydraulic opening in $\bar{w} = \bar{w}_0 + \Delta\bar{w}$ is given by

$$\Delta\bar{w} = \frac{\bar{w}_0(p - \sigma_n)}{p^* - (p - \sigma_n)} \quad (4.10)$$

where \bar{w}_0 is the fracture neutral opening and the fracture characteristic pressure p^* relates to the initial normal stiffness k_{ni} by $p^* = k_{ni}\bar{w}_0$. If we insert the above equation into (4.9) will result in

$$\frac{\partial p}{\partial t} - \frac{\partial \sigma_n}{\partial t} = \frac{p^*}{12\mu_f \bar{w}_0} \left(\frac{\bar{w}_0^3}{1 - \frac{p - \sigma_n}{p^*}} \frac{\partial^2 p}{\partial \hat{x}^2} - \frac{3\bar{w}_0^3}{p^* \left(1 - \frac{p - \sigma_n}{p^*}\right)^2} \frac{\partial p}{\partial \hat{x}} \left(\frac{\partial p}{\partial \hat{x}} - \frac{\partial \sigma_n}{\partial \hat{x}} \right) \right) \quad (4.11)$$

To simplify the numerical analysis, the normalized pressure Π , normal stress Σ_n , time Θ are defined along the normalized coordinate $\hat{\xi} = \hat{x}/a_w$ where

$$\Pi = \frac{p}{\sigma_{min} - p_{tip}}, \quad \Sigma_n = \frac{\sigma_n}{\sigma_{min} - p_{tip}}, \quad \Theta = \frac{Vt}{L_\mu}. \quad (4.12)$$

The normalized form of (4.11) thus takes the form of

$$\frac{\partial \Pi}{\partial \Theta} - \frac{\partial \Sigma_n}{\partial \Theta} = \alpha \left(\frac{1}{1 - \frac{\Pi - \Sigma_n}{\Gamma}} \frac{\partial^2 \Pi}{\partial \hat{\xi}^2} - \frac{3}{\Gamma \left(1 - \frac{\Pi - \Sigma_n}{\Gamma}\right)^2} \frac{\partial \Pi}{\partial \hat{\xi}} \left(\frac{\partial \Pi}{\partial \hat{\xi}} - \frac{\partial \Sigma_n}{\partial \hat{\xi}} \right) \right) \quad (4.13)$$

where fracture dimensionless diffusivity coefficient and stiffness ratio are defined as

$$\alpha = \frac{p^* \bar{w}_0^2 L_\mu}{12\mu_f V a_w^2}, \quad \Gamma = \frac{p^*}{\sigma_{min} - p_{tip}}. \quad (4.14)$$

4.6.1 Undrained pore pressure along the natural fracture

Equation (4.11) considers the flow of fluid along the natural fracture. However, undrained pore pressure difference within the natural fracture $p_0 + \Delta\sigma_n$ and outside porous medium $p_0 + \Delta p_{und}$ causes a transverse flow. Simple analogy is implemented to compare the rate of pore pressure exchange with the semi-impermeable medium with regard to the diffusion along the fracture (Figure 4.3).

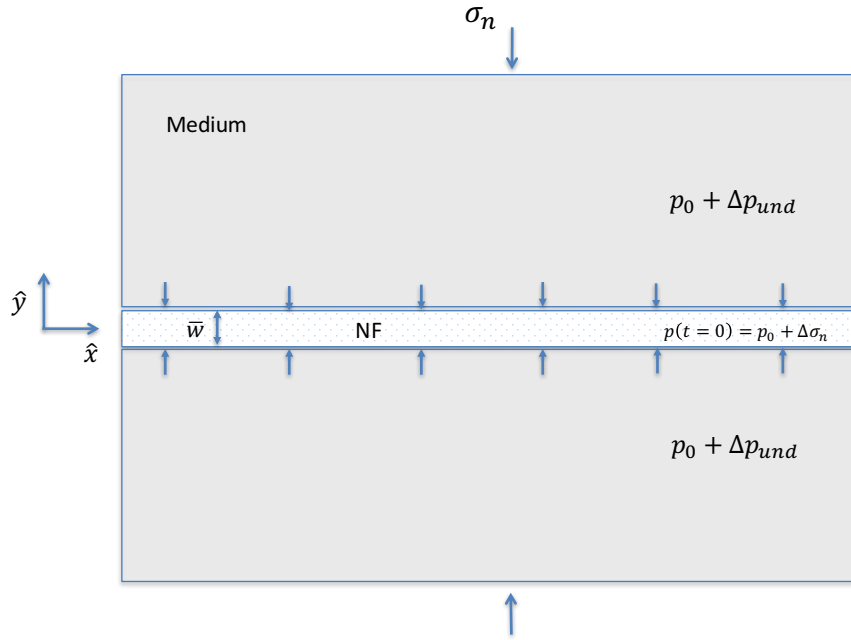


Figure 4.3: The problem set up to approximate pore pressure along the natural fracture

Consider flow of the fluid into the medium in the \hat{y} direction. For the partially mineralized natural fracture and within the time frame of an undrained response, pore pressure distribution in the medium is calculated by solving diffusivity equation:

$$\frac{\partial p}{\partial t} = \frac{k}{\mu_f S} \left(\frac{\partial^2 p}{\partial \hat{y}^2} \right) \quad (4.15)$$

where k is the medium permeability, and the medium storage $S = \phi c_t$ is expressed in terms of porosity ϕ and bulk compressibility c_t , respectively. The storage coefficient S is defined as the volume of fluid stored into or extracted (per unit volume of rock) as a result of a unit increase or decrease of pore pressure, measured under the condition of constant volumetric strain.

The rate of fracture opening (corresponds to volume change) at the wall (i.e., at the boundary $\hat{y} = 0$) is balanced by fluid exchange with medium:

$$\hat{y} = 0^\pm : \quad \frac{1}{2} \frac{\partial \bar{w}}{\partial t} = \pm \frac{k}{\mu_f} \frac{\partial p}{\partial \hat{y}} \quad (4.16)$$

The analogy considers the time scale when pressure inside the fracture is equilibrated with the medium pressure.

When stress changes from propagating hydraulic fracture are imposed on the natural fracture possessing different properties than the medium, the initial pressure is $p_0 + \Delta\sigma_n$ at the fracture wall and the medium undrained pressure $p_0 + \Delta p_{und}$ everywhere else, $\hat{y} > 0$. Using scaling for pressure and time defined in (4.12) along the non dimensional coordinate $\hat{\eta} = \hat{y}/a_w$ gives

$$\frac{\partial \Pi}{\partial \Theta} = \alpha_m \frac{\partial^2 \Pi}{\partial \hat{\eta}^2} \quad (4.17)$$

where $\alpha_m = kL_\mu/(\mu_f S V a_w^2)$ is the medium dimensionless diffusivity coefficient. Non dimensional form of (4.16) and the initial condition are given by

$$\frac{\partial \Pi}{\partial \Theta} = \varrho \frac{\partial \Pi}{\partial \hat{\eta}} \left(1 - \frac{\Pi - \Sigma_n}{\Gamma} \right)^2 \Big|_{\hat{\eta}=0^\pm}, \quad \Pi(\Theta = 0) = \frac{p_0 + \Delta\sigma_n}{\sigma_{min} - p_{tip}}, \quad \Pi(\hat{\eta} > 0) = \frac{p_0 + \Delta p_{und}}{\sigma_{min} - p_{tip}} \quad (4.18)$$

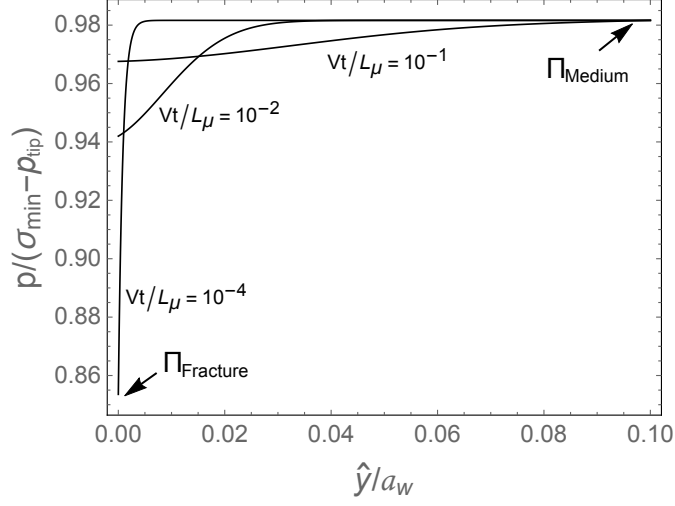


Figure 4.4: Medium pore fluid diffusion into the fracture at the arbitrary location chosen by the normalized distance $L_{max}/L_{\mu} = 10$. Pore fluid flows to equilibrate the pressure difference between the normalized medium pressure $(p_0 + \Delta p_{und})/(\sigma_{min} - p_t) = 0.98$ and the inside fracture pressure $(p_0 + \Delta \sigma_n)/(\sigma_{min} - p_t) = 0.82$ for conventional hydraulic fracturing scenario.

where $\varrho = 2p^* L_{\mu} k / (\bar{w}_0 \mu_f V a_w)$.

Typical representative values of neutral opening and initial stiffness for a fresh to slightly weathered fracture undergoing unloading process (with similar behavior in loading process with high values of confining stress) in sandstone are $\bar{w}_0 = 0.17$ mm and $k_{ni} = 12.8$ MPa/mm, respectively [127]. Using typical values of formation permeability $k = 10$ md, storage coefficient $S = 10^{-10}$ Pa $^{-1}$ (characterized for a typical sand stone with porosity $\phi = 0.1$ and and bulk compressibility $c_t = 10^{-9}$ Pa $^{-1}$) and formation fluid viscosity $\mu_f = 0.001$ Pa.s yields the non-dimensional medium diffusivity coefficient $\alpha_m = 0.007$ and $\varrho = 0.017$ for the conventional fracturing scenario. The fracture non-dimensional diffusivity coefficient and stiffness ratio are calculated as $\alpha = 0.37$ and $\Gamma = 0.08$, respectively. Figure 4.4 shows pressure build up with time inside the fracture at the arbitrary distance from the HF tip chosen by the normalized distance $L_{max}/L_{\mu} = 10$. Formation fluid flows to equilibrate the pressure difference between the larger medium pressure $p_0 + \Delta p_{und}$ and the inside fracture pressure $p_0 + \Delta \sigma_n$.

Pore pressure within the fracture is equilibrated with the medium pore pressure $p_0 + \Delta p_{und}$ (with relative error $e \leq 0.01$) in the time scales two order of magnitudes smaller than the crossing time $Vt/L_\mu = 10$. Thus, the fluid pressure inside the fracture is approximately given by the medium pressure (as a result of the fluid exchange between the natural fracture and the medium).

Assuming that pressure along the fracture is given by the medium undrained pore pressure $p_0 + \Delta p_{und}$ allows us to determine L_{max} (as a function of the effective stress measurements) for the most favorable-to-slip fracture ($\beta = 24^\circ$) that results in $L_{max}/L_\mu = 119.5$ for the first and $L_{max}/L_\mu = 25$ for the second case studies, respectively. Note that the dimensional size $L_{max} \sim 1 - 10$ m validates the use of the tip asymptote solution for the hydraulic fracture with length $\ell \sim 100$ m.

In addition, we can approximate the timescale for pore pressure diffusion in the medium over the characteristic distance L_{max} by solving the diffusivity equation (4.17). The 1-D solution under the assumptions of constant over pressure Δp introduced at a given location $\hat{y} = 0$, initial condition $p = p_0$ and also the ambient pore pressure at infinity, is given by the normalized form of $p - p_0 = \Delta p \operatorname{Erfc}(\hat{y}/\sqrt{(k/\mu_f S)t})$. The result shows that this timescale is five orders of magnitude (with relative error $e \leq 0.1$) larger than the HF crossing time $Vt/L_\mu = 119.5$ (i.e., the time for the HF to propagate the same distance L_{max}). This justifies the assumption of the undrained pore pressure around the HF front.

4.7 Results

Slip occurs on pre-existing shear fracture as the fracture peak shear strength $\tau_p = f_p(\sigma_n^b - (p_0 + \Delta p_{und}))$ declines below the background shear stress τ^b acting along the fracture. It also may activate while τ^b increases above τ_p as the background stresses along the pre-existing fracture evolve when the HF approaches the latter.

Figure 4.5 illustrates the stress perturbation $\Delta\sigma_{YY}$ (a), $\Delta\sigma_{XX}$ (b), $\Delta\sigma_{XY}$ (c) around

the hydraulic fracture. The negative values for the stress perturbations indicate the tensile stress perturbation. As it can be seen the tensile stress perturbations are nowhere greater than the along (“or around”) the tip cavity and deteriorate as the distance from the hydraulic fracture increases. Note that the stress distribution $\sigma_{XX} = \sigma_{max} + \Delta\sigma_{XX}$, $\sigma_{YY} = \sigma_{min} + \Delta\sigma_{YY}$, $\sigma_{XY} = \Delta\sigma_{XY}$ around the hydraulic fracture is determined by superimposing far-field stresses σ_{max} and σ_{min} to stress perturbations $\Delta\sigma_{ij}$ induced by the hydraulic fracture opening. Figure 4.5d shows the undrained pressure perturbation around the hydraulic fracture (2.18) for given Skempton coefficient $B = 0.5$ and undrained Poisson ratio $\nu_u = 0.3$. Pore pressure perturbation is highest at the cavity wall and decreases with distance from the hydraulic fracture. The tensile undrained pressure perturbation reduces pressure along the fracture and hence the fracture shear strength increases. It is evident that the maximum principal shear stress σ_{XY} is much smaller (an order of magnitude) than the deviatoric stress $(\sigma_{max} - \sigma_{min})/2$, (as well as other stress components perturbations). This means that the principal stress directions are approximately the same (modified very little by the hydraulic fracture), and the orientation of the fracture plane favorable to slip is practically unchanged by the hydraulic fracture stress perturbation. Figure 4.7 shows degree of stress rotation by the hydraulic fracture where the change in principal stress directions is minimal.

Slip-activation region $\tau_{max}/\tau_{columb} > 1$ around the propagating hydraulic fracture (4.6) is illustrated in Figure 4.7. L_{max} is defined when slip is activated on the favorably oriented fracture(s) for the first time. It is also apparent that the slip development on the conjugate fractures (with orientation of $180 - \beta$) is identical.

Effective peak shear strength $\tau_p = f_p(\sigma_n - (p_0 + \Delta p_{und}))$ and background shear stress τ^b distribution along pre-existing shear fracture are determined using stress distribution around the hydraulic fracture (4.4) and Mohr relationship (4.5). The normalized peak shear strength $f_p(\sigma_n - (p_0 + \Delta p_{und})) / (\sigma_{min} - p_{tip})$ and normalized

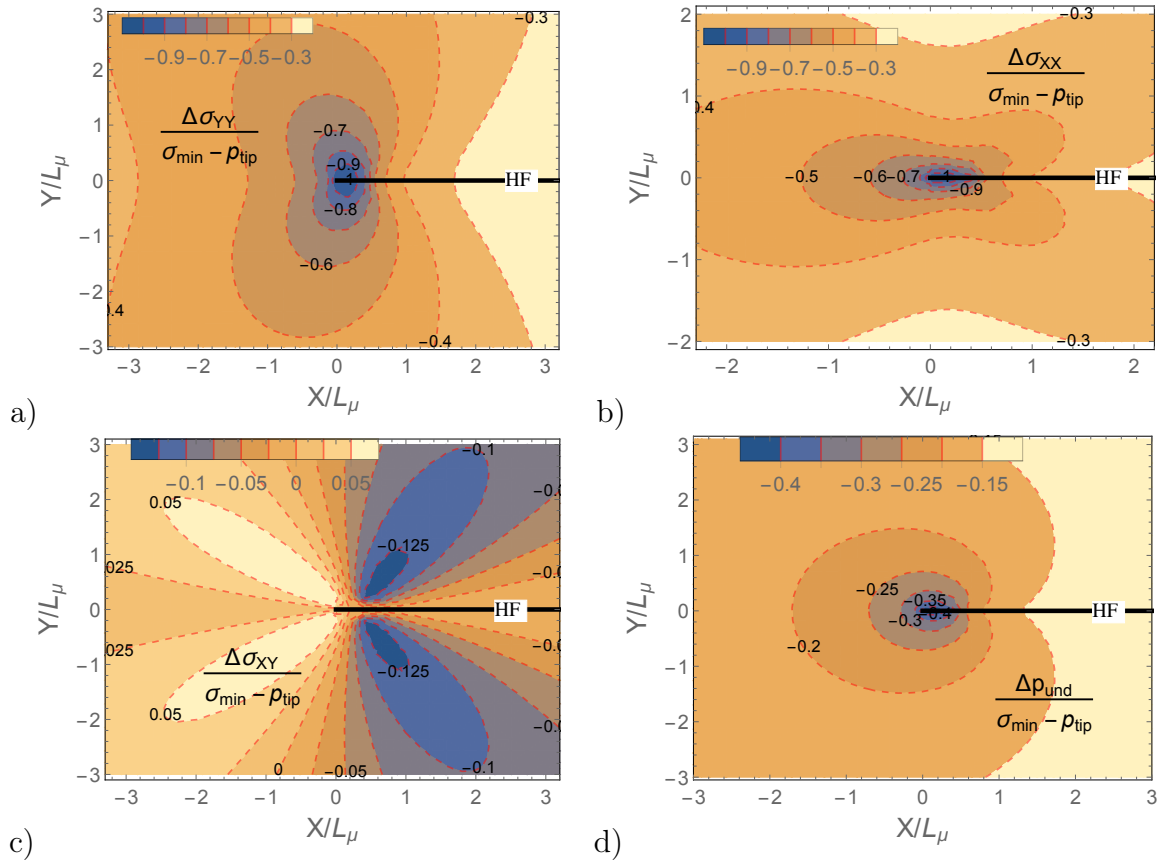


Figure 4.5: Stress perturbations (positive in compression) (a) $\Delta\sigma_{YY}$, (b) $\Delta\sigma_{XX}$, (c) $\Delta\sigma_{XY}$ and (d) pressure perturbation Δp_{und} around propagating hydraulic fracture. Note that the negative X values along the moving coordinates (X, Y) shows the area ahead of the hydraulic fracture.

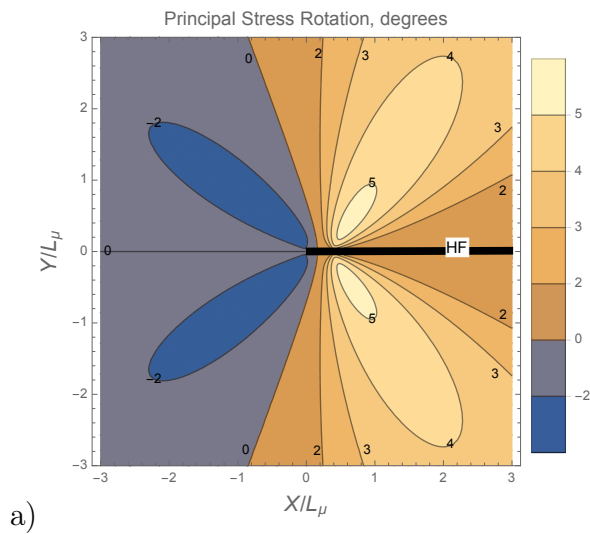
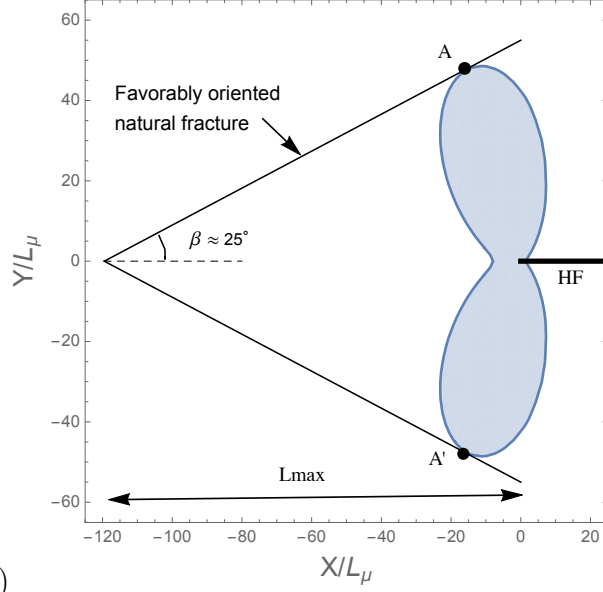


Figure 4.6: Degree of stress rotation by the hydraulic fracture stress perturbation



a)

Figure 4.7: A, A' : Slip activation on conjugate pair of favorably oriented natural fractures during conventional hydraulic fracturing, case study I.

background shear stress $\tau^b/(\sigma_{min} - p_{tip})$ distribution along the shear fracture oriented at $\beta = 20^\circ$ are illustrated in Figure 4.8a at two values of normalized time $Vt/L_\mu = 15.8$ when slip is activated (i.e., $\tau_p = \tau^b$) and $Vt/L_\mu = 19.8$ when nucleation of dynamic slip occurs (Case study I, conventional HF). Figure 4.8b shows shear stress distribution along the crack at the nucleation time $Vt/L_\mu = 19.8$ when length of the slipped portion of the fracture reaches the critical size a_c .

Figure 4.9 shows growth of normalized crack half length a/a_w (a) and slip at the center of slipping patch δ_b/δ_w (b) as a function of normalized time Vt/L_μ for fracture with different orientations located at the maximum distance $L_{max}/L_\mu = 119.5$ during conventional HF (case study I). As the hydraulic fracture advances, the length of slipped portion of the fracture grows quasi-statically. The quasi-static slip turns into dynamic rupture for favorably oriented fractures whereas the expansion of the slipping patch stops for the less favorable oriented fractures (shown by the blue circles). Note that slip develops identically along the fracture which is similarly oriented with regard to the far field stresses, i.e., $180 - \beta$ (Figure 4.7). Slip will

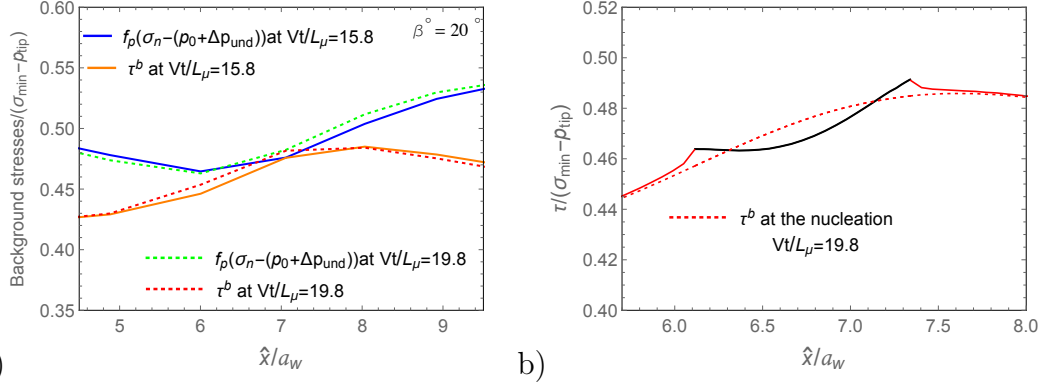


Figure 4.8: (a) Normalized peak background shear strength $f_p(\sigma_n - (p_0 + \Delta p_{und})) / (\sigma_{min} - p_{tip})$ and background shear stress distribution $\tau^b / (\sigma_{min} - p_{tip})$ along fracture oriented at $\beta = 20^\circ$, at two values of normalized time $Vt/L_\mu = 15.8$ and $Vt/L_\mu = 19.8$. (b) Shear stress distribution along the crack at normalized time $Vt/L_\mu = 19.8$ when nucleation of dynamic slip takes place.

not be activated along the fracture which is oriented subparallel to the direction of maximum horizontal stress due to the higher value of the normal stress acting on it, for example: a fracture oriented at an angle of $55 < \beta < 125$ during conventional HF (case study I).

Examples of normalized slip δ/δ_w and stress distribution $\tau / (\sigma_{min} - p_{tip})$ along the fracture oriented at $\beta = 20^\circ$ are plotted in Figure 4.10 at different times. Slip accumulates as the hydraulic fracture approaches closer to the shear fracture. Quasi-static slip turns into dynamic rupture as friction weakens along the slipped portion of the fracture.

For a less critically oriented fracture, slipping patch expansion stops as it can be seen in Figure 4.11 where the normalized slip δ/δ_w and stress distribution $\tau / (\sigma_{min} - p_{tip})$ along the fracture oriented at $\beta = 14^\circ$ are shown for different values of time.

Figure 4.12 shows the values of normalized critical crack half length a_c/a_w , critical time Vt_c/L_μ and slip at the center of slipping patch at instability $(\delta_b)_c/\delta_w$ versus the fracture orientation during conventional hydraulic fracturing for the case study I (refer to Table 4.2). The effect of fluid's viscosity on the instability of slip is investigated with comparison to the slick water HF. Expansion of the crack remains

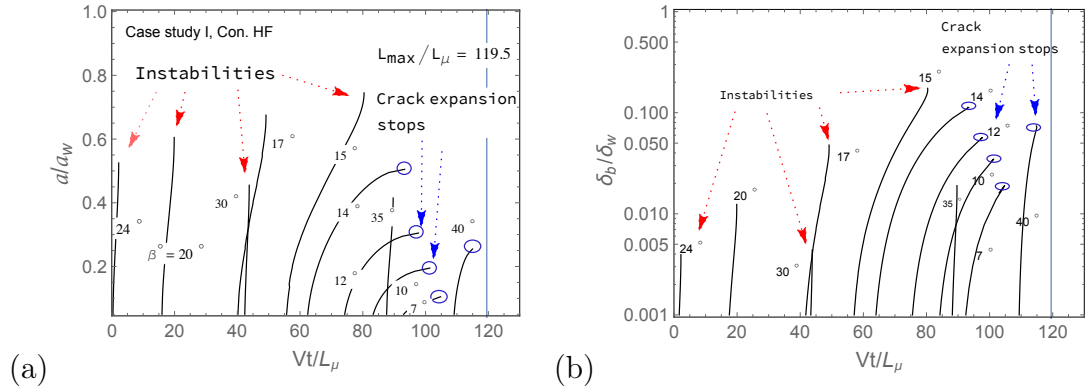


Figure 4.9: Growth of crack half length a/a_w (a) and normalized slip at the center of slipping patch δ_b/δ_w (b) vs. time Vt/L_μ for the fracture with different orientations during conventional HF (case study I). Slip either turns into dynamic rupture (indicated by vertical slopes) or the slipping patch expansion stops (shown by blue circles).

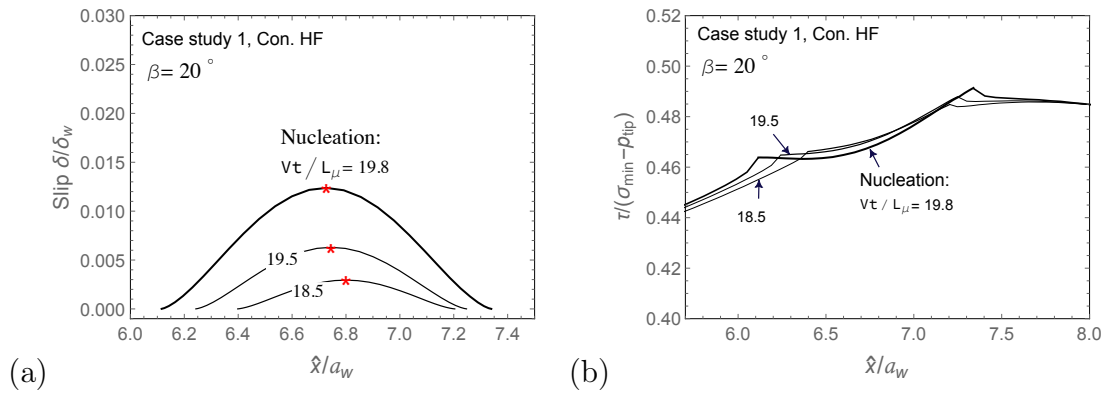


Figure 4.10: (a) Normalized slip δ/δ_w and (b) stress distribution $\tau/(\sigma_{\min} - p_{tip})$ along the fracture oriented at $\beta = 20^\circ$ for different values of time Vt/L_μ (first numerical analysis). The heavy line corresponds to the instability. Center of slipped portion of the crack is shown by star in (a).

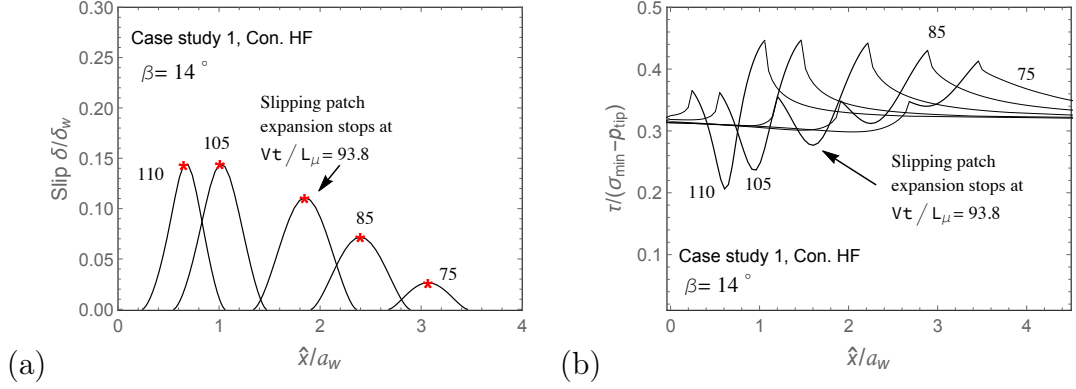


Figure 4.11: (a) Crack expansion stops along the fracture oriented at $\beta = 14^\circ$ where examples of normalized slip δ/δ_w and (b) stress distribution $\tau/(\sigma_{min} - p_{tip})$ are plotted for different values of time Vt/L_μ (Case study I).

quasi-statically for slick water stimulation with smaller length of the tip cavity (shown by dashed line in Figure 4.12).

Effect of in-situ stresses on slip instability is shown on Figure 4.13 by comparing the solutions for the Case I and Case II (Table 4.2) for a conventional HF. It is shown that the expansion of quasi-statically growing slipping patch will be stopped along the fracture with different angles for the case II in which the state of in-situ stresses is further away to the failure.

4.8 Conclusions

Slip (or shearing) of natural fractures plays an important role in the permeability enhancement of tight reservoirs during the hydraulic fracturing process. In this chapter we studied nucleation of dynamic rupture along a natural fracture due to poromechanical interactions with an advancing hydraulic fracture. The length scale of a natural fracture $\sim 1 - 10$ m (constrained by the targeted reservoir layer) is often much smaller than the main hydraulic fracture size ~ 100 m. On the other hand stress perturbations are highest around the tip of a propagating hydraulic fracture. Accordingly, the hydraulic fracture near tip solution that also accounts for the presence of a lag was implemented to investigate instability of slip on the

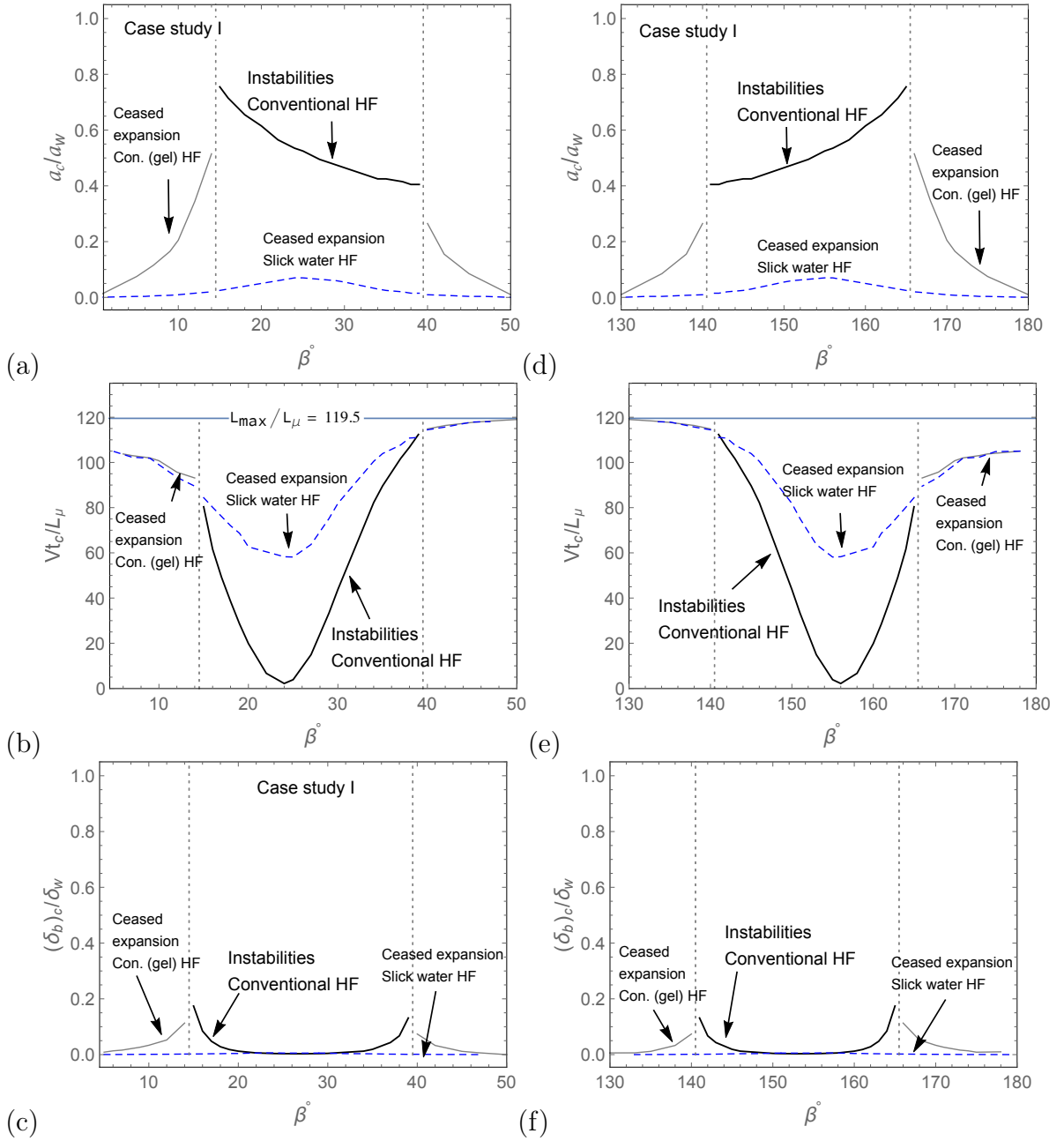


Figure 4.12: Critical crack half-length a_c/a_w (a, d), critical (or a ceased expansion) time Vt_c/L_μ (b, e) and (c, f) slip at the center of slipping patch at instability $(\delta_b/\delta_w)_c$ as a function of fracture orientation for conventional (gel) compared to slick water hydraulic fracturing (case study I). The values of maximum crack expansion (i.e., no instability) in the slick water stimulation are presented by dashed line for the comparison.

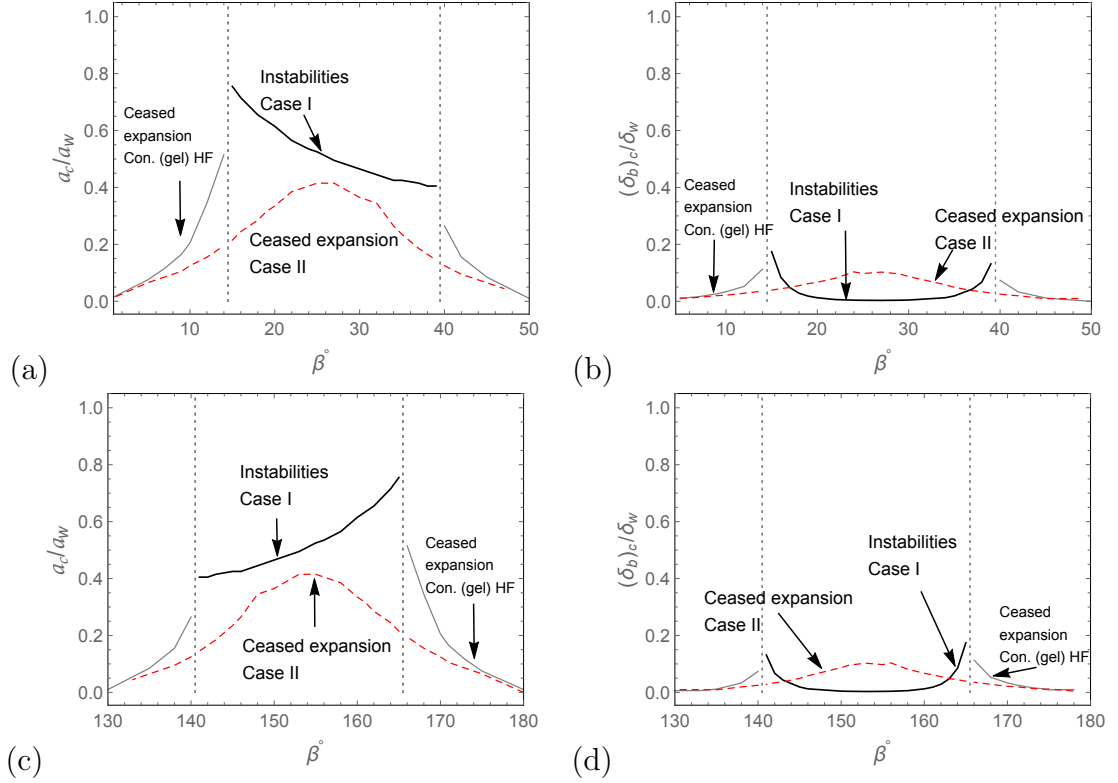


Figure 4.13: Comparison of the two performed numerical analyses on instability of slip along the natural fracture (under different in-situ stress conditions) for conventional HF. Slip grows stably along the fracture which is subjected to the less critical effective principal stress ratio (case study 2 shown by red dashed line).

natural fracture.

Nucleation of dynamic slip on a frictional fracture approached by a hydraulic fracture depends on state of in-situ stresses (e.g., stress anisotropy and magnitude), hydraulic fracture pressure, fluid viscosity, friction and angle of approach. In the limit of short time scales, the pore pressure inside the (partially mineralized) natural fracture is equilibrated with the medium undrained pore pressure. The results show that slip grows dynamically along the critically oriented fracture in the conventional hydraulic fracture treatment if the state of ambient stress is close enough to the failure condition (case study I vs. case study II), which is consistent with the microseismic field observations [17]. Slip instability takes place when the extent of the slipping patch reaches the critical length $\sim a_w$. Only a subset of possible fracture orientations result

in seismic slip, while fractures that are less favorably oriented can still accumulate significant aseismic slip, and thus contribute to permeability enhancement. (This is one of the reasons why it is important to quantify both seismic and aseismic induced slip).

Effect of fluid viscosity on instability of slip was numerically analyzed for the conventional (gel) compared to the slick water treatments. It is shown that the higher values of the fluid viscosity results in the higher stress perturbation around the tip which drives the critically oriented natural fractures to the instability.

CHAPTER 5: NUCLEATION OF DYNAMIC SLIP ALONG A NATURAL FRACTURE CROSSED BY A PROPAGATING HYDRAULIC FRACTURE

5.1 Introduction

The aim of this chapter is to investigate dynamic slip nucleation on a natural fracture which intersects a propagating hydraulic fracture. In the previous chapter we studied dynamic slip activation on a natural fracture as a result of interaction with an advancing hydraulic fracture. Here the model is extended to examine occurrence of seismic slip on the natural fracture that did not slip dynamically before the hydraulic fracture crosses it. We consider interaction of the limited size natural fracture with the propagating hydraulic fracture under assumptions of (i) one-way interaction in which slip along the natural fracture does not perturb the hydraulic fracture propagation and (ii) that the natural fracture is assumed to lie at the edge of the loaded hydraulic fracture. The latter considers the hydraulic fracture's surface effect on the instability of slip along the edge fracture. Furthermore, Daneshy [78] experimentally showed that the natural fractures with sizes smaller than the hydraulic fracture will not be able to change the orientation of the propagating hydraulic fracture.

The edge crack quasi-static slip growth depends on the stress perturbation by the hydraulic fracture as well as pressure diffusion into the fracture. As time progresses, fluid diffusion process becomes the dominant mechanism for instability than the tip stress perturbation (which is decreasing as the hydraulic fracture propagating further from the fracture). Slip initiates at the crack mouth due to increase in the pore pressure that lowers the fracture strength.

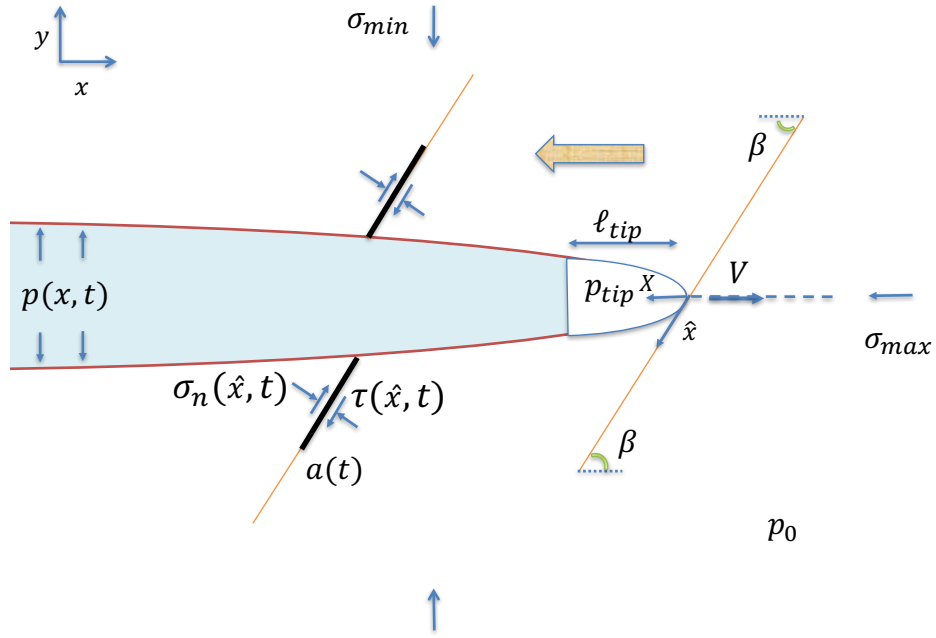


Figure 5.1: The semi-infinite hydraulic fracture crosses the pre-existing shear fracture. Pore pressure diffusion into the edge cracks activates slip along them.

5.2 Model

Consider the pre-existing natural fracture crossed at an angle β by the hydraulic fracture propagating in the direction of maximum principal stress (Figure 5.1). The hydraulic fracture is growing in an impermeable, infinite linear elastic medium with constant velocity V and is loaded internally by fluid pressure p (see 4.2).

Slip initiates along the edge crack(s) as the frictional strength $f_p(\sigma_n - p)$ drops due to increase in pore pressure by diffusion of fluid from the hydraulic fracture. While the pore pressure evolves inside the edge crack(s) the extent of slipped zone $a(t)$ grows quasi-statically before the nucleation of dynamic slip.

We will examine nucleation of dynamic rupture along the fracture (with different orientations), which only has slipped quasi-statically before the crossing. It has been assumed that friction along the edge crack has not weakened from the peak friction ($f/f_p = 1 - \delta/\delta_w > 0.85$ everywhere along the fracture with the ceased expansion

in conventional HF and $f/f_p = 1 - \delta/\delta_w > 0.99$ in slick water HF, Figure 4.12c). The results in the following sections are discussed only for the crack at the edge of hydraulic fracture in the positive local coordinate system.

5.3 Pore pressure along the edge crack

Pore pressure inside the edge crack $0 \leq \hat{x} < \infty$ is govern by equations (4.11-4.13). The numerical solution is defined using two boundary conditions: the hydraulic fracture pressure at the crack mouth and p_0 at the far boundary respectively, and an initial condition $p_0 + \Delta p_{\text{und}}$ (at the crossing time $Vt/L_\mu = 0$). The pore pressure is function of in-situ stresses, hydraulic fracture pressure, diffusivity coefficient and stiffness ratio (4.14) with the fracturing fluid replacing the formation fluid. Although the pore fluid initially flows from the natural fracture into the hydraulic fracture (due to the lower pressure of the tip), the pore pressure inside the edge crack increases as a result of pressure diffusion form the hydraulic fracture. The pore pressure growth is the mechanism that causes crack strength to decline and slip to propagate.

Figure 5.2 shows an example of development of normalized pore pressure vs. time along the edge crack with orientation $\beta = 10^\circ$, non-dimensional diffusivity coefficient $\alpha = 0.004$ and stiffness ratio $\Gamma = 0.08$, respectively (during conventional HF, case study I).

5.4 Slip along the edge crack

The change in shear stress due to slip along the edge crack has a different kernel in the elasticity equation

$$\tau(\hat{x}, t) = \tau^b(\hat{x}, t) - \frac{E'}{4\pi} \int_0^a \frac{d\delta(\hat{s}, t)}{d\hat{s}} G_{\hat{x}\hat{y}}(\hat{x}, \hat{s}) d\hat{s} \quad (5.1)$$

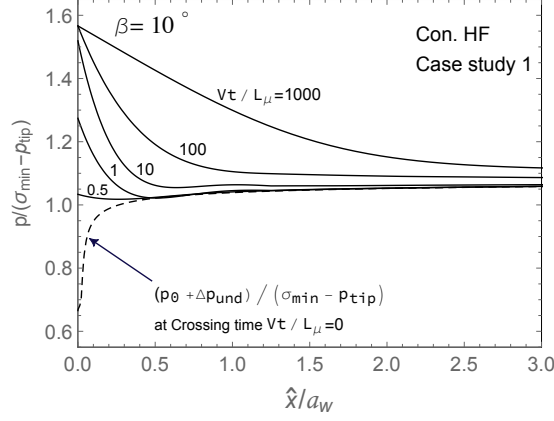


Figure 5.2: Normalized pore pressure evolution with time inside the edge crack inclined at $\beta = 10^\circ$ during conventional HF, case study I.

where the influence functions G_{ijk} are given in Appendix D. The normal stress distribution along the fracture plane in the expression for the natural fracture strength $\tau = f(\sigma_n - p)$ is given by:

$$\sigma_n(\hat{x}, t) = \sigma_n^b(\hat{x}, t) - \frac{E'}{4\pi} \int_0^a \frac{d\delta(\hat{s}, t)}{d\hat{s}} G_{\hat{x}\hat{y}\hat{y}}(\hat{x}, \hat{s}) d\hat{s} \quad (5.2)$$

where the resultant normal stress distribution is the addition of stress induced in material by the hydraulic fracture in absence of the crack σ_n^b and the normal stress change due to slip. The contribution of slip on the local normal stress distribution (which is due to the surface effect) is zero $G_{\hat{x}\hat{y}\hat{y}} = 0$ for a fracture in an infinite medium while the contribution changes the local normal stress distribution $\sigma_n(\hat{x}, t)$ for the edge crack.

5.4.1 Scaling and numerical approach

The system of equations (5.1-5.2) are normalized along the coordinate $\hat{\xi} = 2\hat{x}/a - 1$ using the scaling defined in (4.8). The normalized crack length a/a_w and normalized slip δ/δ_w (i.e., the problem unknowns) can be expressed as functions of normalized time Vt/L_μ , non-dimensional peak friction f_p , normalized residual friction f_r/f_p , the length parameter ς , diffusivity coefficient α and stiffness ratio Γ (i.e., the problem

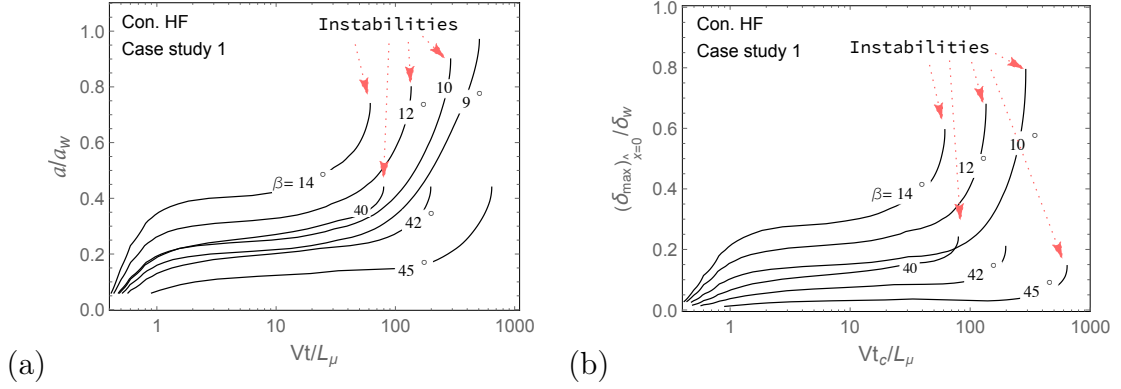


Figure 5.3: Growth of edge crack length a/a_w (a) and normalized slip at the crack mouth δ_{max}/δ_w (b) vs. time Vt/L_μ for the crack with different orientations during conventional HF.

knowns) for an inclination β , pore pressure ratio p_0/σ_{min} and in-situ stress ratio $\sigma_{max}/\sigma_{min}$. The normalized form of slip formulation and the method of solution are provided in Appendix F.

5.5 Results

5.5.1 The model with unlimited weakening friction

Slip accumulates quasi-statically along the edge crack as the pressure front advances inside the fracture. Figure 5.3 shows growth of edge crack length a/a_w (a) and slip at the crack mouth δ_{max}/δ_w (b) as a function of normalized time Vt/L_μ for the fracture with different orientations during conventional HF. As time progresses, and with continuous reduction of the friction, the length of the slipped portion of the fracture will eventually grow dynamically.

An example of normalized slip δ/δ_w and stress distribution $\tau/(\sigma_{min} - p_{tip})$ along the edge crack with the orientation $\beta = 40^\circ$ are plotted on Figure 5.4. Instability will occur as the pore pressure evolves inside the edge crack (shown by heavy line).

Normalized critical edge crack length a_c/a_w , time Vt_c/L_μ and slip at the crack mouth $(\delta_{max})_c/\delta_w$ at instability are plotted in Figure (5.5) for different orientations of the edge crack. The critical edge crack length $a_c \sim a_w$ is mainly a function of the frac-

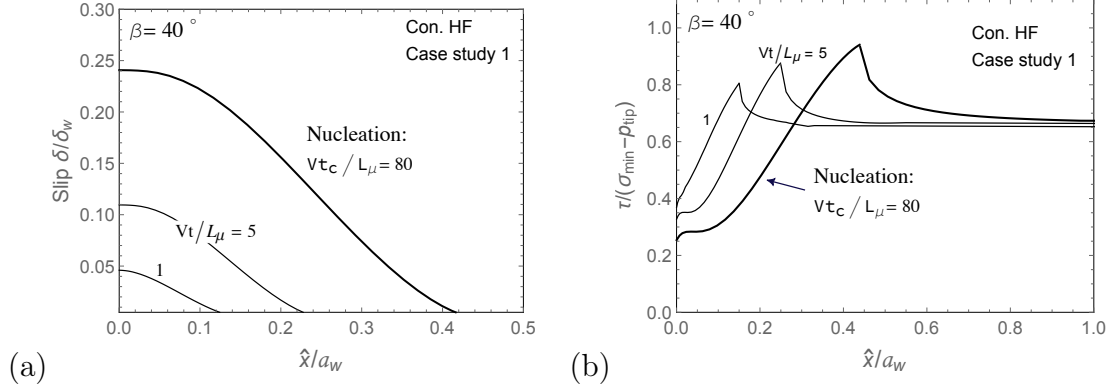


Figure 5.4: (a) Normalized slip δ/δ_w and (b) stress distribution $\tau/(\sigma_{min} - p_{tip})$ along the edge crack oriented at $\beta = 40^\circ$ at different values of normalized time Vt/L_μ . The heavy line corresponds to the instability.

ture orientation comparison with the slick water HF shown by gray line) and grows significantly larger for the low angle fractures (with the lowest values of the background shear stress). While the nucleation time depends on the fracture ordination and fluid viscosity and becomes unbounded for the less critically oriented fractures. The edge crack extends larger and at a longer time before nucleation for the lower values of the effective principal stress ratio (Case study 2, shown by dashed line). The normalized critical slip at the crack mouth $(\delta_{max})_c/\delta_w$ is also only a function of the fracture orientation where it increases for the less critically stressed fractures.

5.5.2 Effect of residual friction

As friction attains its residual value in the slip weakening model, crack grows more stably (compared to the unlimited weakening model) due to the change in the frictional strength of the fracture. The effect of normalized residual friction $f_r/f_p = 0.6$ on the extension of edge crack a/a_w and slip at the crack mouth δ_{max}/δ_w with time Vt/L_μ has been plotted in Figure (5.6) for different orientations of the edge crack during the slick water HF. The extent of the crack at nucleation a_c/a_w grows larger (compared to the unlimited weakening model) for the fractures for which friction has reached the residual value before nucleation (i.e., $\delta/\delta_w \geq 0.4$, Figure 5.5) extending

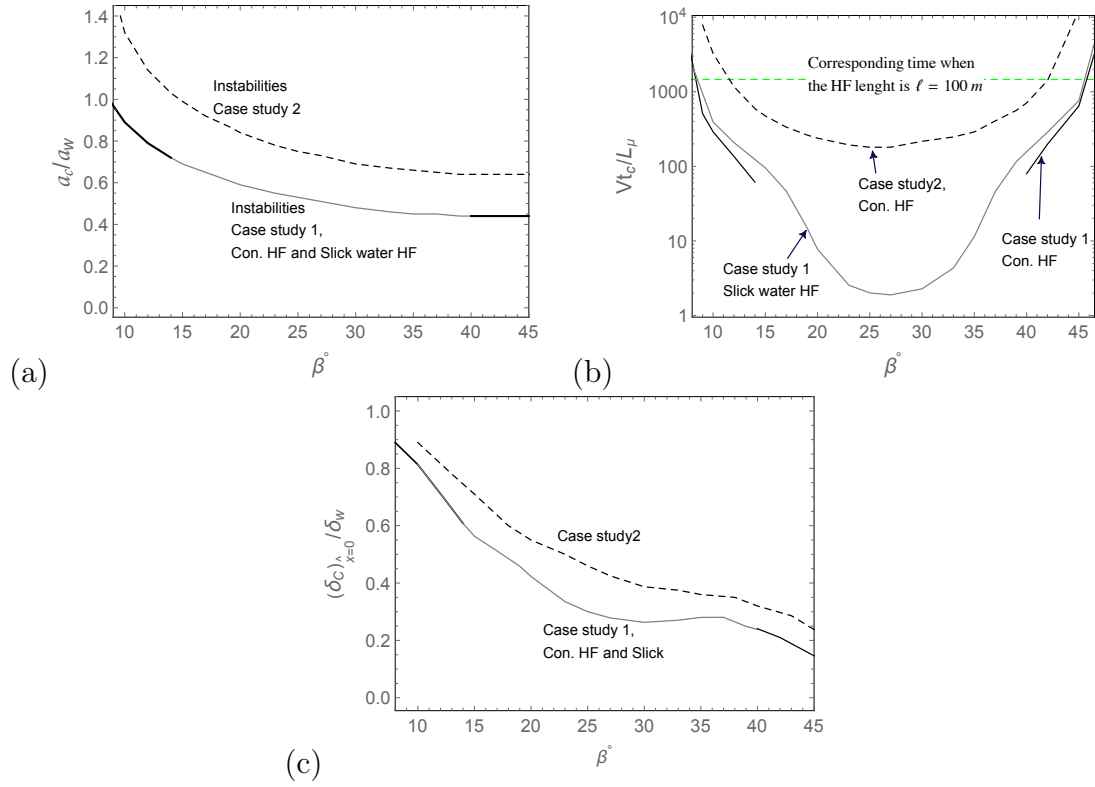


Figure 5.5: Normalized critical edge crack length a_c/a_w (a), critical time Vt_c/L_μ (b) and (c) critical slip at the crack mouth $(\delta_{max})_c/\delta_w$ for the fracture with different orientations. The results are compared to the slick water HF (shown by gray line) and to the case study 2 with lower effective principal stress ratio (shown by dashed line).

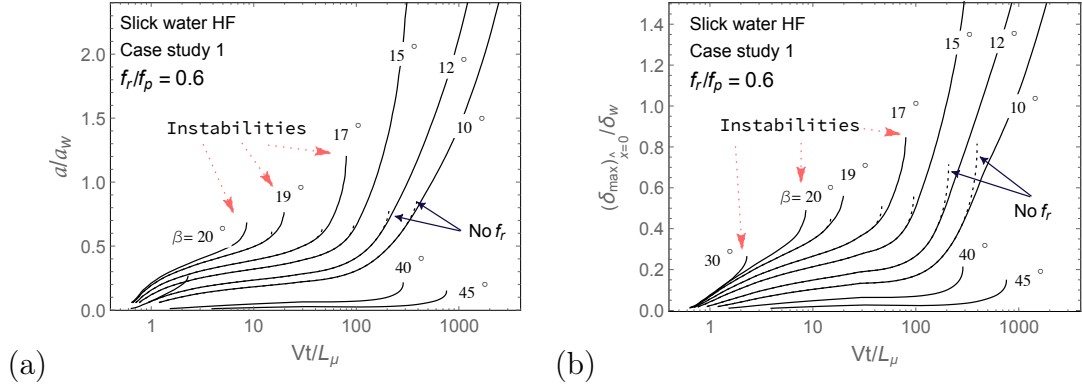


Figure 5.6: Growth of the edge crack length a/a_w (a) and (b) slip at the crack mouth δ_{max}/δ_w with time for the fracture with different orientation in the model with residual friction $f_r/f_p = 0.6$ during slick water HF (case study I). The results are compared to the model with no residual friction (shown by dotted line).

to a stable crack propagation for the fractures with least background shear stress. For fractures which nucleated before the friction reaches the residual value, dynamic formulation should be considered to study the crack propagation, however, as it is forecasted by Garagash and Germanovich [64] the dynamic slip is predicted to arrest due to the effect of residual friction (i.e., a dynamic transient) when the residual shear strength $\tau_p = f_r (\sigma_n - p)$ is larger than the shear stress τ .

CHAPTER 6: DISCUSSION

6.1 Relation to existing cases of HF induced seismicity

Interaction of a hydraulic fracturing fluid injection with natural fractures [77, 128, 129] and faults [Davies et al., 13, and references therein] may include the following scenarios.

1. Direct hydraulic stimulation of a fault (when an injection interval of the well intersects the fault) resulting in the fault hydraulic fracture.
2. A dominant opening mode hydraulic fracture propagating in the maximum horizontal stress direction intersecting a fault followed by either (*i*) diverting into and opening of the fault, or (*ii*) crossing, if the fault is mechanically and hydraulically healed, or (*iii*) arresting, if the injected fluid can be accommodated by the leak-off into the intersected permeable fault zone and/or by storage in the compliant “parent” fracture, *effectively preventing the fluid pressure build up in the arrested HF* from reaching the level of the fault normal stress and, therefore, preventing the fault opening (case *2i*).
3. A distributed network of hydraulically stimulated, mixed-mode pre-existing and induced fractures, which allow for enhanced communication of the fluid pressure from the well to a proximal fault, without opening the latter.

The in situ stress anisotropy (magnitude of the horizontal deviatoric stress), the pervasiveness and strength of fractures in the pre-existing fracture network(s), as well as, the orientation, structure and properties of the fault zone (e.g., the mechanical weakness of the fault core and the permeability of the fractured and foliated rocks/gouge in the fault damage zone) are expected to shape the hydraulic fracture propagation and the HF-fault interaction, as outlined in the above scenarios.

For example, a certain degree of in situ stress anisotropy and/or lack of mechanically weak pre-existing fractures would favor the scenario (2) of a “localized” HF propagation in the direction of the maximum in situ stress prior to the fault intersection, while a low permeability, but mechanically weak intersected fault would favor the HF diversion into the fault as in the case (2*i*). The model developed in Chapter 3 is deemed applicable to the case (1) of the direct HF injection into a fault, and, as a first order approximation, to the case (2*i*), if, firstly, the effects of the stress perturbations due to the “parent” HF and due to the non-trivial intersection geometry can be reasonably neglected, and, secondly, that the partition of the newly injected fluid between the parent fracture and the fault-diverted branch can be ascertained.

Stimulation of pre-existing natural fractures by hydraulic fracturing process is necessary in the productivity enhancement of the unconventional reservoirs with very low matrix permeability. Stress/ pore pressure perturbation caused by the main hydraulic fracture (of the order of 100 meters) induces unstable slip along the adjacent natural fractures that often have limited extent (on the order of 1 meter). As it is discussed in chapter 4, instability of slip is induced only on a subset of possible fracture orientations (i.e., critically oriented), which is consistent with microseismic field observations [17]. While less favorably oriented fractures also contribute to the reservoir permeability enhancement as they may accumulate significant aseismic slip. Yet, the slip-stimulated rock volume of the fracture sets with nucleated dynamic slip would be larger than the less critically oriented fracture sets as the entire surfaces of the pre-existing fractures will undergo slip-induced stimulation.

The HF-induced *microseismicity* is ubiquitous and, for the most part, it is interpreted to occur in the stimulated reservoir rock. As such, it is used as a diagnostic tool for hydraulic fracturing treatments to infer the approximate extent and the orientation of the final fracture(s) [17, 16]. Few documented cases of the HF intersecting and potentially propagating along a well-developed fault (scenario (1) and (2*i*) in the

above) within the hydraulically fractured reservoir [130, 131] showed a tendency for increased count and magnitude of events associated with the reservoir fault, yet still remaining within the microseismic realm (negative seismic moment magnitude).

Few known cases of larger seismicity (moment magnitude 2 and larger) that were correlated spatially and temporarily to hydraulic fracturing operations in deep shale plays, e.g. in Blackpool, England [23], Ohio [28], Alberta [21, 15], have been inferred to *nucleate in or at the contact with the basement rock*, some 100s of meters to a km deeper than the depth of hydraulic fracturing stages. The fracturing fluid buoyancy (compared to the host rock) limits the extent of the downward fracture growth, making it unlikely that the open-mode hydraulic fracture could propagate these distances towards the inferred nucleation site in the basement. Instead, it is more likely in these field cases that the HF have intersected a developed fault zone (see scenarios (2iii) or (3) in the above) extending from the reservoir to the basement, which, due to either intrinsically high or slip-refreshed permeability, has then communicated the HF-induced pore pressure perturbation downdip to the nucleation site in the basement. The absence of large seismic events nucleated within the reservoir, and more generally, along the path of the fault within the sedimentary strata above the basement, may be attributed to the interbedded nature of clastic rock, where the frictionally stable shale beds with higher organic content [132] can effectively arrest the dynamic slip if nucleated within the brittle, low-organic content (e.g. sandstone) beds.

In summary, existing field observations of the HF-induced seismicity suggest that the opening mode hydraulic fracturing of a fault, as considered in Chapter 3, may be one of prevalent mechanisms for nucleating *microseismicity within the reservoir*. However, for the known cases of more significant HF-related seismicity, it has likely been nucleated at (or near) the basement extension of the reservoir faults, i.e. downdip from the hydraulically fractured reservoir, by means of a “long-distance” communi-

cation of the pore pressure changes by diffusion and/or poroelastic stress changes. Whether or not significant seismicity can be nucleated on the reservoir faults *in-reservoir*, as the result of the direct interaction with the hydraulic fracturing, remains an open question.

CHAPTER 7: CONCLUSIONS AND RECOMMENDATIONS

This dissertation addresses different scenarios of interactions between a hydraulic fracturing fluid injection with a fault/fracture. Particularly, semi-analytical approaches are carried out to study the involved physical processes in the following scenarios for which the main results are summarized here.

1. Direct hydraulic injection into a fault which results in a mixed-mode fault hydraulic fracture

- The slip patch grows as a result of the reduction of the fault strength to zero along the hydraulic fracture, the open part of the fault, as well as the decrease of the fault frictional strength due to the normal stress perturbation ahead of the hydraulic fracture tip.
- Slip instability on the fault is mainly controlled by the hydraulic fracture length (i.e., the size of the fully unloaded fault segment at a given time) and is only weakly dependent on the magnitude of the stress perturbation ahead of the propagating hydraulic fracture, or the HF propagation regime.
- The growth of the fault slipping patch remains stable when the background shear stress τ_0 is lower than the residual fault strength τ_r under ambient conditions.
- Injection into a fault with $\tau_0 > \tau_r$ will result in a dynamic shear rupture.
- Nucleation of dynamic slip takes place when the hydraulic fracture grows to the critical size ℓ_c , which is vanishingly small $\propto \tau_p - \tau_0$ for critically-stressed faults (i.e., when the background stress approaches the fault peak strength, $\tau_0 \rightarrow \tau_p$) and is diverging as $\propto 1/(\tau_0 - \tau_r)$ when the stability

boundary is approached ($\tau_0 \rightarrow \tau_r$).

- No dynamic slip transients are predicted when background shear stress is less than the residual fault strength.
- The solution for the critical size of hydraulic fracture (HF) leading to nucleation of dynamic slip was established. It allows to infer the corresponding fluid injection volume that may lead to slip instability on a fault with given frictional properties and background stress.

2. A hydraulic fracture propagating in the direction of maximum horizontal stress induces dynamic slip on a natural fracture due to the stress perturbation.

- Nucleation of slip on the frictional fracture approached by the hydraulic fracture depends on the state of in-situ stresses, hydraulic fracture pressure, angle of approach and friction of the fracture.
- The undrained stress perturbations around the propagating hydraulic fracture is proportional to the length of the tip of the hydraulic fracture ℓ_{tip} .
- Slip instability occurs on the critically stressed and favorably oriented strike-slip fracture as the slipping patch reaches the critical length $\sim E' / (\sigma_{min} - p_{tip}) \times \delta_w$.

3. Pore pressure increase by diffusion induces slip instability on a natural fracture crossed by a propagating hydraulic fracture.

- The size of slipped region at nucleation follows the similar scaling $\sim E' / (\sigma_{min} - p_{tip}) \times \delta_w$ that is also proportional to the effective principal stress ratio $(\sigma_{max} - p_0) / (\sigma_{min} - p_0)$
- The scaling changes when the residual friction is attained before nucleation. The fracture may grow stably under low enough background shear stress.

7.1 Recommendations for future research

Our recommendations for the course of future studies on the topic are as follows:

- We considered a one-way mechanical coupling between the hydraulic fracture and the natural fracture. The future work may consider fully coupled interactions of the hydraulic fracture and the natural fracture.
- The results of this study may be extended to the more complex configurations of multiple fracture interactions in the hydraulic fracture stimulation.
- The full effect of poroelastic coupling has not been considered in this work. Further developments could then investigate complete interactions between the pore fluid and the rock.
- The role of dilatancy, and stabilizing effect of pore fluid pressure reduction on slip development, might be considered in future studies by the use of a model that couples the normal deformation (i.e., change of fracture aperture) to the shear displacement and fluid flow along the fracture.
- A better understanding of the process may be achieved applying a more detailed friction model.
- Further investigations may consider different HF geometries and propagation regimes.

Bibliography

- [1] M.K. Hubbert and D.G. Willis. Mechanics of hydraulic fracturing. *Trans. AIME*, 210:153–168, 1957.
- [2] M.P. Cleary. Theory and application of hydraulic fracturing technology. *Mechanics of elastic and inelastic solids*, 5:267–289, 1983.
- [3] C.F. Tsang, J. Birkholzer, and J. Rutqvist. A comparative review of hydrologic issues involved in geologic storage of co2 and injection disposal of liquid waste. *Environ. Geol.*, 54(8):1723–1737, 2008.
- [4] S. M. Johnson and J. P. Morris. Hydraulic fracturing mechanisms in carbon sequestration applications. *American Rock Mechanics Association*, 43rd U.S. Rock Mechanics Symposium & 4th U.S. Canada Rock Mechanics Symposium, 2009.
- [5] Z.P. Bazant and H. Ohtsubo. Geothermal heat extraction by water circulation through a large crack in a hot dry rock mass. *Int. J. Numer. Anal. Methods Geomech.*, pages 317–327, 1978.
- [6] K. Hayashi and H. Abe. Opening of a fault and resulting slip due to injection of fluid for the extraction of geothermal heat. *J. Geophys. Res.*, 87:1049–1054, 1982.
- [7] F. H. Cornet, J. Helm, H. Poitrenaud, and A. Etchecopar. Seismic and aseismic slips induced by large-scale fluid injections. *PAGEOPH*, 150:563–583, 1997.
- [8] J. H. Healy, W. W. Rubey, D. T. Griggs, and C. B. Raleigh. The denver earthquakes. *Science*, 161:1301–1310, 1968.
- [9] C. Frohlich, C. Hayward, B. Stump, and E. Potter. The dallas-fort worth earthquake sequence: October 2008 through may 2009. *Bull. Seis. Soc. Am.*, 101:327–340, 2011.
- [10] S. Horton. Disposal of hydrofracking waste fluid by injection into subsurface aquifers triggers earthquake swarm in central arkansas with potential for damaging earthquake. *Seismol. Res. Lett.*, 83 (2):250–260, 2012.
- [11] W. L. Ellsworth. Injection-induced earthquakes. *Science*, 341:1225942, 2013.
- [12] E. L. Majer, R. Baria, M. Stark, S. Oates, J. Bommere, B. Smith, and H Asanuma. Induced seismicity associated with enhanced geothermal systems. *Geothermics*, 36:185–222, 2007.
- [13] R. Daviesa, G. Foulgera, A. Bindleya, and P. Stylesb. Induced seismicity and hydraulic fracturing for the recovery of hydrocarbons. *Marine and Petroleum Geology*, 45:171–185, August 2013.

- [14] G. M. Atkinson, D. W. Eaton, H. Ghofrani, D. Walker, B. Cheadle, R. Schultz, R. Shcherbakov, K. Tiampo, J. Gu, R. M. Harrington, Y. Liu, M. van der Baan, and H. Kao. Hydraulic fracturing and seismicity in the western Canada sedimentary basin. *Seism. Res. Lett.*, 87(3):631–647, 2016.
- [15] X. Bao and D. W. Eaton. Fault activation by hydraulic fracturing in western Canada. *Science*, page to appear, 2016.
- [16] S. C. Maxwell, T. Urbancic, N. Steinsberger, and R. Zinno. Microseismic imaging of fracture complexity in the Barnett shale (SPE 77440). In *SPE Annual Technical Conference*, pages 1–9, San Antonio, Texas, 29 September - 2 October, 2002.
- [17] J. T. Rutledge, W. S. Phillips, and M. J. Mayerhofer. Faulting induced by forced fluid injection and fluid flow forced by faulting: An interpretation of hydraulic-fracture microseismicity, carthage cotton valley gas field, texas. *Bull. Seismol. Soc. Am.*, 94(5):1817–1830, 2004.
- [18] P. Segall and S. Lu. Injection-induced seismicity: Poroelastic and earthquake nucleation effects. *J. Geophys. Res. Solid Earth*, 120:5082–5103, 2015.
- [19] K. Deng, Y. Liu, and R. M. Harrington. Poroelastic stress triggering of the december 2013 crooked lake, alberta, induced seismicity sequence,. *Geophys. Res. Lett.*, 43:8482–8491, 2016.
- [20] Nolte K.G. Economides, M.J. *Reservoir Stimulation*. Wiley, 3rd edition, 2000.
- [21] R. Schultz, S. Mei, D. Pană, V. Stern, Y. Jeffrey Gu, A. Kim, and D. Eaton. The cardston earthquake swarm and hydraulic fracturing of the exshaw formation (alberta bakken play). *Bull. Seismol. Soc. Am.*, 105(6), December 2015.
- [22] National Research Council. Induced seismicity potential in energy technologies. [http://www.nap.edu/catalog/13355/inducedâseismicityâpotentialâinâenergyâtechnologies](http://www.nap.edu/catalog/13355/induced%seismicity%potential%in%energy%technologies), National Academies Press, Washington, DC 2013.
- [23] C. J. de Pater and S. Baisch. Geomechanical study of Bowland shale seismicity: Synthesis report. Technical Report 71, Department of Energy and Climate Change, Cadrilla Resour., Staffordshire, UK, Nov. 2 2011.
- [24] A. A. Holland. Earthquakes triggered by hydraulic fracturing in south-central oklahoma. *Bull. Seismol. Soc. Am.*, 103:1784–1792, 2013.
- [25] BC Oil and Gas Commission. Investigation of observed seismicity in the horn river basin. <http://www.bcogc.ca/document.aspx?documentID=1270>, page 29, 2012.
- [26] BC Oil and Gas Commission. Investigation of observed seismicity in the montney trend. [http://www.bcogc.ca/sites/default/files/documenta-tion/technicalâreports/investigationâobservedâseismicityâmontneyâtrend.pdf](http://www.bcogc.ca/sites/default/files/documenta-tion/technical%reports/investigation%observed%seismicity%montney%trend.pdf), page 32, 2014.

- [27] P. A. Friberg, G. M. Besana-Ostman, and I. Dricker. Characterization of an earthquake sequence triggered by hydraulic fracturing in harrison county, ohio. *Seismol. Res. Lett.*, 85(2):462, 2014.
- [28] R. J. Skoumal, M. R. Brudzinski, and B. S. Currie. Earthquakes induced by hydraulic fracturing in poland township, ohio. *Bull. Seismol. Soc. Am.*, 105:189–197, 2015.
- [29] R. Schultz, V. Stern, M. Novakovic, G. Atkinson, and Y. J. Gu. Hydraulic fracturing and the crooked lake sequences: Insights gleaned from regional seismic networks. *Geophys. Res. Lett.*, 42(8):2750–2758, 2015.
- [30] D. Eaton and A. Babaie Mahani. Focal mechanisms of some inferred induced earthquakes in alberta, canada. *Seismol. Res. Lett.*, 86:1078–1085, 2015.
- [31] S. Maxwell. Unintentional seismicity induced by hydraulic fracturing. *CSEG Rec.*, 38:40–49, October 2013.
- [32] M. J. Economides and K. G. Nolte, editors. *Reservoir stimulation*. John Wiley and Sons, Chichester UK, 3rd edition, 2000.
- [33] J. I. Adachi. *Fluid-Driven Fracture in Permeable Rock*. PhD thesis, University of Minnesota, 2001.
- [34] S.A. Khristianovic and Y.P. Zheltov. Formation of vertical fractures by means of highly viscous fluids. In *Proc. 4th World Petroleum Congress, Rome*, volume II, pages 579–586, 1955.
- [35] T. K. Perkins and L. R. Kern. Widths of hydraulic fractures. *J. Pet. Tech., Trans. AIME*, 222:937–949, 1961.
- [36] J. Geertsma and F. De Klerk. A rapid method of predicting width and extent of hydraulic induced fractures. *JPT*, 246:1571–1581, 1969.
- [37] R.P. Nordgren. Propagation of vertical hydraulic fractures. *J. Pet. Tech.*, 253:306–314, 1972. (SPE 3009).
- [38] D. I. Garagash. Scaling of physical processes in fluid-driven fracture: Perspective from the tip. In F. Borodich, editor, *IUTAM Symposium on Scaling in Solid Mechanics*, volume 10 of *IUTAM Bookseries*, pages 91–100. Springer, 2009.
- [39] D. A. Spence and D. L. Turcotte. An elastostatic model of stress accumulation on the san andreas fault. *Proc. Roy. Soc. of London, Ser. A*, 349:xx, 1976.
- [40] J. R. Lister. Buoyancy-driven fluid fracture: The effects of material toughness and of low-viscosity precursors. *J. Fluid Mech.*, 210:263–280, 1990.

- [41] J. Desroches, E. Detournay, B. Lenoach, P. Papanastasiou, J. R. A. Pearson, M. Thiercelin, and A. H-D. Cheng. The crack tip region in hydraulic fracturing. *Proc. Roy. Soc. London, Serie A(447)*:39–48, 1994.
- [42] R.S. Carbonell, J. Desroches, and E. Detournay. A comparison between a semi-analytical and a numerical solution of a two-dimensional hydraulic fracture. *Int. J. Solids Structures*, 36(31-32):4869–4888, 1999.
- [43] J. I. Adachi and E. Detournay. Self-similar solution of a plane-strain fracture driven by a power-law fluid. *Int. J. Numer. Anal. Methods Geomech.*, 26:579–604, 2002.
- [44] D. I. Garagash. Propagation of a plane-strain hydraulic fracture with a fluid lag: Early-time solution. *Int. J. Solids Structures*, 43:5811–5835, 2006.
- [45] E. Detournay. Fluid and solid singularities at the tip of a fluid-driven fracture. In D. Durban and J.R.A. Pearson, editors, *Proc. IUTAM Symp. on Non-Linear Singularities in Deformation and Flow, Haifa*, pages 27–42, Dordrecht, 1999. Kluwer Academic Publ.
- [46] D. I. Garagash and E. Detournay. The tip region of a fluid-driven fracture in an elastic medium. *ASME J. Appl. Mech.*, 67(1):183–192, 2000.
- [47] A. M. Rubin. Tensile fracture of rock at high confining pressure: Implications for dike propagation. *J. Geophys. Res.*, 98(B9):15,919–15,935, 1993.
- [48] E. Detournay and D. Garagash. The tip region of a fluid-driven fracture in a permeable elastic solid. *J. Fluid Mech.*, 494:1–32, 2003.
- [49] D. A. Spence and P. W. Sharp. Self-similar solution for elastohydrodynamic cavity flow. *Proc. Roy. Soc. London, Ser. A(400)*:289–313, 1985.
- [50] E. Detournay. Mechanics of hydraulic fractures. *Annu. Rev. Fluid Mech.*, 48:311–39, 2016.
- [51] Gudmundsson A. Form and dimensionso f dykes in easterniceland. *Tectonophysics*, 95:295–307, 1983.
- [52] C.B. Raleigh, J.H. Healy, and J.D. Bredehoeft. An experiment in earthquake control at rangely, colorado. *Science*, 191:1230–1237, 1976.
- [53] A. Ziv and A. M. Rubin. Stability of dike intrusion along preexisting fractures. *J. Geo. Res.*, 105(B3):5947–5961, March 2000.
- [54] X. Zhang, R. G. Jeffrey, and E. M. Llanos. On plane-strain fluid-driven shear fracture propagation in elastic solids. *Geophys. J. Int.*, 163:419–430, 2005.
- [55] F. Cappa and J. Rutqvist. Impact of co2 geological sequestration on the nucleation of earthquakes. *Geophys. Res. Lett.*, 38(L17313).

- [56] M. W. McClure and R. N. Horne. Investigation of injection-induced seismicity using a coupled fluid flow and rate/state friction model. *Geophys.*, 76(6):WC181–WC198, 2011.
- [57] V. S. Gischig. Rupture propagation behavior and the largest possible earthquake induced by fluid injection into deep reservoirs. *Geophys. Res. Lett.*, 42:7420–7428, 2015.
- [58] D. Dempsey and J. Suskale. Collective properties of injection-induced earthquake sequences: 1. Model description and directivity bias. *J. Geophys. Res.*, 121:3609–3637, 2016.
- [59] D. I. Garagash, L. N. Germanovich, L. C. Murdoch, S. Martel, Z. Reches, D. Ellsworth, T. C. Onstott, and S. D. Glaser. A thermal technique of fault nucleation, growth, and slip. *EOS Trans. AGU (Fall Meeting Suppl.)*, 90(52):H23E–0995, 2009.
- [60] L. N. Germanovich, L. C. Murdoch, D. I. Garagash, Z. Reches, S. J. Martel, D. Gwaba, D. Ellsworth, R. P. Lowell, and T. C. Onstott. A controllable earthquake rupture experiment on the homestake fault. *EOS Trans. AGU (Fall Meeting Suppl.)*, San Francisco, pages H13F–1045, 13-17 Dec 2010.
- [61] L. N. Germanovich, L. C. Murdoch, D. I. Garagash, Z. Reches, S. J. Martel, D. Gwaba, D. Ellsworth, and T. C. Onstott. Earthquake rupture experiment on the homestake fault. *Engineering Research and Innovation Conference, Natl. Sci. Found., Atlanta*, 2011.
- [62] R. C. Viesca and R. Rice. Nucleation of slip-weakening rupture instability in landslides by localized increase of pore pressure. *JOURNAL OF GEOPHYSICAL RESEARCH*, 117, 2012.
- [63] Y. Guglielmi, F. Cappa, J. Avouac, P. Henry, and D. Ellsworth. Seismicity triggered by fluid injection-induced aseismic slip. *Science*, 348:1224–1226, June 2015.
- [64] D. I. Garagash and L. N. Germanovich. Nucleation and arrest of dynamic slip on a pressurized fault. *J. Geophys. Res.*, 117 B(10), 2012.
- [65] G.I. Barenblatt. The formation of equilibrium cracks during brittle fracture: General ideas and hypotheses: Axially-symmetric cracks. *Prikl. Mat. Mech.*, 23:434–444, 1959.
- [66] Y. Ida. Cohesive force across the tip of a longitudinal-shear crack and griffith’s specific surface energy. *J. Geophys. Res.*, 77:3796–3805, 1972.
- [67] A. C. Palmer and J. R. Rice. The growth of slip surfaces in the progressive failure of over-consolidated clay. *Proc. Roy. Soc. London*, 433:469–477, 1973.

- [68] J.H. Dieterich. Modeling of rock friction 1. experimental results and constitutive equations. *J. Geophys. Res.*, 84(15):2161–2168, 1979.
- [69] C. Marone. Laboratory-derived friction laws and their application to seismic faulting. *Annu. Rev. Earth Planet. Sci.*, 26:643–696, 1998.
- [70] J.P. Ampuero and A. M. Rubin. Earthquake nucleation on rate and state faults: Aging and slip laws. *J. Geophys. Res.*, 113(B01302), 2008.
- [71] A. M. Rubin and J.P. Ampuero. Earthquake nucleation on (aging) rate and state faults. *J. Geophys. Res.*, 110(B11312), 2005.
- [72] J. H. Dieterich. Earthquake nucleation on faults with rate- and statedependent friction. *Tectonophysics*, 211(115-134), 1992.
- [73] K. Uenishi and J. R. Rice. Universal nucleation length for slip-weakening rupture instability under nonuniform fault loading. *J. Geophys. Res.*, 108(B1):2042, 2003.
- [74] D. J. Andrews. Rupture propagation with finite stress in antiplane strain. *J. Geophys. Res.*, 81(20):3575–3582, 1976.
- [75] T. L. Blanton. Propagation of hydraulically and dynamically induced fractures in naturally fractured reservoirs. *SPE UGTS, Louisville, SPE Paper No. 152618.*, 1986.
- [76] N. R. Warpinski and L. W. Teufel. 15, 737e751. influence of geologic discontinuities on hydraulic fracture propagation. *J. Pet. Tech.*, pages 209–220, 1987.
- [77] C. E. Renshaw and D. D. Pollard. An experimentally verified criterion for propagation across unbounded frictional interfaces in brittle, linear elastic materials. *Int. J. Rock Mech. Min. Sci. and Geomech. Abstr.*, 32:237–249, 1995.
- [78] AA. Daneshy. Hydraulic fracture propagation in the presence of planes of weakness. *SPE European Spring Meeting; Amsterdam, Netherlands*, 1974.
- [79] T. L. Blanton. An experimental study of interaction between hydraulically induced and preexisting fractures. *SPE 10847, presented at the SPE/DOE Unconventional Gas Recovery Symposium, Pittsburgh, PA*, May 16 - 18 1982.
- [80] M. Thiercelin and E. Makkhyu. Stress field in the vicinity of a natural fault activated by the propagation of an induced hydraulic fracture. *Proceedings of the 1st Canada-US Rock Mechanics Symposium - Rock Mechanics Meeting Society's Challenges and Demands, 2*, pages 1617–1624, 2007.
- [81] D.A. Chuprakov, A.V. Akulich, E. Siebrits, and M.Thiercelin. Hydraulic fracture propagation in a naturally fractured reservoir. *SPE 128715, presented at the SPE Oil and Gas India Conference and Exhibition held in Mumbai, India*, 20-22 January 2010.

- [82] X. Zhang and R.G. Jeffrey. The role of friction and secondary flaws on deflection and re-initiation of hydraulic fractures at orthogonal pre-existing fractures. *Geophys. J. Int.*, 166 (3):1454–1465, 2006.
- [83] X. Zhang, R. G. Jeffrey, and M. Thiercelin. Mechanics of fluid-driven fracture growth in naturally fractured reservoirs with simple network geometries. *J. Geo. Res.*, 114, 2009.
- [84] H. Gu and X. Weng. Criterion for fracturers crossing frictional interfaces at non-orthogonal angles. *ARMA 10-198, presented at the 44th US Rock mechanics Symposium and 5th U.S.-Canada Rock mechanics Symposium, Salt Lake City, UT*, 2010.
- [85] E. Detournay and A.H.-D. Cheng. “fundamentals of poroelasticity”. , *Chapter 5 in Comprehensive Rock Engineering: Principles, Practice and Projects, Vol. II, Analysis and Design Method*, ed. C. Fairhurst, Pergamon Press, pages 113–171, 1993.
- [86] M.A. Biot. General theory of three-dimensional consolidation. *J. Appl. Phys.*, 12:155–164, 1941.
- [87] J. R. Rice and M.P. Cleary. Some basic stress-diffusion solutions for fluid saturated elastic porous media with compressible constituents. *Rev. Geophys. Space Phys.*, 14:227–241, 1976.
- [88] S. A. Shapiro and Dinske C. Fluid-induced seismicity: Pressure diffusion and hydraulic fracturing. *Geophys. Prospect.*, 57:301–310, 2009.
- [89] P. Segall and J. R. Rice. Dilatancy, compaction, and slip instability of a fluid-infiltrated fault. *J. Geophys. Res.*, 100:22,155–22,171, 1995.
- [90] N. H. Sleep and M. Blanpied. Creep, compaction and the weak reology of major faults. *Nature*, 359, 1992.
- [91] D. I. Garagash and J. W. Rudnicki. Shear heating of a fluid-saturated slip-weakening dilatant fault zone 1. Limiting regimes. Art. No 2121. *J. Geophys. Res.*, 108(B2):1–19, 2003.
- [92] M. D. Zoback and J. D. Byerlee. The effect of microcrack dilatancy on the permeability of westerly granite. *J. Geophys. Res.*, 80:752–755, 1975.
- [93] N. Barton, S. Bandis, and K. Bakhtar. Strength, deformation and conductivity coupling of rock joints. *Int. J. Rock Mech. Min. Sci.*, 22(3):121–140, 1985.
- [94] B. A. Bilby and J. D. Eshelby. Dislocations and the theory of fracture. In H. Liebowitz, editor, *Fracture, an Advanced Treatise*, volume I, chapter 2, pages 99–182. Academic Press, New York NY, 1968.

- [95] J. R. Rice. Mathematical analysis in the mechanics of fracture. In H. Liebowitz, editor, *Fracture, an Advanced Treatise*, volume II, chapter 3, pages 191–311. Academic Press, New York NY, 1968.
- [96] J. W. Rudnicki and J. R. Rice. Effective normal stress alteration due to pore pressure changes induced by dynamic slip propagation on a plane between dissimilar materials. *J. Geophys. Res.*, 111(B):10308, 2006.
- [97] E. Detournay. Propagation regimes of fluid-driven fractures in impermeable rocks. *Int. J. Geomechanics*, 4(1):1–11, 2004.
- [98] M. Campillo and I. R. Ionescu. Initiation of antiplane shear instability under slip dependent friction. *J. Geophys. Res.*, 102:20363–20371, 1997.
- [99] J.-P. Ampuero and Y. Ben-Zion. Cracks, pulses and macroscopic asymmetry of dynamic rupture on a bimaterial interface with velocity-weakening friction. *Geophys. J. Int.*, 173:674–692, 2008.
- [100] J. R. Rice. The mechanics of earthquake rupture. In A.M. Dziewonski and E. Boschi, editors, *Physics of the Earth’s Interior, Proc. Int. Sch. Phys. Enrico Fermi, 78*, pages 555–649, North-Holland, Amsterdam, 1980.
- [101] F. Rummel, H. J. Alheid, and C. Frohn. Dilatancy and fracture-induced velocity changes in rock and their relation to frictional sliding. *Pure Appl. Geophys.*, 116:743–764, 1978.
- [102] N. Brantut and R. C. Viesca. Earthquake nucleation in intact or healed rocks. *J. Geophys. Res.*, 120:191–209, 2015.
- [103] S. L. Karner, C. Marone, and B. Evans. Laboratory study of fault healing and lithification in simulated fault gouge under hydrothermal conditions. *Tectonophysics*, pages 41–55, 1997.
- [104] F. M. Chester, J. P. Evans, and R. L. Biegel. Internal structure and weakening mechanisms of the San Andreas fault. *J. Geophys. Res.*, 98(B1):771–786, 1993.
- [105] M. Zoback, S. Hickman, W. Ellsworth, and the SAFOD Science Team. Scientific drilling into the San Andreas fault zone - An overview of SAFOD’s first five years. *Scientific Drilling*, 11:14–28, 2011.
- [106] A.-M. Boullier, E.-C. Yeh, S. Boutareaud, S.-R. Song, and C.-H. Tsai. Microscale anatomy of the 1999 Chi-Chi earthquake fault zone. *Geochem. Geophys. Geosystems*, 10(3):Q03016, 2009.
- [107] F. M. Chester and J. S. Chester. Ultracataclasite structure and friction processes of the Punchbowl fault, San Andreas system, California. *Tectonophysics*, 295:199–221, 1998.

- [108] J. D. Platt, J. W. Rudnicki, and J. R. Rice. Stability and localization of rapid shear in fluid-saturated fault gouge: 2. Localized zone width and strength evolution. *J. Geophys. Res.*, 119:4334–4359, 2014.
- [109] C. Marone and B. Kilgore. Scaling of the critical slip distance for seismic faulting with shear strain in fault zones. *Nature*, 362:618–621, 1993.
- [110] M. Guatteri and P. Spudich. What can strong motion data tell us about slip-weakening fault-friction laws? *Bull. Seism. Soc. Am.*, 90:98–116, 2000.
- [111] P. M. Mai and G. C. Beroza. A spatial random field model to characterize complexity in earthquake slip. *J. Geophys. Res.*, 107(B11):2308, 2002.
- [112] M. D. Zoback, C. A. Barton, M. Brudy, D. A. Castillo, T. Finkbeiner, B. R. Grollmund, D. B. Moos, P. Peska, C. D. Ward, and D. J. Wiprut. Determination of stress orientation and magnitude in deep wells. *Int. J. Rock Mech. Min. Sci.*, 40:1049–1076, 2003.
- [113] S. Hickman and M. Zoback. Stress orientations and magnitudes in the SAFOD pilot hole. *Geophys. Res. Lett.*, 31:L15S12, 2004.
- [114] J.-P. Ampuero, J. Ripperger, and P. M. Mai. Properties of dynamic earthquake ruptures with heterogeneous stress drop. In A. McGarr, R. Abercrombie, and H. Kanamori, editors, *Earthquakes: Radiated Energy and the Physics of Faulting*, volume 170 of *Geophysical Monograph Series*. American Geophysical Union, 2006.
- [115] J. Ripperger, J.-P. Ampuero, P. M. Mai, and D. Giardini. Earthquake source characteristics from dynamic rupture with constrained stochastic fault stress. *J. Geophys. Res.*, 112:B04311, 2007.
- [116] M.G. Mack and R. Warpinski. Mechanics of hydraulic fracturing. In M.J. Economides and K.G. Nolte, editors, *Reservoir Stimulation*, chapter 6. John Wiley and Sons, Chichester UK, 3rd edition, 2000.
- [117] A. N. B. Poliakov, R. Dmowska, and J. R. Rice. Dynamic shear rupture interactions with fault bends and off-axis secondary faulting. *J. Geo. Res.*, 107(B11, 2295), 2002.
- [118] M.S. Paterson and Teng fong Wong. Experimental rock deformation - the brittle field. *Springer Science Business Media, Science*, page 347, 2005.
- [119] M. D. Zoback, R. Apel, J. Baumgartner, M. Brudy, R. Emmermann, B. Engeser, K. Fuchs, W. Kessels, H. RischmullerI, F. Rummel, and L. Vernic. Upper-crustal strength inferred from stress measurements to 6 km depth in the ktb borehole. *Nature*, 365:633 – 635, 1993.

- [120] D. J. Bishop D. A. Castillo and M. de Ruig. Fault seal integrity in the timor sea area: Prediction of trap failure using well-constrained stress tensors and fault surfaces interpreted from 3d seismic. Barossa Valley, South Australia, Dec 1-5 2002.
- [121] D. Castillo, D. J. Bishop, I. Donaldson, D. Kuek, M. J. de Ruig, M. Trupp, M. W. Shuster, Australian Petroleum Production, Exploration Association (APPEA), and Petroleum Exploration Society of Australia. Trap integrity in the laminaria high-nancar trough region, timor sea: Prediction of fault seal failure using well constrained stress tensors and fault surfaces interpreted from 3d seismic. *APPEA*, 40(151-173), 2000.
- [122] Mark D. Zoback David Wiprut. Fault reactivation and fluid flow along a previously dormant normal fault in the northern north sea. *Geology*, 28:595–598, 2000.
- [123] M. D. Zoback. *Reservoir Geomechanics*. May 2010.
- [124] J. Byerlee. Friction of rocks. *Pageoph, Birkhfiuser Verlag, Basel*, 116, 1978.
- [125] A.F. Gangi. Variation of whole and fractured porous rock permeability with confining pressure. *Int. J. Rock Mechanics and Mining Sciences*, 15:249–257, 1978.
- [126] J.B. Walsh. Effect of pore pressure and confining pressure on fracture permeability. *Int. J. Rock Mech. Min. Sci.*, 18:429–435, 1981.
- [127] S. C. Bandis, A. C. Lumsden, and N. R. Barton. Fundamentals of rock joint deformation. *Int. J. Rock Mech. Min. Sci.*, 20(6):249–268, 1983.
- [128] R. G. Jeffrey, X. Zhang, and M. Thiercelin. Hydraulic fracture offsetting in naturally fractured reservoirs: Quantifying a long-recognized process. In *SPE Hydraulic Fracturing Technology Conference*, pages SPE–119351–MS, The Woodlands, Texas, January 2009.
- [129] H. Gu, X. Weng adn J. Lund, M. Mack, U. Ganguly, and R. Suarez-Rivera. Hydraulic fracture crossing natural fracture at nonorthogonal angles: A criterion and its validation. In *SPE Hydraulic Fracturing Technology Conference*, pages SPE–139984, The Woodlands, Texas, January 2011.
- [130] B. J. Hulse, B. Cornette, and D. Pratt. Surface microseismic mapping reveals details of the Marcellus shale. In *SPE Eastern Regional Meeting*, page SPE 138806, Morgantown, WV, 2010.
- [131] S. L. Wolhart, T. A. Harting, J. E. Dahlem, T. J. Young, M. J. Mayerhofer, and E. P. Lolon. Hydraulic fracture diagnostics used to optimize development in the Jonah field. In *SPE Annual Technical Conference*, page SPE 102528, San Antonio, Texas, 2006.

- [132] A. H. Kohli and M. D. Zoback. Frictional properties of shale reservoir rocks. *J. Geophys. Res.*, 118:5109–5125, 2013.
- [133] J.H. Michell. On the direct determination of stress in an elastic solid, with application to the theory of plates. *Proceedings of the London Mathematical Society*, 31:100–124, 1899.
- [134] J.R. Barber. *Elasticity*. Kluwer Academic Publishers, Dordrecht, 1992.
- [135] D.A. Hills, P.A. Kelly, D.N. Dai, and A.M. Korsunsky. *Solution of Crack Problems. The Distributed Dislocation Technique*, volume 44 of *Solid Mechanics and its Applications*. Kluwer Academic Publ., Dordrecht, 1996.
- [136] M. Abramowitz and I.A. Stegun, editors. *Handbook of Mathematical Functions with Formulas, Graphs, and Mathematical Tables*. Dover Publications Inc., New York NY, 1972.
- [137] H. Tada, P. C. Paris, and G.R. Irwin. *The Stress Analysis of Cracks Handbook*. ASME Press, New York, 3rd edition, 2000.
- [138] F. Erdogan and G.D. Gupta. On the numerical solution of singular integral equations. *Quart. Appl. Math.*, 30:525–534, 1972.
- [139] S. Krenk. On the use of the interpolation polynomial for solutions of singular integral equations. *Quart. Appl. Math.*, 32:479–484, 1975.

APPENDIX A: DERIVATION OF GOVERNING EQUATIONS

In this Appendix, we present the derivation of the partial governing equations for the solid and fluid. We then proceed with providing the basic solutions for the equations that were used in our study, considering simplifying assumptions.

A.1 Equilibrium equations

An elastic body is in equilibrium if each point in the solid is stationary. In order to derive the condition for stresses σ_{ij} when the elastic body is at equilibrium, consider an infinitely small differential element with dimensions dx , dy , dz as shown in Figure A.1.

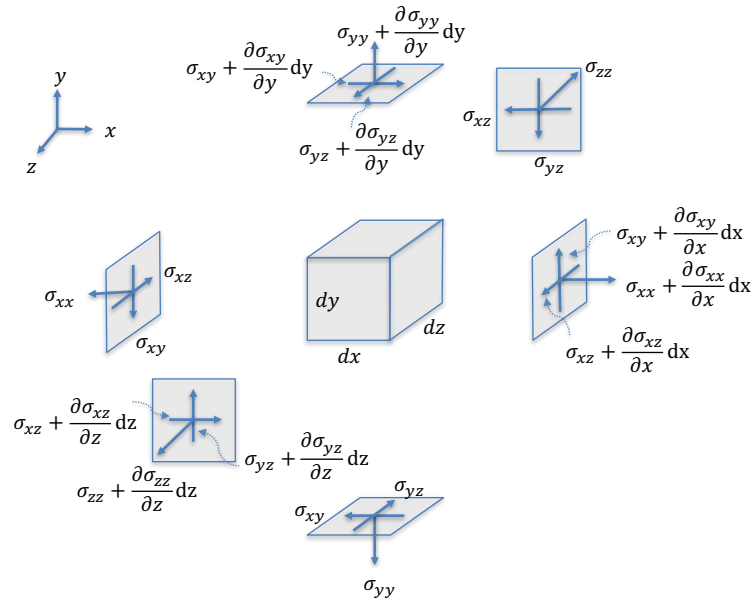


Figure A.1: An infinitely small differential element in equilibrium

Consider the element is loaded along its sides by stresses that vary in x , y , and z , where the variation in each stress term is considered using a first order Taylor series

expansion, and suppose that there are body forces P_x , P_y and P_z per unit volume.

Summing forces in the x direction gives:

$$\left[\sigma_{xx} + \left(\frac{\partial \sigma_{xx}}{\partial x} \right) dx \right] dydz - \sigma_{xx} dydz + \left[\sigma_{xy} + \left(\frac{\partial \sigma_{xy}}{\partial y} \right) dy \right] dx dz - \sigma_{xy} dx dz + \quad (\text{A.1})$$

$$\left[\sigma_{xz} + \left(\frac{\partial \sigma_{xz}}{\partial z} \right) dz \right] dx dy - \sigma_{xz} dx dy + P_x dx dy dz = 0$$

which in terms of force per unit volume ($dx \times dy \times dz$) simplifies to the following:

$$\frac{\partial \sigma_{xx}}{\partial x} + \frac{\partial \sigma_{xy}}{\partial y} + \frac{\partial \sigma_{xz}}{\partial z} + P_x = 0. \quad (\text{A.2})$$

Similarly, writing the equations of equilibrium for the stresses in the y and z directions gives

$$\frac{\partial \sigma_{yy}}{\partial y} + \frac{\partial \sigma_{xy}}{\partial x} + \frac{\partial \sigma_{yz}}{\partial z} + P_y = 0 \quad (\text{A.3})$$

$$\frac{\partial \sigma_{zz}}{\partial z} + \frac{\partial \sigma_{yz}}{\partial y} + \frac{\partial \sigma_{xz}}{\partial x} + P_z = 0.$$

And in index notation (for a three-dimensional element) we have:

$$\frac{\partial \sigma_{ij}}{\partial x_i} + P_i = 0 \quad (\text{A.4})$$

These differential equations of equilibrium hold everywhere in a body that is in static equilibrium. It should be noted that the equilibrium of moments acting on the element requires a symmetric stress tensor: $\sigma_{ij} = \sigma_{ji}$.

Strain compatibility

The equations of compatibility, or the relations between the strains, can be obtained directly from the definition of the strain tensor

$$\varepsilon_{ij} = \frac{1}{2} \left(\frac{\partial u_i}{\partial x_j} + \frac{\partial u_j}{\partial x_i} \right) \quad (\text{A.5})$$

where u_x, u_y, u_z are the components of displacement field in the strain-displacement relations. The above definition relates six components of the strain tensor (in the three dimensional case) to the three components of the displacement field that implies that the strains are not independent. The first equation of compatibility can be obtained by calculating

$$\frac{\partial^2 \varepsilon_{xx}}{\partial y^2} = \frac{\partial^3 u_x}{\partial x \partial y^2}, \quad \frac{\partial^2 \varepsilon_{yy}}{\partial x^2} = \frac{\partial^3 u_y}{\partial x^2 \partial y}, \quad \frac{\partial^2 \varepsilon_{xy}}{\partial xy} = \frac{1}{2} \left(\frac{\partial^3 u_x}{\partial x \partial y^2} + \frac{\partial^3 u_y}{\partial x^2 \partial y} \right)$$

and hence it follows that

$$\frac{\partial^2 \varepsilon_{xx}}{\partial y^2} - 2 \frac{\partial^2 \varepsilon_{xy}}{\partial xy} + \frac{\partial^2 \varepsilon_{yy}}{\partial x^2} = 0. \quad (\text{A.6})$$

Stress-strain constitutive laws

According to the linear elasticity the material obeys Hooke's law which implies a linear relation between stress and strain. Stress-strain relations are expressed in two-dimensional problems as:

$$\varepsilon_{xx} = \left(\frac{k+1}{8G} \right) \sigma_{xx} - \left(\frac{3-k}{8G} \right) \sigma_{yy}; \quad \varepsilon_{yy} = \left(\frac{k+1}{8G} \right) \sigma_{yy} - \left(\frac{3-k}{8G} \right) \sigma_{xx}, \quad \varepsilon_{xy} = \frac{\sigma_{xy}}{2G} \quad (\text{A.7})$$

where the modulus of rigidity $G = E/2(1 + \nu)$, E is elasticity modulus and k is Kolosov's constant, defined as $k = (\frac{3-\nu}{1+\nu})$ for the plane stress state that assumes the traction on the plane is zero and $k = (3 - 4\nu)$ for the plane strain state that assumes the strain normal to the plane is zero $\varepsilon_{zz} = \varepsilon_{xz} = \varepsilon_{yz} = 0$ and $u_x = u_x(x, y)$, $u_y = u_y(x, y)$.

A.1.1 Stress function formulation

“Airy Stress Function” method is a technique for solving two-dimensional static linear elasticity problems. The technique is based on the idea of representing the stress fields by a scalar potential that satisfy the equilibrium equations. In the absence of body forces, the two-dimensional equilibrium equations reduce to

$$\frac{\partial \sigma_{xx}}{\partial x} + \frac{\partial \sigma_{xy}}{\partial y} = 0, \quad \frac{\partial \sigma_{yy}}{\partial y} + \frac{\partial \sigma_{xy}}{\partial x} = 0. \quad (\text{A.8})$$

Propose that a scalar function, ϕ , exists that is related to the stress components by the following relationships

$$\sigma_{xx} = \frac{\partial^2 \phi}{\partial y^2}, \quad \sigma_{xy} = -\frac{\partial^2 \phi}{\partial x \partial y}, \quad \sigma_{yy} = \frac{\partial^2 \phi}{\partial x^2} \quad (\text{A.9})$$

so that it will satisfy the equilibrium equations automatically. The Airy stress function must also satisfy the compatibility equation. Expressing the two dimensional compatibility equation (A.6) by using the stress-strain relations (A.7) and substituting for the stress components from the above gives

$$\frac{\partial^4 \phi}{\partial x^4} + 2\frac{\partial^4 \phi}{\partial x^2 \partial y^2} + \frac{\partial^4 \phi}{\partial y^4} = \nabla^4 \phi = 0. \quad (\text{A.10})$$

This relation is called the biharmonic partial differential equation that is the governing equation for the Airy stress function in two-dimensional elasticity problems.

In polar coordinates, the biharmonic equation is given by

$$\nabla^4 \phi = \left(\frac{1}{r} \frac{\partial}{\partial r} \left(r \frac{\partial}{\partial r} \right) + \frac{1}{r^2} \frac{\partial^2}{\partial \theta^2} \right)^2 \phi = 0 \quad (\text{A.11})$$

where the relationships for the stress components (A.9) are

$$\sigma_{rr} = \frac{1}{r} \frac{\partial \phi}{\partial r} + \frac{1}{r^2} \frac{\partial^2 \phi}{\partial \theta^2}, \quad \sigma_{\theta\theta} = \frac{\partial^2 \phi}{\partial r^2}, \quad \sigma_{r\theta} = -\frac{\partial}{\partial r} \left(\frac{1}{r} \frac{\partial \phi}{\partial \theta} \right). \quad (\text{A.12})$$

Michell [133] obtained a general solution to equation (A.11) in the form

$$\begin{aligned} \phi = & A_{01}r^2 + A_{02}r^2 \ln r + A_{03} \ln r + A_{04}\theta \\ & + (A_{11}r^3 + A_{12}r \ln r + A_{14}r^{-1}) \cos \theta + A_{13}r\theta \sin \theta \\ & + (B_{11}r^3 + B_{12}r \ln r + B_{14}r^{-1}) \sin \theta + B_{13}r\theta \cos \theta \\ & + \sum_{n=2}^{\infty} (A_{n1}r^{n+2} + A_{n2}r^{-n+2} + A_{n3}r^n + A_{n4}r^{-n}) \cos n\theta \\ & + \sum_{n=2}^{\infty} (B_{n1}r^{n+2} + B_{n2}r^{-n+2} + B_{n3}r^n + B_{n4}r^{-n}) \sin n\theta \end{aligned} \quad (\text{A.13})$$

where the coefficients A_{ij} , B_{ij} are arbitrary constants for the Airy stress components in the Fourier series. Each term in the series must also satisfy the biharmonic equation. For example, it can be easily verified for the term $\phi = r \ln r \cos \theta$ by expanding the biharmonic equation (A.11) into

$$\nabla^4 \phi = \phi_{rrrr} + \frac{2}{r^2} \phi_{rr\theta\theta} + \frac{1}{r^4} \phi_{\theta\theta\theta\theta} + \frac{2}{r} \phi_{rrr} - \frac{2}{r^3} \phi_{r\theta\theta} - \frac{1}{r^2} \phi_{rr} + \frac{4}{r^4} \phi_{\theta\theta} + \frac{1}{r^3} \phi_r = 0. \quad (\text{A.14})$$

The corresponding stress components are obtained by substituting the expression (A.13) into formulas (A.12). Moreover, If the stress components are known for a specific problem, Hook's law is used to find the strains and the displacement components will be obtained by the integration of the latter.

A.1.2 Dislocation solution

Stress function technique may be employed to evaluate the stress and displacement fields emerging in the dislocated bodies. If we make a cut along positive x axis in an infinite continuous body and pull the material apart to open up a gap of constant thickness b_y , this will leave the continuous body in a state of residual stress. The resulting climb dislocation solution is found by choosing the appropriate stress function (for the stress field that is proportional to r^{-1} , symmetric about $\theta = 0$ and has no net force at the origin) [134]:

$$\phi = A_{12} r \ln r \cos \theta \quad (\text{A.15})$$

for which the stress components are obtained using formulas (A.12) as

$$\begin{aligned} \sigma_{rr} &= \frac{A_{12} \cos \theta}{r} \\ \sigma_{r\theta} &= \frac{A_{12} \sin \theta}{r} \\ \sigma_{\theta\theta} &= \frac{A_{12} \cos \theta}{r} \end{aligned} \quad (\text{A.16})$$

The strain components are given by the two-dimensional stress-strain relations

$$\begin{aligned} \varepsilon_{rr} &= \left(\frac{k+1}{8G} \right) \sigma_{rr} - \left(\frac{3-k}{8G} \right) \sigma_{\theta\theta} = \frac{(k-1)A_{12} \cos \theta}{4G r} \\ \varepsilon_{\theta\theta} &= \left(\frac{k+1}{8G} \right) \sigma_{\theta\theta} - \left(\frac{3-k}{8G} \right) \sigma_{rr} = \frac{(k-1)A_{12} \cos \theta}{4G r} \\ \varepsilon_{r\theta} &= \frac{\sigma_{r\theta}}{2G} = \frac{A_{12} \sin \theta}{2G r} \end{aligned} \quad (\text{A.17})$$

The displacement field can be found by integration of the strain components. The strain-displacement relationships in polar coordinates are

$$\varepsilon_{rr} = \frac{\partial u_r}{\partial r}, \quad \varepsilon_{\theta\theta} = \frac{1}{r} \frac{\partial u_\theta}{\partial \theta} + \frac{u_r}{r}, \quad \varepsilon_{r\theta} = \frac{1}{2} \left(\frac{1}{r} \frac{\partial u_r}{\partial \theta} + \frac{\partial u_\theta}{\partial r} - \frac{u_\theta}{r} \right) \quad (\text{A.18})$$

We now integrate the first strain component with respect to r to give

$$u_r = \frac{(k-1)A_{12}}{4G} \cos \theta \ln r + f(\theta) \quad (\text{A.19})$$

where $f(\theta)$ is an arbitrary function. We then obtain $\partial u_\theta / \partial \theta = r\varepsilon_{\theta\theta} - u_r$ by substituting (A.17) for $\varepsilon_{\theta\theta}$ and substituting (A.19) for u_r as

$$\frac{\partial u_\theta}{\partial \theta} = \frac{(k-1)A_{12}}{4G} \cos \theta (1 - \ln r) - f(\theta) \quad (\text{A.20})$$

which can be integrated with respect to θ to give

$$u_\theta = \frac{(k-1)A_{12}}{4G} \sin \theta (1 - \ln r) - F(\theta) + g(r) \quad (\text{A.21})$$

where $F(\theta) = \int f(\theta) d\theta$, and $g(r)$ is an arbitrary function of r . The two functions $f(\theta)$ and $g(r)$ can be found with using the definition of shear strain in (A.18). Substituting for u_r and u_θ from (A.19, A.21), performing differentiations and rearranging the terms, we obtain

$$\left(F(\theta) + f'(\theta) - g(r) + rg'(r) \right) = \frac{(k+1)A_{12}}{2G} \sin \theta. \quad (\text{A.22})$$

The right-hand side of (A.22) is a function of θ only and hence $g(r) = 0$. Solving the resulting ordinary differential equation for $f(\theta)$, we find $f(\theta) = \frac{A_{12}}{4G} ((k+1)\theta \sin \theta - \cos \theta)$.

The displacement field components are then given by

$$\begin{aligned} u_r &= \frac{A_{12}}{4G} [(k+1)\theta \sin \theta - \cos \theta + (k-1) \ln r \cos \theta] \\ u_\theta &= \frac{A_{12}}{4G} [(k+1)\theta \cos \theta - \sin \theta - (k-1) \ln r \sin \theta] \end{aligned} \quad (\text{A.23})$$

The strength of the climb dislocation, or thickness of the gap, is equal to the discontinuity in the displacement u_θ on $\theta = 0, 2\pi$ along the cut line

$$b_y = u_\theta(0) - u_\theta(2\pi) = -\frac{\pi(k+1)}{2G}A_{12} \quad (\text{A.24})$$

that gives the unknown A_{12} . The corresponding Cartesian stress fields along $y = 0$, (i.e., $\theta = 0, \pi$), are

$$\begin{aligned} \sigma_{yy} = \sigma_{xx} &= -\frac{2Gb_y}{\pi(k+1)x} \\ \sigma_{yx} &= 0 \end{aligned} \quad (\text{A.25})$$

A glide dislocation solution is obtained by the choice of stress function

$$\phi = \frac{2Gb_x r \ln r \sin \theta}{\pi(k+1)} \quad (\text{A.26})$$

for a discontinuity in the displacement component u_r , where two surfaces of the cut experience a relative tangential displacement, $b_x = u_r(0) - u_r(2\pi)$. The resulting stress fields due to the glide dislocation are

$$\begin{aligned} \sigma_{rr} = \sigma_{\theta\theta} &= \frac{2Gb_x \sin \theta}{\pi(k+1)r} \\ \sigma_{r\theta} &= -\frac{2Gb_x \cos \theta}{\pi(k+1)r} \end{aligned} \quad (\text{A.27})$$

and Cartesian stress fields along $y = 0$ are given by

$$\begin{aligned} \sigma_{yy} = \sigma_{xx} &= 0 \\ \sigma_{yx} &= -\frac{2Gb_x}{\pi(k+1)x} \end{aligned} \quad (\text{A.28})$$

A.1.3 Stress field due to a planar crack

Stress fields due to a single ‘‘edge’’ dislocation with resolved Burger vector components shear b_x and opening b_y may be found from corresponding Airy stress functions and

are given by:

$$\begin{aligned}
\sigma_{xx}(x, y) &= \frac{E'}{4\pi}[b_x G_{xxx} + b_y G_{yxx}] \\
\sigma_{yy}(x, y) &= \frac{E'}{4\pi}[b_x G_{xyy} + b_y G_{yyy}] \\
\sigma_{xy}(x, y) &= \frac{E'}{4\pi}[b_x G_{xxy} + b_y G_{yxy}]
\end{aligned} \tag{A.29}$$

where for plane strain $E' = E/(1 - \nu^2)$, $k = 3 - 4\nu$ and noting that $G = E/2(1 + \nu)$. The influence functions G_{ijk} related to specific stress components and dislocation orientations differ for various geometries. Stress σ_{ij} is second rank tensor while dislocation vector is first rank tensor, therefore the influence functions G_{ijk} must also be a tensor (of 3rd rank). The influence functions for an *infinite medium* are expressed by [135]:

$$\begin{aligned}
G_{xxx}(x, y; \xi, \eta) &= y_1(-3x_1^2 - y_1^2)/r_1^4 \\
G_{xyy}(x, y; \xi, \eta) &= y_1(x_1^2 - y_1^2)/r_1^4 \\
G_{xxy}(x, y; \xi, \eta) &= x_1(x_1^2 - y_1^2)/r_1^4 \\
G_{yxx}(x, y; \xi, \eta) &= x_1(x_1^2 - y_1^2)/r_1^4 \\
G_{yyy}(x, y; \xi, \eta) &= x_1(x_1^2 + 3y_1^2)/r_1^4 \\
G_{yxy}(x, y; \xi, \eta) &= y_1(x_1^2 - y_1^2)/r_1^4
\end{aligned} \tag{A.30}$$

where

$$x_1 = x - \xi, y_1 = y - \eta, r_1^2 = x_1^2 + y_1^2 \tag{A.31}$$

and for dislocations along global coordinate x axis $(\xi, 0)$, $y_1 = y$.

Stresses induced in the material due to an open crack (Figure 2.1) are obtained by accumulations of opening Burger vectors (as dislocation densities $\delta b_y = (dw/ds)\delta s$) using (A.29-A.30)

$$\begin{aligned}
\sigma_{xx}(x, y) &= \frac{E'}{4\pi} \int_{-\ell}^{\ell} \frac{dw}{d\xi} \frac{x_1(x_1^2 - y_1^2)}{r_1^4} d\xi \\
\sigma_{yy}(x, y) &= \frac{E'}{4\pi} \int_{-\ell}^{\ell} \frac{dw}{d\xi} \frac{x_1(x_1^2 + 3y_1^2)}{r_1^4} d\xi \\
\sigma_{xy}(x, y) &= \frac{E'}{4\pi} \int_{-\ell}^{\ell} \frac{dw}{d\xi} \frac{y_1(x_1^2 - y_1^2)}{r_1^4} d\xi
\end{aligned} \tag{A.32}$$

Note that, for example, along the crack plane ($y = 0$) these relations simplify to $\sigma_{xx}(x, 0) = \sigma_{yy}(x, 0) = (E'/4\pi) \int_{-\ell}^{\ell} \frac{dw}{d\xi} \frac{d\xi}{x-\xi}$ and $\sigma_{xy}(x, 0) = 0$.

A.2 Mass conservation and continuity equation

The law of mass conservation requires that the time rate of change of mass in an element must be balanced by the flow of fluid out of the element

$$\frac{\partial}{\partial t} \int_{CV} \rho dV + \int_{CS} \rho v \cdot n dS = 0 \tag{A.33}$$

where CV is control volume, CS is control surface, ρ is density, $v = (v_x, v_y, v_z)$ is the fluid velocity vector and n is outward normal unit vector (perpendicular to surface). In addition, the integral of outward component of a vector f over the control surface CS is related to the divergence of the vector over the control volume CV by Divergence theorem: $\int_{CS} f \cdot n dS = \int_{CV} \nabla \cdot f dV$. Thus, equation (A.33) can be expressed as

$$\frac{\partial}{\partial t} \int_{CV} \rho dV + \int_{CV} \nabla \cdot \rho v dV = 0 \tag{A.34}$$

For control volume with fixed boundaries (i.e., no change in time) and applying Leibniz's rule we find that

$$\int_{CV} \frac{\partial}{\partial t} \rho dV + \int_{CV} \nabla \cdot \rho v dV = \int_{CV} \left(\frac{\partial \rho}{\partial t} - \nabla \cdot \rho v \right) dV = 0 \tag{A.35}$$

This relation applies to any control volume; this can only be true if the integrand

itself is zero, so that:

$$\frac{\partial \rho}{\partial t} + \nabla \cdot \rho v = 0 \quad (\text{A.36})$$

Expanding equation (A.36), we obtain

$$\frac{\partial \rho}{\partial t} + v \cdot \nabla \rho + \rho \nabla \cdot v = 0 \quad (\text{A.37})$$

where divergence of the velocity is $\nabla \cdot v = (\partial v_x / \partial x) + (\partial v_y / \partial y) + (\partial v_z / \partial z)$. Making use of the definition for the material derivative of the density, we obtain the continuity equation

$$\frac{D\rho}{Dt} + \rho \nabla \cdot v = 0 \quad (\text{A.38})$$

Note that for an incompressible fluid, ρ is a constant, $D\rho/Dt = 0$ and the continuity equation reduces to $\nabla \cdot v = 0$.

A.3 Navier-Stokes equations of fluid flow

The Navier-Stokes equations are the fundamental partial differential equations that describe the flow of fluids. These equations arise from applying Newton's second law to fluid motion. The principle of conservation of momentum states that mass times acceleration is equal to the sum of forces that act on a volume unit

$$\rho \frac{Dv}{Dt} = \sum F \quad (\text{A.39})$$

where density ρ is mass per unit volume (in a fixed control volume or infinitesimal fluid parcels), the material derivative of velocity is $Dv/Dt = dv/dt + v \cdot \nabla v$, and F is the total force per unit volume.

By examining the forces acting on a differential fluid element (Figure A.1), it may be shown that the force on each fluid particles is due to two components, fluid stresses and other external forces

$$\rho \frac{Dv}{Dt} = \nabla \sigma + P \quad (\text{A.40})$$

where σ is the stress tensor and P represents external forces. The x-component of equation (A.40), for example, in the absence of any external body forces, is given by

$$\rho \left(\frac{\partial v_x}{\partial t} + v_x \frac{\partial v_x}{\partial x} + v_y \frac{\partial v_x}{\partial y} + v_z \frac{\partial v_x}{\partial z} \right) = \frac{\partial \sigma_{xx}}{\partial x} + \frac{\partial \sigma_{xy}}{\partial y} + \frac{\partial \sigma_{xz}}{\partial z} \quad (\text{A.41})$$

For incompressible Newtonian fluid, the stress is proportional to the rate of deformation, and the stress tensor is assumed to take the form:

$$\sigma_{ij} = -p\delta_{ij} + \mu \left(\frac{\partial v_i}{\partial x_j} + \frac{\partial v_j}{\partial x_i} \right) \quad (\text{A.42})$$

where p is the pressure, δ_{ij} is the Kronecker delta and μ is viscosity of the fluid. The Navier-Stokes equations for a Newtonian fluid with no body force is obtained by substituting expression (A.42) for σ_{ij} into equation (A.40), and noting that for incompressible fluids $\nabla \cdot v = 0$,

$$\rho \frac{Dv}{Dt} = -\nabla p + \mu \nabla^2 v \quad (\text{A.43})$$

Flows of very small velocity are considered under Stokes flow condition when advective inertial forces are small compared with viscous forces. The laminar (smooth) flow occurs at very small Reynolds number (defined as the ratio of inertial forces to viscous forces of the fluid within a crack $Re = (\rho v w)/\mu < 1$ where w is the crack opening), especially for very small fluid velocities or very large viscosities when the viscous forces are dominant.

Dropping the time dependence and the advective terms from the Navier-Stokes equation (A.43) gives the the following equation for steady incompressible creeping flow

$$\nabla p = \mu \nabla^2 v \quad (\text{A.44})$$

A.3.1 Laminar unidirectional flow in a gap space

Consider the Stokes equation (A.44) describes the flow of the fracturing fluid inside the crack. If the fracture opening w is very much smaller than the fracture half-length ℓ , then the flow can be approximated unidirectional to the crack axis x , Figure A.2.

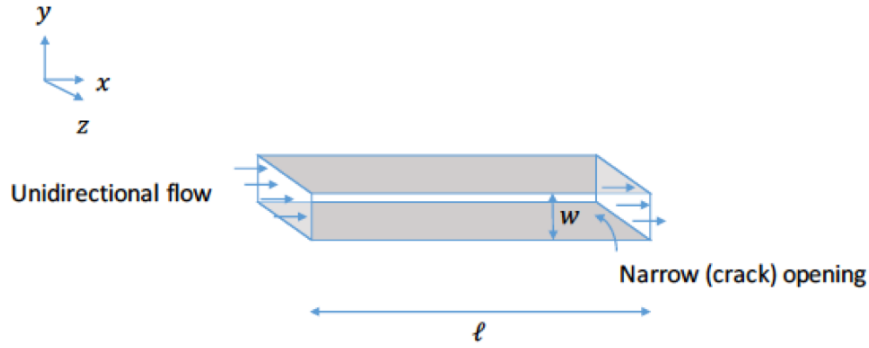


Figure A.2: Unidirectional flow between parallel plates

Generally, for an unidirectional flow of an incompressible fluid, if there is no velocity component in either the y or z direction (i.e., $v_y = 0$ and $v_z = 0$), the steady-state continuity equation becomes $\nabla v = \partial v_x / \partial x = 0$, and it can be concluded that the velocity v_x is only a function of y for an infinitely wide plain strain crack $v_x = v_x(y)$.

The x component of the Stokes equation reads

$$\frac{\partial p}{\partial x} = \mu \frac{\partial^2 v_x}{\partial y^2} \quad (\text{A.45})$$

and the y component reduces to

$$\partial p / \partial y = 0 \quad (\text{A.46})$$

that shows the fluid pressure is only a function of the x component and time. If we integrate equation (A.45) twice with respect to y and apply the no-slip boundary conditions at the crack walls ($v_x = 0$ at $y = \pm w/2$), it yields the parabolic distribution of the velocity profile for the two-dimensional Poiseuille flow

$$v_x = -\frac{1}{2\mu} \frac{\partial p}{\partial x} \left(\frac{w^2}{4} - y^2 \right). \quad (\text{A.47})$$

The net volume flux (per unit width in the z -direction) of fluid is obtained by integration of equation (A.47) to yield so called Poiseuille equation

$$q = -\frac{w^3}{12\mu} \frac{\partial p}{\partial x} \quad (\text{A.48})$$

where the average fluid velocity $\bar{v} = \frac{1}{w} \int_{-w/2}^{w/2} v_x dy$ relates to the flow rate by $q = \bar{v}w$.

Fluid mass conservation equation (A.34) for an element with dimensions dx , time dependent crack opening w , and dz of a plane crack propagating in an impermeable medium, and also accounting for the unidirectional flow, yields the continuity equation as

$$\frac{\partial}{\partial t}(\rho \cdot dx \cdot w \cdot dz) + \frac{\partial}{\partial x}(\rho \cdot \bar{v}_x \cdot dx \cdot w \cdot dz) = 0 \quad (\text{A.49})$$

which for incompressible fluids simplifies to

$$\frac{\partial w}{\partial t} + \frac{\partial \bar{v}_x w}{\partial x} = 0 \quad (\text{A.50})$$

where \bar{v}_x is the average velocity across the gap w .

APPENDIX B: SOME DETAILS OF THE ZERO-TOUGHNESS HYDRAULIC FRACTURE SOLUTION

Numerical solution of Adachi and Detournay [43] is in the form of expansions

$$\bar{\Omega} = \sum_{j=1}^m A_j \bar{\Omega}_j^* + B \bar{\Omega}^{**} \quad (|\xi| < 1), \quad \Pi = \sum_{j=1}^m A_j \Pi_j^* + B \Pi^{**} \quad (\xi \in \mathbb{R}) \quad (\text{A.1})$$

over a set of base

$$\bar{\Omega}_j^* = (1 - \xi^2)^{2/3} C_{2j-2}^{(1/6)}(\xi), \quad \Pi_j^* = -\frac{1}{4\pi} \int_{-1}^1 \frac{d\bar{\Omega}_j^*/d\eta}{\eta - \xi} d\eta \quad j = 1, 2, \dots, \quad (\text{A.2})$$

and particular

$$\bar{\Omega}^{**} = 4(1 - \xi^2) + 2\xi^2 \ln \left| \frac{1 - \sqrt{1 - \xi^2}}{1 + \sqrt{1 - \xi^2}} \right|, \quad \Pi^{**} = -\frac{1}{4\pi} \int_{-1}^1 \frac{d\bar{\Omega}^{**}/d\eta}{\eta - \xi} d\eta. \quad (\text{A.3})$$

functions. In the above, $C_i^{(\kappa)}(\xi)$ is the Gegenbauer polynomial of degree i and index κ [136]. Numerical values of coefficients A_j and B for the $m = 7$ terms solution are given in Table 1 of Adachi and Detournay [43] (for the case of a Newtonian fluid with $n = 1$).

Adachi and Detournay[43] evaluated the explicit form of the integrals for the pressure base and particular functions inside the crack, $|\xi| < 1$: see their equations (44)-(45) and (52) with their α set to $2/3$. Here, we complement their solution by evaluating explicit expressions for Π_j^* and Π^{**} outside of the crack, $|\xi| > 1$.

To evaluate Π_j^* we follow the approach outlined by Adachi and Detournay [43] (their Appendix A.2), in which the integrals (A.2)_b can be generally expressed in a complex-valued form in terms of the Legendre function of the second kind (their equation (A29) with $\alpha = 2/3$). The latter assume distinct real value forms for $|\xi| < 1$, as cited

by Adachi and Detournay [43], and for $|\xi| > 1$, as given by Abramowitz and Stegun [136, p. 332, sec. 8.1.3]. Using the latter, we can obtain explicit expressions for the pressure base functions for $|\xi| > 1$:

$$\Pi_1^* = -\frac{3}{20\sqrt{\pi}} \frac{\Gamma(\frac{8}{3})}{\Gamma(\frac{13}{6})} \frac{{}_1F_2\left(\frac{2}{3}, \frac{7}{6}, \frac{13}{6}; \frac{1}{\xi^2}\right)}{|\xi|^{4/3}(\xi^2 - 1)^{1/3}}$$

$$\Pi_{j>1}^* = \frac{\Gamma(2j - \frac{5}{3})}{3\Gamma(\frac{1}{6})\Gamma(2j - \frac{5}{6})} \times$$

$$\frac{(6j - 5)(\xi^2 - 1) {}_1F_2\left(j - \frac{1}{3}, j + \frac{1}{6}; 2j - \frac{5}{6}; \frac{1}{\xi^2}\right) - 4\xi^2 {}_1F_2\left(j - \frac{5}{6}, j - \frac{1}{3}; 2j - \frac{5}{6}; \frac{1}{\xi^2}\right)}{|2\xi|^{2j-2/3}(\xi^2 - 1)^{1/3}} \quad (\text{A.4})$$

where Γ is the Euler gamma function and ${}_2F_1$ is the Gauss hypergeometric function. The particular opening solution $\bar{\Omega}^{**}$, (A.3), corresponds to linear net pressure distribution along the crack $\Pi^{**} = 2 - \pi|\xi|$, $|\xi| < 1$. The corresponding stress perturbation outside the crack, $|\xi| > 1$, can be obtained from Tada et al. [137], page: 145] as $\Pi^{**} = 2 - 2|\xi| \operatorname{arccot} \sqrt{\xi^2 - 1}$.

The leading-order tip asymptotics of the opening and the stress change of the zero-toughness hydraulic fracture can be formulated by either rescaling the near tip solution (3.4)-(3.5), or by expanding the Adachi and Detournay's solution (A.1) (based on the corresponding base opening and pressure functions' expansions) near the tip, $|\xi| \rightarrow 1$. The result is recorded in (3.8), with one important extension for the stress (net pressure) asymptote. Namely, the latter has been enriched by including the next-order (constant) term $\Pi_{\text{const}} \approx 0.7508$ in the expansion, as obtained from the full solution (A.1)_b by subtracting the leading-order (singular) asymptote and then passing to the limit $|\xi| \rightarrow 1$. This enrichment allows to greatly improve the extent

of the near tip region where the stress asymptote is applicable.

APPENDIX C: NORMALIZED FORM OF SLIP FORMULATION ALONG THE HYDRAULICALLY FRACTURED FAULT)

The dimensionless form of the elasticity equation (2.13) for a symmetric crack is given by:

$$\frac{f(\delta(aX))}{f_p} \frac{[\sigma - p](aX)}{\sigma_0 - p_0} = \frac{\tau_0}{\tau_p} - \frac{1}{\pi} \frac{a_w}{a} \int_0^1 \frac{d\delta/\delta_w}{dX'} \frac{dX'}{X - X'}. \quad (\text{B.1})$$

The non-singular tip condition (2.14) yields:

$$\frac{2}{\pi} \int_{b/a}^1 \frac{f(\delta)}{f_p} \frac{\sigma - p}{\sigma_0 - p_0} \frac{dX}{\sqrt{1 - X^2}} = \frac{\tau_0}{\tau_p}. \quad (\text{B.2})$$

where we explicitly accounted for zero value of the shear stress along the frictionless part of the crack ($|X| < b/a$). The normalized effective normal stress distribution $(\sigma - p)/(\sigma_0 - p_0)$ is given by (3.11) in the main text.

APPENDIX D: STRESS FIELD AROUND PROPAGATING HYDRAULIC FRACTURE

Stress fields around the propagating semi-infinite hydraulic fracture (Figure 2.2) due to continuous distribution of opening Burger vector $\delta b_y = (dw/ds)\delta s$ along the hydraulic fracture line with no shear dislocation component ($b_x = 0$) are given by following using (A.29- A.30)

$$\begin{aligned}\sigma_{xx}(x, y) &= \frac{E'}{4\pi} \int_{-\infty}^{x_{tip}} \frac{dw}{d\xi} \frac{x_1(x_1^2 - y_1^2)}{r_1^4} d\xi \\ \sigma_{yy}(x, y) &= \frac{E'}{4\pi} \int_{-\infty}^{x_{tip}} \frac{dw}{d\xi} \frac{x_1(x_1^2 + 3y_1^2)}{r_1^4} d\xi \\ \sigma_{xy}(x, y) &= \frac{E'}{4\pi} \int_{-\infty}^{x_{tip}} \frac{dw}{d\xi} \frac{y_1(x_1^2 - y_1^2)}{r_1^4} d\xi\end{aligned}\tag{C.1}$$

Note that the stress fields are determined by superposition of background stresses (i.e., $\sigma_{min}, \sigma_{max}$) and induced stresses due to the opening dislocations.

C.1 Traction along the edge crack with an arbitrary orientation

The elastic medium for a short natural fracture at the edge of a propagating semi-infinite hydraulic fracture can be assumed as an elastic half-plane. The solution for the influence functions in an half-plane is obtained by using the solution for two bonded half-space and letting the rigidity of one of the half-space goes to zero. In this case, the solution for a dislocation at a distance (ξ, η) in cartesian coordinate (x, y) is given by [135]

$$G_{xxx} = y_1 \left(-\frac{1}{r_1^2} - \frac{2x_1^2}{r_1^4} + \frac{1}{r_2^2} + \frac{2x_2^2}{r_2^4} - \frac{4\xi x_2}{r_2^4} + \frac{4\xi^2}{r_2^4} + \frac{16\xi x_2^3}{r_2^6} - \frac{16\xi^2 x_2^2}{r_2^6} \right)\tag{C.2}$$

$$G_{xyy} = y_1 \left(-\frac{1}{r_1^2} + \frac{2x_1^2}{r_1^4} + \frac{1}{r_2^2} - \frac{2x_2^2}{r_2^4} + \frac{12\xi x_2}{r_2^4} - \frac{4\xi^2}{r_2^4} - \frac{16\xi x_2^3}{r_2^6} + \frac{16\xi^2 x_2^2}{r_2^6} \right)$$

$$G_{xxy} = -\frac{x_1}{r_1^2} + \frac{2x_1^3}{r_1^4} + \frac{x_2}{r_2^2} - \frac{2\xi}{r_2^2} - \frac{2x_2^3}{r_2^4} + \frac{16\xi x_2^2}{r_2^4} - \frac{12\xi^2 x_2}{r_2^4} - \frac{16\xi x_2^4}{r_2^6} + \frac{16\xi x_2^3}{r_2^6}$$

$$G_{yxx} = -\frac{x_1}{r_1^2} + \frac{2x_1^3}{r_1^4} + \frac{x_2}{r_2^2} - \frac{2\xi}{r_2^2} - \frac{2x_2^3}{r_2^4} - \frac{8\xi x_2^2}{r_2^4} + \frac{12\xi^2 x_2}{r_2^4} + \frac{16\xi x_2^4}{r_2^6} - \frac{16\xi^2 x_2^3}{r_2^6}$$

$$G_{yyy} = +\frac{3x_1}{r_1^2} - \frac{2x_1^3}{r_1^4} - \frac{3x_2}{r_2^2} - \frac{2\xi}{r_2^2} + \frac{2x_2^3}{r_2^4} + \frac{16\xi x_2^2}{r_2^4} - \frac{12\xi^2 x_2}{r_2^4} - \frac{16\xi x_2^4}{r_2^6} + \frac{16\xi^2 x_2^3}{r_2^6}$$

$$G_{yxy} = y_1 \left(-\frac{1}{r_1^2} + \frac{2x_1^2}{r_1^4} + \frac{1}{r_2^2} - \frac{2x_2^2}{r_2^4} - \frac{4\xi x_2}{r_2^4} + \frac{4\xi^2}{r_2^4} + \frac{16\xi x_2^3}{r_2^6} - \frac{16\xi^2 x_2^2}{r_2^6} \right)$$

using (A.31) and

$$x_2 = x + \xi, r_2^2 = x_2^2 + y_1^2 \quad (\text{C.3})$$

These influence functions are defined for a cartesian coordinate system in which the free surface is located along the y axis. In order to find influence functions for an elastic half-plane in which the free surface coincides with the global x axis coordinate (i.e., global coordinate axis for our problem), one should rotate the axis by $\theta = 270$ degrees. If we are counterclockwise rotating the two dimensional coordinate axes with basis vectors x and y into a new basis with basis vectors x' and y' , the new basis can be written in terms of the old basis by resolving the vectors $x' = x \cos \theta + y \sin \theta$ and $y' = -x \sin \theta + y \cos \theta$, which can be written using 2×2 transformation matrix with components a_{ij} as:

$$\begin{bmatrix} x' \\ y' \end{bmatrix} = \begin{bmatrix} \cos \theta & \sin \theta \\ -\sin \theta & \cos \theta \end{bmatrix} \begin{bmatrix} x \\ y \end{bmatrix} \quad (\text{C.4})$$

For a third rank tensor, the general transformation law is expressed as $T'_{ijk} = a_{il}a_{jm}a_{kn}T_{lmn}$ where a_{ijs} are components of the above rotational matrix.

Traction along an edge crack with an arbitrary orientation due to continuous distribution of shear Burger vector $\delta b_{\hat{x}} = (d\delta/d\hat{s})\delta\hat{s}$ are given by

$$\begin{aligned} \sigma_{\hat{y}\hat{y}}(\hat{x}, 0) &= \frac{E'}{4\pi} \int_{a_-}^{a_+} \frac{d\delta(\hat{s}, t)}{d\hat{x}} G_{\hat{x}\hat{y}\hat{y}}(\hat{x}, \hat{s}) d\hat{s} \\ \sigma_{\hat{x}\hat{y}}(\hat{x}, 0) &= \frac{E'}{4\pi} \int_{a_-}^{a_+} \frac{d\delta(\hat{s}, t)}{d\hat{x}} G_{\hat{x}\hat{x}\hat{y}}(\hat{x}, \hat{s}) d\hat{s} \end{aligned} \quad (\text{C.5})$$

where the local influence functions $G_{\hat{i}\hat{j}\hat{k}}(\hat{x}, 0; \hat{s})$ are found by multiplying the global influence functions C.2 by the third order rotational transformation matrix which has been provided in Appendix A7 Hills et al. [135].

APPENDIX E: NORMALIZED FORM OF SLIP FORMULATION FOR THE NATURAL FRACTURE BEFORE CROSSING

The normalized form of elasticity equation along the coordinate $\hat{\xi} = (\hat{x} - b)/a$ is given by

$$f_p \left(1 - \frac{\delta}{\delta_w}\right) \frac{\sigma_n(a\hat{\xi} + b) - (p_0 + \Delta p_{und}(a\hat{\xi} + b))}{\sigma_{min} - p_{tip}} = \frac{\tau^b(a\hat{\xi} + b)}{\sigma_{min} - p_{tip}} - \frac{1}{4\pi} \frac{a_w}{a} \int_{-1}^1 \frac{d\delta}{d\hat{s}} \frac{d\hat{s}}{\hat{\xi} - \hat{s}} \quad (\text{D.1})$$

where $a(t) = (a_+ - a_-)/2$ is the crack half-length and $b(t) = (a_+ + a_-)/2$ is the asymmetry measure.

Here, we implement the Gauss- Chebyshev quadrature approximation Erdogan and Gupta [138] to evaluate the integral appearing in the elasticity equation.

For a crack in an infinite medium, the method approximates the singular integral to a set of $N - 1$ algebraic equations by

$$\int_{-1}^1 \frac{F(\hat{s})}{\sqrt{1 - \hat{s}^2}} \approx \frac{\pi}{N} \sum_{j=1}^N F(\hat{s}_j) \quad (\text{D.2})$$

where $s_j \equiv \cos[\pi(2j - 1)/(2N)]$. When $F(\hat{s})$ has the form of kernel $1/(\hat{\xi} - \hat{s})$ the quadrature approximation holds at collocation points $\hat{\xi} = \hat{\xi}_i \equiv \cos[(\pi i)/N]$ where $i = 1, 2, \dots, N - 1$. We may define a new function

$$\frac{d\delta(\hat{s})}{d\hat{s}} = \frac{1}{\sqrt{1 - \hat{s}^2}} \phi(\hat{s}) \quad (\text{D.3})$$

which let us to approximate the integral in the above as

$$\int_{-1}^1 \frac{d\delta}{d\hat{s}} \frac{ds}{\hat{\xi} - s} \approx \frac{\pi}{N} \sum_{j=1}^N \frac{\phi(\hat{s}_j)}{\hat{\xi}_i - \hat{s}_j}. \quad (\text{D.4})$$

The Gauss-Chebyshev quadrature implies that $\phi(\hat{s})$ can be approximated with

$$\phi(\hat{s}) \approx \sum_{m=0}^p B_m T_m(\hat{s}) \quad (\text{D.5})$$

where $p < N$ and $T_m(\hat{s})$ is the m -th Chebyshev polynomial of the first kind. This can be expressed as (with summation for the repeated indices) $\phi_j = C_{jm} B_m$ where $\phi(\hat{s})$ is abbreviated as ϕ_j and $C_{jm} = T_m(\hat{s}_j)$. Thus the expression for slip at $\hat{\xi}_i$ reads

$$\delta_i \approx \int_{-1}^{\hat{\xi}_i} \frac{B_m T_m(\hat{s})}{\sqrt{1 - \hat{s}^2}} d\hat{s} \approx B_0 \left(\arcsin[\hat{\xi}_i] + \frac{\pi}{2} \right) + B_k \frac{\sin[k \arcsin[\hat{\xi}_i]]}{k} \approx D_{im} B_m \quad (\text{D.6})$$

Slip therefore can be written in terms of $\phi(\hat{s})$ using (D.5 and D.6)

$$\delta_i = S_{ij} \phi_j \quad (\text{D.7})$$

where $S_{ij} = D_{im} C_{jm}^{-1}$.

The index i provides a set of $N - 1$ equations for $N + 2$ unknowns: $a/a_w, b/a_w, \phi_j$.

The additional constraint of no dislocation beyond the crack will impose

$$\int_{-1}^1 \frac{\phi(\hat{s})}{\sqrt{1 - \hat{s}^2}} \approx \frac{\pi}{N} \sum_{j=1}^N \phi_j = 0. \quad (\text{D.8})$$

Furthermore, the values of the function ϕ_j at the end point are directly related to the stress intensity factor $\phi(\pm 1) = 0$ (non singular stress). These values are obtained from Krenk's interpolation formulae [139]:

$$\phi(-1) = 0 = \frac{1}{N} \sum_{i=1}^N \frac{\sin[\pi(2N-1)(2j-1)/4n]}{\sin[\pi(2j-1)/4n]} \phi_{n-j+1} \quad (\text{D.9})$$

$$\phi(1) = 0 = \frac{1}{N} \sum_{i=1}^N \frac{\sin[\pi(2N-1)(2j-1)/4n]}{\sin[\pi(2j-1)/4n]} \phi_j \quad (\text{D.10})$$

APPENDIX F: NORMALIZED FORM OF SLIP FORMULATION FOR THE EDGE CRACK

With the change of variable $\hat{\xi} = 2\hat{x}/a - 1$ we may simplify the elasticity integral (5.1)

$$f_p \left(1 - \frac{\delta}{\delta_w}\right) \frac{\sigma_n - p}{\sigma_{min} - p_{tip}} = \frac{\tau^b}{\sigma_{min} - p_{tip}} - \frac{1}{4\pi} \frac{a_w}{a} \int_{-1}^1 \frac{d\delta}{d\hat{s}} G_{\hat{\xi}\hat{\xi}\hat{\xi}} d\hat{s} \quad (\text{E.1})$$

where the normal stress distribution along the fracture plane is given by:

$$\frac{\sigma_n}{\sigma_{min} - p_{tip}} = \frac{\sigma_n^b \left(a(\hat{\xi} + 1)/2\right)}{\sigma_{min} - p_{tip}} - \frac{1}{4\pi} \frac{a_w}{a} \int_{-1}^1 \frac{d\delta}{d\hat{s}} G_{\hat{\xi}\hat{\xi}\hat{\xi}} d\hat{s} \quad (\text{E.2})$$

The Gauss- Chebyshev quadrature approximation [138] for the surface crack has the form of

$$\int_{-1}^1 \frac{\sqrt{1+\hat{s}}}{\sqrt{1-\hat{s}}} F(\hat{s}) \approx \frac{2(1+\hat{s}_j)}{2N+1} \sum_{j=1}^N F(\hat{s}_j) \quad (\text{E.3})$$

where $\hat{s}_j \equiv \cos[\pi(2j-1)/(2N+1)]$. The quadrature approximation holds at collocation points $\hat{\xi} = \hat{\xi}_i \equiv \cos[\pi(2i)/(2N+1)]$ where $i = 1, 2, \dots, N$.

This type of Gauss-Chebyshev with the fundamental function $\sqrt{1+\hat{\xi}'}/\sqrt{1-\hat{\xi}'}$ pertains to a singular displacement density at $\hat{s} = +1$ and bounded at $\hat{s} = -1$. Zero displacement discontinuity at the mouth $d\delta(\hat{s})/d\hat{s}(-1) = 0$ implies that the crack faces at the mouth are parallel which is not physically reasonable. In order to overcome over prescription of deformation of the medium in the neighborhood of the mouth of the crack, a modification to the dislocation density behavior can be made [135]

$$\frac{d\delta(\hat{s})}{d\hat{s}} = \frac{\sqrt{1+\hat{s}}}{\sqrt{1-\hat{s}}} \phi(\hat{s}) + A \frac{1-\hat{s}}{2} \quad (\text{E.4})$$

where A is an unknown constant and a linear bounded function of $f(\hat{s}) = (1 - \hat{s})/2$ ensures the dislocation density at the crack mouth is bounded.

An approximate expression for slip at $\hat{\xi}_i$ can be written using (E.4 and D.5) as

$$\delta_i = \int_{-1}^{\hat{\xi}_i} \left(\frac{\sqrt{1 + \hat{s}}}{\sqrt{1 - \hat{s}}} B_m T_m(\hat{s}) + A \frac{1 - \hat{s}}{2} \right) d\hat{s} \quad (\text{E.5})$$

where it can be written in the following form

$$\delta_i = D_{im} B_m + A \int_{-1}^{\hat{\xi}_i} \frac{1 - \hat{s}}{2} d\hat{s} = S_{ij} \phi_j + A \int_{-1}^{\hat{\xi}_i} \frac{1 - \hat{s}}{2} d\hat{s} - \delta_0 \quad (\text{E.6})$$

where $S_{ij} = D_{im} C_{jm}^{-1}$. Slip at the crack mouth δ_0 ($\hat{\xi} = 0$) can be calculated by

$$\delta_0 = \delta_{\hat{\xi}=1} - \int_{-1}^1 \left(\frac{d\delta}{d\hat{s}} \right) d\hat{s} = \int_{-1}^1 \left(\frac{\sqrt{1 + \hat{s}}}{\sqrt{1 - \hat{s}}} \phi_j + A \frac{1 - \hat{s}}{2} \right) d\hat{s} = -\frac{2(1 + \hat{s}_j)}{2N + 1} \sum_{j=1}^N \phi(\hat{s}_j) - A \quad (\text{E.7})$$

The index i provides a set of N equations for $N + 2$ unknowns: $a/a_w, \phi_j, A$. The additional constraints of bounded stress intensity factor $\phi(\pm 1) = 0$ are imposed applying Krenk's interpolation approximation for the end-points [139]:

$$\phi(-1) = 0 = \sum_{i=1}^N \frac{\sin[i\pi(2N - 1)/(2j + 1)]}{\sin[i\pi/(2j - 1)]} \phi_{n-j+1} \quad (\text{E.8})$$

$$\phi(1) = 0 = \frac{2}{2N + 1} \sum_{i=1}^N \cot\left[\frac{2i - 1}{2N + 1} \frac{\pi}{2}\right] \sin\left[\frac{2i - 1}{2N + 1} N\pi\right] \phi_j \quad (\text{E.9})$$